5-2019

Predicting the Mechanical Properties of Nanocomposites Reinforced with 1-D, 2-D and 3-D Nanomaterials

Scott Edward Muller
University of Arkansas, Fayetteville

Predicting the Mechanical Properties of Nanocomposites
Reinforced with 1-D, 2-D and 3-D Nanomaterials

A dissertation submitted in partial fulfillment
of the requirements for the degree of
Doctor of Philosophy in Engineering

by

Scott E. Muller
Brigham Young University-Idaho
Bachelor of Science in Physics, 2013

May 2019
University of Arkansas

This dissertation is approved for recommendation to the Graduate Council.

Arun Nair, Ph.D.
Dissertation Director

Salvador Barraza-Lopez, Ph.D.
Committee Member

Jim Leylek, Ph.D.
Committee Member

Paul Millett, Ph.D.
Committee Member

Uche Wejinya, Ph.D.
Committee Member

Abstract

Materials with features at the nanoscale can provide unique mechanical properties and increased functionality when included as part of a nanocomposite. This dissertation utilizes computational methods at multiple scales, including molecular dynamics (MD) and density functional theory (DFT), and the coupled atomistic and discrete dislocation multiscale method (CADD), to predict the mechanical properties of nanocomposites possessing nanomaterials that are either 1-D (carbyne chains), 2-D (graphene sheets), or 3-D (Al/amorphous-Si core-shell nanorod).

The MD method is used to model Ni-graphene nanocomposites. The strength of a Ni-graphene nanocomposite is found to improve by increasing the gap between the graphene sheet and a crack embedded in the Ni matrix. Ni-graphene nanocomposites also show substantially greater strength than pure Ni, depending on the loading direction and crack orientation relative to the graphene sheet. Moreover, polycrystalline graphene may serve as a better reinforce in Ni-graphene nanocomposites due to its improved interfacial shear stress with the Ni matrix compared to pristine graphene. This work develops a patchwork quilt method for generating polycrystalline graphene sheets for use in MD models.

Carbyne-based nanocomposites are modeled from first principles using DFT. This research finds that carbyne can only serve as an effective reinforcement in Ni-based nanocomposites when it is dielectrically screened from the Ni matrix, otherwise the carbyne structure is lost. When graphene is used as a dielectric screen, the local stiffness of the nanocomposite improves with the number of carbyne chains present. Specific stiffness is introduced as an alternative to elastic stiffness for characterizing low-dimensional materials because it is not dependent on volume when derived using an energy vs. strain relation.

A two-material formulation of CADD is developed to model Al/a-Si core-shell nanorods under indentation/retraction. The structural deformation behavior is found to be dependent on the geometry of both core and shell. When present, the a-Si shell protects the Al core by delocalizing forces produced by the indenter. It is also found that substrate deformation becomes important for core-shell structures with sufficiently small cores.

This work can help guide experimental and computational work related to the discussed 1-D, 2-D and 3-D nanomaterials and aid in future nanocomposite design.

Acknowledgements

There are many people who provided support to make this dissertation possible. I would like to thank my advisor Dr. Arun K. Nair who provided invaluable vision and guidance throughout my graduate research and education. He patiently allowed me to grow and figure things out for myself, while also providing key insights at times where the work would otherwise have stagnated. I also want to acknowledge the support of my fellow graduate students in the Multiscale Materials Modeling Laboratory: Raghuram Santhapuram, Matthew Brownell, Mohan Yasodharababu, Marco Fielder and Yucong Gu. Each of them took time to assist me with their unique perspectives and skills as I wrote papers, prepared presentations, and beat my head against tricky problems. I want to specifically thank Raghuram for his help on the paper he coauthored with me. Special thanks to Dr. Salvador Barraza-Lopez, Dr. Jim Leylek, Dr. Paul Millett and Dr. Uche Wejinya for taking time out of their busy schedules to serve on my dissertation committee. I am very thankful for the professors and staff at the University of Arkansas, particularly the Mechanical Engineering Department, who provided me with an advanced education. I would like to further thank the graduate school for the Doctoral Academy Fellowship which allowed me to continue supporting my family while I pursued my degree.

The computational work present throughout my dissertation would not have been possible without use of the Arkansas High Performance Computing Center. Financial support for my work was provided by the Arkansas EPSCoR Program, the Center for Advanced Surface Engineering, the Arkansas Science and Technology Authority, the Arkansas Economic Development Commission, and the National Science Foundation (specific grant numbers can be found in the Acknowledgements sections of chapters 4-7).

On a personal note, I'm grateful for my parents who raised me with a love of learning and provided an example of a healthy work-life balance that I have tried to emulate in my own life. I also want to thank my wife Elisa and our daughter Lucy for supporting and being patient with me throughout this process, and for making me happy to come home each day. Finally, I want to acknowledge the unseen work that Elisa does every day for our growing family, which is just as important to our future happiness as any of the work I have done.

Table of Contents

List of Published Papers

Chapter 4

Muller, Scott E., and Arun K. Nair, Dislocation Nucleation in Nickel-Graphene Nanocomposites Under Mode I Loading, *JOM: The Journal of the Minerals, Metals & Materials Society (TMS)* 68(7) (2016) 1909-1914.

Chapter 5

Muller, Scott E., Raghuram R. Santhapuram, and Arun K. Nair, Failure mechanisms in pre-cracked Ni-graphene nanocomposites, *Computational Materials Science* 152 (2018) 341-350.

Chapter 6

Muller, Scott E., and Arun K. Nair, Carbyne as a fiber in metal-matrix nanocomposites: A first principle study, *Computational Materials Science* 159 (2019) 187-193.

Chapter 7

Muller, Scott E., and Arun K. Nair, Deformation mechanisms of Al/amorphous-Si core-shell nanorods, *Modelling and Simulation in Materials Science and Engineering* (Accepted).

Certification of First Author by Co-author

Arun K. Nair

I hereby certify that Scott E. Muller is first author of the articles included in chapters 4, 5, 6 and 7 and has completed at least 51% of the work described in these articles.

Signature Date

_____ _____

Certification of First Author by Co-author

Raghuram R. Santhapuram

I hereby certify that Scott E. Muller is first author of the article included in chapter 5 and has completed at least 51% of the work described in this article.

Signature Date

_____ _____

Chapter 1

Introduction

1.1 Motivation

Composite materials are a combination of two or more distinct materials, with the aim of blending the properties of the materials. Composites can be optimized to meet the needs of applications by careful choice of matrix/filler material and by controlling filler dispersion and alignment. For example, strong and flexible fibers will make for a stronger and more flexible composite so long as the matrix and fiber have high interfacial shear strength. For mechanical properties, filler materials with high aspect ratios are generally preferred because they tend to be stronger, more flexible, and have fewer defects than bulk materials. This is one of the reasons that nanomaterials (materials with at least one dimension at the nanoscale) are sought after for use in composite materials.

Nanocomposites are a special class of composite material where at least one of the constituent materials is a nanomaterial. The included nanomaterial can markedly improve the electrical, thermal, and mechanical properties of the host material [1-3]. Emerging applications for nanocomposites are wide ranging, including medical [4], industrial [5] and commercial [6]. There are generally three kinds of nanomaterials defined by their number of dimensions at the nanoscale: nanolayers, nanofibers, and nanoparticles [7]. The most extreme versions of nanolayers and nanofibers in terms of length scale are 2-D and 1-D materials respectively.

Before 2004 2-D materials were only theoretically possible. With the discovery of graphene by Novoselov et al. [8] the era of 2-D materials began. Now 2-D materials are an important part of cutting edge research in materials science. Graphene is a 2-D material in the

sense that it is a sheet of carbon atoms one atom thick, as shown in Figure 1.1(a). Graphene has exceptional electrical, thermal and mechanical properties, including an astonishing tensile strength of 130 GPa and a Young's modulus of 1 TPa [9]. Graphene is currently being embedded in both polymer [10, 11] and metal-matrix nanocomposites [9, 12-14]. The effects that graphene has on the yield properties of matrixes in which it is embedded is still being explored.

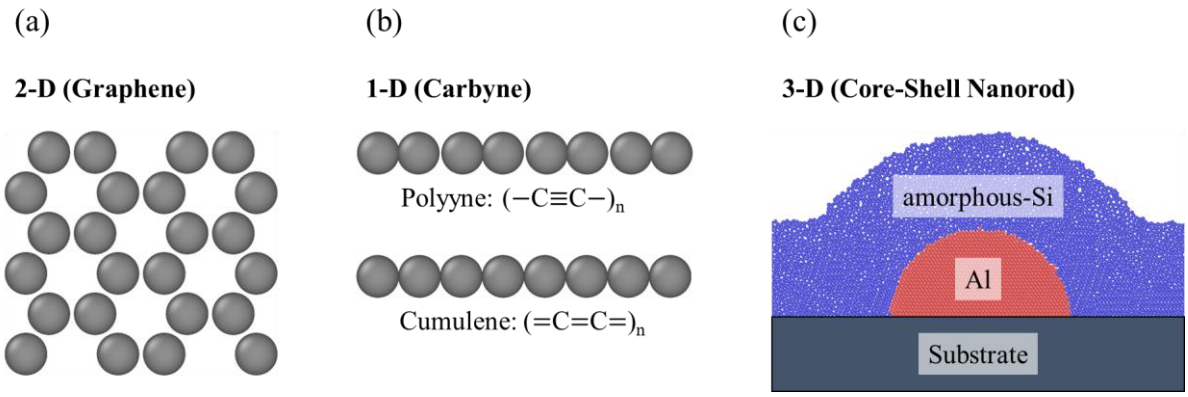

Figure 1.1. Visualization of nanomaterials of different dimensionality: (a) a 2-D graphene sheet, (b) the two types of 1-D carbyne chains, (c) Al/amorphous-Si core-shell nanorod. Note that for (b) there are two kinds of carbyne shown: polyyne which has alternating single and triple bonds, and cumulene which has repeating double bonds; these chains are discussed in more detail in section 2.3.

Linear carbon chains are a class of 1-D materials that are currently being investigated, with many attempts at synthesis. These chains are 1-D in the sense that they have a diameter of one atom, which results in incredibly high aspect ratios. Carbyne is the strongest of these types of chains and could be considered the "strongest material in the world", with a lower order estimate of its tensile strength being around 270 GPa [15] and predictions for its Young's modulus ranging from 1.3 TPa [16, 17] to 32.7 TPa [18] (in its polyyne form). The two types of carbyne chains, polyyne and cumulene, are visualized in Figure 1.1(b). Over the past decade many advances have been made toward synthesizing longer carbyne chains [19-21], which would greatly improve their ability to be tested experimentally. Shi et al. recently developed a technique for growing carbyne chains composed of more than 6400 atoms—two orders of magnitude longer than the previous

longest recorded carbyne chain length [21]. Though development of long carbyne chains is still in its early stages, the possible benefits of this material are a strong motivation for continued work. As carbyne begins to enter real-world use it will be important to know what advantages and disadvantages it will provide as part of a nanocomposite system.

Nanocomposites with reinforcing materials with 1-D and 2-D features are an important area of modern nanocomposite research. Their high aspect ratios coupled with their high strength and flexibility give them great potential for use as filler material [9]. However, most nanocomposites have reinforcing materials with thickness/diameter greater than one atom; in this sense they are 3-D. Reinforcement at this scale is useful for many applications, including nanotribology in the form of nanotextured surfaces [22, 23]. These surfaces can greatly improve tribological properties but are highly prone to plastic deformation [24, 25]. Nanocomposites comprising core-shell nanostructures can be used to make nanotextured surfaces more deformation resistant [26]. Work by Fleming et al. investigated Al/a-Si core-shell nanostructures and nanorods, visualized in Figure 3(c), and found that these nanocomposites experienced substantial recovery after initial indentation [27, 28]. While they tested different core-shell geometries, the relationship between core-shell structures and their deformation characteristics can be more thoroughly explored.

1.2 Objectives

The objective of this dissertation is to predict the mechanical properties of nanocomposites where the reinforcing nanomaterial is either 1-D, 2-D or 3-D. Diverse computational methods spanning different length scales are used to simulate these nanocomposites to obtain quantitative and qualitative descriptions of their behavior. The 1-D and 2-D nanocomposites use Ni as the matrix material and either carbyne or graphene as the reinforcing nanomaterial respectively. Both

these nanocomposites have the reinforcing material sandwiched within the Ni matrix. The nanocomposite possessing 3-D nanomaterial is an Al/a-Si core-shell nanorod, where both Al and a-Si have some features at the nanoscale. The specific objectives in studying these nanocomposites are:

1. Predict the yield behavior of Ni-graphene nanocomposite when a crack is present while varying loading direction and crack orientation. (Chapters 4 and 5)
2. Develop a method to make polycrystalline graphene samples computationally (section 3.1.4), and investigate changes in yield behavior within Ni-graphene when polycrystalline graphene is used rather than pristine. (Chapter 5)
3. Develop a Ni-carbyne model and predict the maximum contribution to stiffness that carbyne can make within the Ni matrix. (Chapter 6)
4. Determine the stability of carbyne in a Ni matrix, and the effect on stability when graphene is used as a dielectric screen. (Chapter 6)
5. Develop a two-material formulation of the coupled atomistic and discrete dislocation (CADD) method for use in modeling an Al/a-Si core-shell nanorod. (Chapter 7)
6. Predict the deformation mechanisms of Al/a-Si core-shell nanorods under indentation and retraction as a function of core-shell structure. (Chapter 7)

1.3 Layout of dissertation

This dissertation is separated into eight chapters and two appendices. Chapter 2 is a literature review to provide a background for the nanomaterials being modeled in this work as well as the current state of closely connected nanocomposites. Chapter 3 describes the computational methods used in this research. Chapters 4 and 5 are published papers [29, 30] predicting the properties and yield behavior of Ni-graphene nanocomposites, as mentioned in objectives 1 and 2.

Chapter 6 is a paper that has been submitted for review predicting the contribution of carbyne in a Ni-based nanocomposite from first principles, addressing objectives 3 and 4. Chapter 7 is a paper that has been submitted for review investigating the deformation mechanisms of an Al/a-Si core-shell nanorod using a two-material formulation of the CADD method, addressing objectives 5 and 6. Chapter 8 is the conclusion where key results of the dissertation are summarized, the main takeaways are set forth, and some potential future work is discussed. Appendix A contains stress vs. strain information related to the results in chapter 5. Appendix B provides a derivation for the general rule of mixtures for specific stiffness used in chapter 6.

References

[1] H. Aguilar-Bolados, M.A. Lopez-Manchado, J. Brasero, F. Avilés, M. Yazdani-Pedram, Effect of the morphology of thermally reduced graphite oxide on the mechanical and electrical properties of natural rubber nanocomposites, Composites Part B: Engineering 87 (2016) 350-356.

[2] P. Pokharel, S.H. Lee, D.S. Lee, Thermal, mechanical, and electrical properties of graphene nanoplatelet/graphene oxide/polyurethane hybrid nanocomposite, Journal of nanoscience and nanotechnology 15(1) (2015) 211-214.

[3] S. Shang, L. Gan, M.C.-w. Yuen, S.-x. Jiang, N.M. Luo, Carbon nanotubes based high temperature vulcanized silicone rubber nanocomposite with excellent elasticity and electrical properties, Composites Part A: Applied Science and Manufacturing 66 (2014) 135-141.

[4] L.E. Strong, S.N. Dahotre, J.L. West, Hydrogel-nanoparticle composites for optically modulated cancer therapeutic delivery, Journal of Controlled Release 178 (2014) 63-68.

[5] S. Veprek, M.J. Veprek-Heijman, Industrial applications of superhard nanocomposite coatings, Surface and Coatings Technology 202(21) (2008) 5063-5073.

[6] D.A.P. de Abreu, J.M. Cruz, I. Angulo, P.P. Losada, Mass transport studies of different additives in polyamide and exfoliated nanocomposite polyamide films for food industry, Packaging Technology and Science: An International Journal 23(2) (2010) 59-68.

[7] H. Hu, L. Onyebueke, A. Abatan, Characterizing and modeling mechanical properties of nanocomposites-review and evaluation, Journal of minerals and materials characterization and engineering 9(04) (2010) 275.

[8] K.S. Novoselov, A.K. Geim, S.V. Morozov, D. Jiang, Y. Zhang, S.V. Dubonos, I.V. Grigorieva, A.A. Firsov, Electric field effect in atomically thin carbon films, Science 306(5696) (2004) 666-9.

[9] I.A. Ovid'ko, Metal-Graphene Nanocomposites with Enhanced Mechanical Properties: A Review, Rev Adv Mater Sci 38(2) (2014) 190-200.

[10] G. Mittal, V. Dhand, K.Y. Rhee, S.-J. Park, W.R. Lee, A review on carbon nanotubes and graphene as fillers in reinforced polymer nanocomposites, Journal of Industrial and Engineering Chemistry 21 (2015) 11-25.

[11] K. Hu, D.D. Kulkarni, I. Choi, V.V. Tsukruk, Graphene-polymer nanocomposites for structural and functional applications, Progress in Polymer Science 39(11) (2014) 1934-1972.

[12] P.K. HG, M.A. Xavior, Graphene reinforced metal matrix composite (GRMMC): a review, (2014).

[13] Z. Hu, G. Tong, D. Lin, C. Chen, H. Guo, J. Xu, L. Zhou, Graphene-reinforced metal matrix nanocomposites–a review, Materials Science and Technology 32(9) (2016) 930-953.

[14] A.D. Moghadam, E. Omrani, P.L. Menezes, P.K. Rohatgi, Mechanical and tribological properties of self-lubricating metal matrix nanocomposites reinforced by carbon nanotubes (CNTs) and graphene–a review, Composites Part B: Engineering 77 (2015) 402-420.

[15] A. Timoshevskii, S. Kotrechko, Y. Matviychuk, Atomic structure and mechanical properties of carbyne, Phys Rev B 91(24) (2015).

[16] Y. Zhang, Y. Su, L. Wang, E.S.-W. Kong, X. Chen, Y. Zhang, A one-dimensional extremely covalent material: monatomic carbon linear chain, Nanoscale research letters 6(1) (2011) 577.

[17] X. Liu, G. Zhang, Y.-W. Zhang, Tunable mechanical and thermal properties of one-dimensional carbyne chain: Phase transition and microscopic dynamics, The Journal of Physical Chemistry C 119(42) (2015) 24156-24164.

[18] M. Liu, V.I. Artyukhov, H. Lee, F. Xu, B.I. Yakobson, Carbyne from first principles: chain of C atoms, a nanorod or a nanorope, ACS Nano 7(11) (2013) 10075-82.

[19] W.A. Chalifoux, R.R. Tykwinski, Synthesis of polyynes to model the sp-carbon allotrope carbyne, Nat Chem 2(11) (2010) 967-71.

[20] R.R. Tykwinski, W. Chalifoux, S. Eisler, A. Lucotti, M. Tommasini, D. Fazzi, M. Del Zoppo, G. Zerbi, Toward carbyne: Synthesis and stability of really long polyynes, Pure Appl Chem 82(4) (2010) 891-904.

[21] L. Shi, P. Rohringer, K. Suenaga, Y. Niimi, J. Kotakoski, J.C. Meyer, H. Peterlik, M. Wanko, S. Cahangirov, A. Rubio, Confined linear carbon chains as a route to bulk carbyne, Nature materials 15(6) (2016) 634-639.

[22] T. Sukhanova, Characterization of multiblock (segmented) copoly (urethane-imide) s and their nanocomposites using AFM, nanotribology and nanoindentation methods, (2018).

[23] A.S. Mohammed, A. bin Ali, M. Nesar, Evaluation of tribological properties of organoclay reinforced UHMWPE nanocomposites, Journal of Tribology 139(1) (2017) 012001.

[24] Z. Guo, Y. Meng, C. Su, H. Wu, An on-chip micro-friction tester for tribology research of silicon based MEMS devices, Microsystem Technologies 14(1) (2008) 109-118.

[25] L. Chen, J. Zhang, Design and properties of self-assembled ordered films for nanolubrication, Surfactants in tribology 4 (2015) 97-150.

[26] W. Tidwell, D. Scott, H. Wang, R. Fleming, M. Zou, Nanoindentation study of deformation-resistant Al/a-Si core–shell nanostructures, Acta Materialia 59(15) (2011) 6110-6116.

[27] R.A. Fleming, J.A. Goss, M. Zou, Material dimensionality effects on the nanoindentation behavior of Al/a-Si core-shell nanostructures, Applied Surface Science 412 (2017) 96-104.

[28] R.A. Fleming, M. Zou, The effects of confined core volume on the mechanical behavior of Al/a-Si core-shell nanostructures, Acta Materialia 128 (2017) 149-159.

[29] S.E. Muller, A.K. Nair, Dislocation Nucleation in Nickel-Graphene Nanocomposites Under Mode I Loading, Jom 68(7) (2016) 1909-1914.

[30] S.E. Muller, R.R. Santhapuram, A.K. Nair, Failure mechanisms in pre-cracked Ni-graphene nanocomposites, Computational Materials Science 152 (2018) 341-350.

Chapter 2

Literature Review

Each of the papers in chapters 4-7 include an introduction where much of the relevant connected literature is discussed. This chapter provides a basic overview of recent literature related to the reinforcing materials used in this work, while trying to avoid redundancy with later chapters. Graphene is discussed first, followed by graphene in the context of metal-matrix nanocomposites. Then some of the basic aspects of carbyne and work related to its applications are reviewed. Finally, Al/amorphous-Si (Al/a-Si) core-shell nanorods and their connection to nanotextured surfaces is discussed.

2.1 Graphene

Graphene is a carbon sheet with a honeycomb lattice structure [1]. It is the first of a host of different 2-D materials developed over the past two decades [2]. It's superior mechanical, electrical and thermal properties have given it prominence in materials science research [3]. Techniques for producing graphene vary greatly in terms of cost and graphene quality [4]. Micromechanical cleavage is a mechanical exfoliation technique whereby high quality monolayer graphene sheets can be achieved, but its cost is quite high in terms of time and labor [5]. Liquid-phase exfoliation techniques for producing graphene are gaining some traction due to their low cost and scalability, but the quality of graphene produced is also of lower quality [6]. Chemical vapor deposition (CVD) is currently the most popular technique for producing high quality graphene, with potential for scalability [7, 8]. Common substrates for CVD grown graphene include both nickel (Ni) and copper (Cu) [9, 10], from which completed graphene sheets can be

transferred to other desired substrates [11]. Substrates with defects, such as polycrystalline-Ni, can result in substantial graphene defects, such as multilayer graphene and wrinkling [12, 13].

When synthesizing macroscopic graphene samples, there will always be some structural defects such as vacancies and grain misorientation [14], which can vary from 0° to 30° [15]. These defects can have a significant impact on the mechanical properties of graphene [16]. Zhang et al. performed a computational study comparing the intrinsic tensile strength of pristine graphene to graphene with misoriented grain boundaries [17]. The degree of misorientation was varied during the study. It was found that grain boundaries with high thermodynamic stability proved nearly as strong as pristine graphene, however those with high inflection angles due to their misorientation would buckle along the grain boundary. This buckling led to a reduced intrinsic tensile strength. The same results were found by Lee et al. who performed experimental tests on CVD-grown graphene sheets, with multiple grains present on the sheet [18]. They found that the strength of polycrystalline graphene would only be slightly reduced from pristine graphene if postprocessing were performed to avoid damage or rippling. More recently Zandiatashbar et al. performed experimental and computational work on graphene with defects introduced by plasma etching [19]. Surprisingly they found that even highly defective graphene samples showed only slightly diminished elastic stiffness compared to pristine graphene. Meaning that graphene can tolerate the presence of defects without significant loss to its mechanical properties. Lopez-Polin et al. took this idea even further in their experimental work in which they found that the in-plane elastic modulus of graphene can actually be improved with increasing vacancy density, up to a certain point [20]. And for a range of grain sizes, polycrystalline graphene has been shown to be tougher than pristine graphene [21].

2.2 Graphene in metal-matrix nanocomposites

In the material science community graphene has been experiencing a kind of "gold rush" in the level of attention it has attracted for possible application [3]. While other 2-D materials are receiving attention in research [2, 22], graphene is still the most popular candidate for use in nanocomposites. The number of publications dealing with graphene has skyrocketed, and so has the number of articles dealing with graphene composites [23]. Polymer-graphene nanocomposites are being researched for use in many areas including material design for cars and aircraft, where graphene nanocomposites offer the benefit of a light material that can save on fuel costs without sacrificing strength [24]. This is true also for metal-graphene nanocomposites, which can better take advantage of graphene's high electrical and thermal conductivity than polymer-graphene nanocomposites [3].

One major challenge for producing bulk metal-graphene nanocomposites is developing scalable methods for the dispersion of graphene within the metal-matrix. Some approaches are done in the context of powder metallurgy, where graphene platelets are included with metal flakes, which are then combined to form the final composite structure [25-27]. The most common method currently used in research for metal-graphene nanocomposites is layer-by-layer assembly, often making use of CVD [28]. While the scalability of this method is currently limited, it allows for excellent nanolayer control and maintains high quality graphene [29]. This approach also enables the nanocomposite to best take advantage of graphene's unique mechanical, electrical and thermal properties [30, 31]. Some methods make use of graphene oxide which anchors better to metals, is easier to disperse in water, and provides more avenues for fabrication [29, 32]. Graphene oxide nanocomposites are not discussed in this research, but it is a promising area of research because of the added interactions and applications possible with this form of graphene [33, 34].

Kim et al. studied the strengthening effect of single-layer graphene in metal-matrix composites both experimentally and computationally [35]. They used layer-by-layer CVD to grow single-layer graphene, which was then deposited on thin copper or nickel films, followed by the stacking of another metal layer. This pattern was repeated until the desired composite layup was complete. The result was a stable metal-graphene nanocomposite with much of the graphene in single layer form, with the graphene having a weight fraction of around 0.00004%. Nanopillars were cut out of the fabricated nanocomposite, each having a diameter of 200 nm and heights between 400 and 600 nm. Nanopillar compression tests were then performed where the nanopillars were pressed into a flat surface at a rate of 0.8-1.2 nm/s, which is a strain rate of 0.002 s^{-1}. Researchers observed that there was a distinct lack of plastic deformation in the bottom half of the nanopillar, below the graphene layer. Computational work by Kim et al. showed that graphene effectively inhibits dislocation passage from one region of metal to the next, with dislocations collecting at the graphene layer [35].

Chang et al. investigated the mechanical behavior of metal-graphene under compressive loading for both single-layer and multi-layer graphene [36]. They computationally modeled Ni-graphene under nanoindentation while varying the number of graphene layers and determined the effect this had on plastic deformation. They also assessed whether this could allow for the tuning of metal-graphene to favor specific mechanical properties. In their simulation, nickel blocks were generated with different numbers of embedded layers of graphene. Nanoindentation was performed normal to the embedded graphene sheet(s). They found that increasing the number of graphene layers causes dislocation nucleation to occur at greater indentation depth, while also producing a decrease in the stiffness/hardness of the nanocomposite. This suggests that elastic strain and hardness can be tuned based on the number of layers of graphene present under

nanoindentation. Dislocations generated during the simulation were unable to penetrate the graphene barrier, in agreement with Kim et al. [35].

Finding new layups for graphene-based nanocomposites and their associated mechanical properties is an area of research that is rapidly expanding [37, 38]. Investigating the way that yield behavior is affected by these different layups is just as important. Ovid'ko et al. found that the competition between plastic deformation and fracture in metal-graphene nanocomposites depends on parameters such as metallic layer and graphene layer thickness [39]. Yield may depend on many other things including potential defects in matrix materials, and the way nanocomposites are to be loaded relative to embedded graphene sheets.

Because polycrystalline graphene is more common than pristine graphene in real world fabrication, nanocomposite models that include polycrystalline graphene will better predict many of the mechanical properties of real graphene-based nanocomposites. Chu et al. showed that defects in graphene can improve its interfacial adhesion with a Cu matrix [40]. This implies that polycrystalline graphene may also have greater interfacial adhesion than pristine graphene in reinforcing metal-matrix nanocomposites. However, prior to the published work presented here, no computational studies had been conducted to compare the mechanical properties of nanocomposites with pristine graphene and nanocomposites with polycrystalline graphene. One possible reason for this omission in computational studies is that ReaxFF [41] is the most common potential used in MD simulations of polycrystalline graphene, and this potential is not equipped to model many possible matrix materials. Yet other potentials, such as the adaptive intermolecular reactive empirical bond order (AIREBO) potential, have been used to model polycrystalline graphene [42-45]. AIREBO has also been used in conjunction other potentials to model metal-

graphene nanocomposites [46, 47]. This leaves the door open to model nanocomposites reinforced with polycrystalline graphene, and to compare their reinforcing ability to that of pristine graphene.

2.3 Carbyne

Carbyne is a carbon chain with alternating single and triple bonds while in its polyyne form, and repeated double bonds in its cumulene form [48]. Though both kinds of carbyne are predicted to have fantastic mechanical properties [49, 50], they also have differences that fuel separate research into both types. For example, polyyne is predicted to behave electrically like a semiconductor while cumulene behaves more like a metal [51]. Polyyne chains have been investigated more heavily as they tend to be more stable [50]. Strategies to increase cumulene's stability include careful choice of end groups [52] and rotaxination [53]. Additionally, on some transition metal surfaces cumulene has been predicted to be energetically favorable over polyyne [54].

Owing to carbyne's chemical instability [55-57], most studies investigating its mechanical properties thus far obtained them computationally [58]. Liu et al. performed an extensive first principles study on the mechanical properties of carbyne using density functional theory (DFT) [59]. In their work the Young's modulus of carbyne is predicted to be an order of magnitude higher than that of graphene and the specific stiffness is more than twice that of graphene and three times that of diamond. They also found that carbyne's persistence length is 14 nm, which would consist of around 110 C atoms. This makes carbyne a very stiff polymer. Mechanical properties for carbyne were also investigated using MD simulations by Nair et al. [60]. They identified a size-dependent strength inherent in carbyne, which peaks with shorter chains and decreases with chain length.

The main challenge in fabricating carbyne chains is in their tendency to either decompose or polymerize [57]. This can be addressed by including end groups for carbyne chains [57, 61, 62], though the number of atoms in a single chain using this method has so far been small (less than 25 C atoms). The properties of these short chains vary widely depending on their length and structure, allowing for some tunability [63]. The longest carbyne chains that have been fabricated contained more than 6400 atoms, and were grown within double wall carbon nanotubes [64]. The properties of carbyne chain thus encapsulated are partially dependent on the properties of the carbon nanotubes, such as their chirality and the diameter of the inner nanotube [65].

Carbyne has many potential applications including high resolution DNA sequencing [66] and hydrogen storage [67]. Most commonly carbyne has been considered for use as both an electrical and mechanical junction between larger components [68, 69]. While the practical use of carbyne is still mostly theoretical, we can look to the history of graphene to show how quickly theory can be converted to application. Before 2004 research into graphene was done without a direct opportunity for application; now applications for graphene are widespread. By 2008 at least two papers were published every day on graphene composites alone [23]. Another such acceleration in research may begin when the synthesis of stable carbyne becomes more viable.

Before carbyne can be used in nanocomposites, the environmental factors affecting carbyne's stability need to be further investigated. Carbyne is expensive to produce, and potentially explosive even in airless environments [57]. Computational models offer a low-cost and safe method for investigating the properties of carbyne in proximity to other materials. Tarakeshwar et al. used DFT to model carbyne in the presence of gold clusters and found that carbyne's charge structure was stabilized, but also changed so significantly that they denote such chains "pseudocarbyne" [70]. Other materials should be investigated to determine how radically

carbyne's structure will be affected by potential matrix materials. In addition, up to this point, no one has directly investigated the mechanical properties that carbyne might contribute as part of a nanocomposite. Such research can help motivate work on carbyne synthesis and provide a glimpse into future applications.

2.4 Al/a-Si core-shell nanorods

Metals are known to exhibit surprising behavior when their features are nanoscopic. Examples include material strengthening through dislocation starvation [71, 72], increased hardness when placed within a multilayer laminate [73], and different deformation mechanisms at different material sizes [74]. The unique behavior of nanocomposites composed of metals and metalloids with features at the nanoscale is an area of intense and ongoing research. These materials can be used in strengthened nanotextured surfaces for tribological applications.

The natural world is full of surfaces with amazing properties due to texturing at the nanoscale [75]. Researchers have been able to replicate and expand on features found in biology and have shown that nanotexturing can produce contacting surfaces with greatly reduced friction and adhesion [76-82]. However, there are drawbacks to having features at the nanoscale. The forces caused by friction become more significant as the surface-to-volume ratio increases [83, 84], producing early wear and loss of the textured surface and its tribological contributions. One method for preserving nanotextured surfaces is by adding coatings to the material surface. Many different coating materials can be used for this purpose including polymers [85], and metalloids [86]. The resulting coated nanotextured surface is a nanocomposite with the coating material improving strength and wear resistance while the underlying material providing toughness.

Tidwell et al. produced Al/amorphous-Si (Al/a-Si) core-shell nanostructures by fabricating Al nanodots and coating them with an a-Si shell [87]. These nanostructures were found to be deformation resistant under indentation, and therefore a strong candidate for nanotextured surface design. Fleming et al. performed experiments on the same types of nanostructures and found that they exhibited unique properties [88, 89]. They found that the nanostructure exhibited recovery after deformations beyond the elastic limit. This effect was most pronounced in nanostructures with smallest core volume, and that it was suppressed with increasing core volume. Fleming et al. point out several possible mechanisms at work in the observed nanostructure recovery. They theorize that this effect could be caused by stress fields generated by dislocation piling at grain boundaries within the Al core. Unfortunately, grain boundaries in MD simulations are small enough that they cannot be used to test the theorized mechanism for the effect they observe. Other possible mechanisms for nanostructure recovery include dislocation absorption by the Al/a-Si interface or annihilation through reactions with other dislocations. They observed some of these effects using an MD model of their sample, albeit a smaller version.

The recovery of Al/a-Si core-shell nanostructures/nanorods could be simulated for larger geometries than those achieved by Fleming et al. using a multiscale model to capture both indentation at the atomistic scale and its effects at the length scale of experimental observations. The deformation of specific members of the core-shell structure (core, shell and substrate) can also be investigated for different core and shell sizes to better understand the indentation and retraction behavior of these nanocomposites.

References

[1] M.J. Allen, V.C. Tung, R.B. Kaner, Honeycomb carbon: a review of graphene, Chemical reviews 110(1) (2009) 132-145.

[2] D. Akinwande, C.J. Brennan, J.S. Bunch, P. Egberts, J.R. Felts, H. Gao, R. Huang, J.-S. Kim, T. Li, Y. Li, A review on mechanics and mechanical properties of 2D materials—Graphene and beyond, Extreme Mechanics Letters 13 (2017) 42-77.

[3] A.K. Geim, K.S. Novoselov, The rise of graphene, Nat Mater 6(3) (2007) 183-91.

[4] K.S. Novoselov, V. Fal, L. Colombo, P. Gellert, M. Schwab, K. Kim, A roadmap for graphene, nature 490(7419) (2012) 192-200.

[5] M. Yi, Z. Shen, A review on mechanical exfoliation for the scalable production of graphene, Journal of Materials Chemistry A 3(22) (2015) 11700-11715.

[6] M. Yi, Z. Shen, Fluid dynamics: an emerging route for the scalable production of graphene in the last five years, RSC Advances 6(76) (2016) 72525-72536.

[7] S. Hofmann, P. Braeuninger-Weimer, R.S. Weatherup, CVD-enabled graphene manufacture and technology, The journal of physical chemistry letters 6(14) (2015) 2714-2721.

[8] J. De La Fuente, CVD Graphene-Creating Graphene via Chemical Vapour Deposition, Graphenea, 2016.

[9] X. Li, W. Cai, J. An, S. Kim, J. Nah, D. Yang, R. Piner, A. Velamakanni, I. Jung, E. Tutuc, S.K. Banerjee, L. Colombo, R.S. Ruoff, Large-area synthesis of high-quality and uniform graphene films on copper foils, Science 324(5932) (2009) 1312-4.

[10] L. Huang, Q. Chang, G. Guo, Y. Liu, Y. Xie, T. Wang, B. Ling, H. Yang, Synthesis of high-quality graphene films on nickel foils by rapid thermal chemical vapor deposition, Carbon 50(2) (2012) 551-556.

[11] A. Reina, X. Jia, J. Ho, D. Nezich, H. Son, V. Bulovic, M.S. Dresselhaus, J. Kong, Large area, few-layer graphene films on arbitrary substrates by chemical vapor deposition, Nano letters 9(1) (2008) 30-35.

[12] Y. Zhang, L. Gomez, F.N. Ishikawa, A. Madaria, K. Ryu, C. Wang, A. Badmaev, C. Zhou, Comparison of graphene growth on single-crystalline and polycrystalline Ni by chemical vapor deposition, The Journal of Physical Chemistry Letters 1(20) (2010) 3101-3107.

[13] S.J. Chae, F. Güneş, K.K. Kim, E.S. Kim, G.H. Han, S.M. Kim, H.J. Shin, S.M. Yoon, J.Y. Choi, M.H. Park, Synthesis of large-area graphene layers on poly-nickel substrate by chemical vapor deposition: wrinkle formation, Advanced Materials 21(22) (2009) 2328-2333.

[14] C. Lee, X.D. Wei, J.W. Kysar, J. Hone, Measurement of the elastic properties and intrinsic strength of monolayer graphene, Science 321 (2008) 385-388.

[15] K. Kim, Z. Lee, W. Regan, C. Kisielowski, M. Crommie, A. Zettl, Grain boundary mapping in polycrystalline graphene, ACS nano 5(3) (2011) 2142-2146.

[16] H.I. Rasool, C. Ophus, W.S. Klug, A. Zettl, J.K. Gimzewski, Measurement of the intrinsic strength of crystalline and polycrystalline graphene, Nature communications 4 (2013) 2811.

[17] J. Zhang, J. Zhao, J. Lu, Intrinsic strength and failure behaviors of graphene grain boundaries, ACS Nano 6(3) (2012) 2704-11.

[18] G.H. Lee, R.C. Cooper, S.J. An, S. Lee, A. van der Zande, N. Petrone, A.G. Hammerberg, C. Lee, B. Crawford, W. Oliver, J.W. Kysar, J. Hone, High-strength chemical-vapor-deposited graphene and grain boundaries, Science 340(6136) (2013) 1073-6.

[19] A. Zandiatashbar, G.H. Lee, S.J. An, S. Lee, N. Mathew, M. Terrones, T. Hayashi, C.R. Picu, J. Hone, N. Koratkar, Effect of defects on the intrinsic strength and stiffness of graphene, Nature communications 5 (2014) 3186.

[20] G. Lopez-Polin, C. Gomez-Navarro, V. Parente, F. Guinea, M.I. Katsnelson, F. Perez-Murano, J. Gomez-Herrero, Increasing the elastic modulus of graphene by controlled defect creation, Nature Physics 11(1) (2015) 26-31.

[21] A. Shekhawat, R.O. Ritchie, Toughness and strength of nanocrystalline graphene, Nature communications 7 (2016) 10546.

[22] A. Molle, J. Goldberger, M. Houssa, Y. Xu, S.-C. Zhang, D. Akinwande, Buckled two-dimensional Xene sheets, Nature Materials 16(2) (2017) 163-169.

[23] H. Kim, A.A. Abdala, C.W. Macosko, Graphene/Polymer Nanocomposites, Macromolecules 43(16) (2010) 6515-6530.

[24] G. Mittal, V. Dhand, K.Y. Rhee, S.-J. Park, W.R. Lee, A review on carbon nanotubes and graphene as fillers in reinforced polymer nanocomposites, Journal of Industrial and Engineering Chemistry 21 (2015) 11-25.

[25] Z. Li, Q. Guo, Z. Li, G. Fan, D.-B. Xiong, Y. Su, J. Zhang, D. Zhang, Enhanced mechanical properties of graphene (reduced graphene oxide)/aluminum composites with a bioinspired nanolaminated structure, Nano letters 15(12) (2015) 8077-8083.

[26] S.F. Bartolucci, J. Paras, M.A. Rafiee, J. Rafiee, S. Lee, D. Kapoor, N. Koratkar, Graphene–aluminum nanocomposites, Materials Science and Engineering: A 528(27) (2011) 7933-7937.

[27] F. Khodabakhshi, S. Arab, P. Švec, A. Gerlich, Fabrication of a new Al-Mg/graphene nanocomposite by multi-pass friction-stir processing: Dispersion, microstructure, stability, and strengthening, Materials Characterization 132 (2017) 92-107.

[28] K. Yan, H. Peng, Y. Zhou, H. Li, Z. Liu, Formation of bilayer bernal graphene: layer-by-layer epitaxy via chemical vapor deposition, Nano letters 11(3) (2011) 1106-1110.

[29] D.-B. Xiong, M. Cao, Q. Guo, Z. Tan, G. Fan, Z. Li, D. Zhang, High content reduced graphene oxide reinforced copper with a bioinspired nano-laminated structure and large recoverable deformation ability, Scientific reports 6 (2016) 33801.

[30] F. Bonaccorso, L. Colombo, G. Yu, M. Stoller, V. Tozzini, A.C. Ferrari, R.S. Ruoff, V. Pellegrini, Graphene, related two-dimensional crystals, and hybrid systems for energy conversion and storage, Science 347(6217) (2015) 1246501.

[31] I. Vlassiouk, G. Polizos, R. Cooper, I. Ivanov, J.K. Keum, F. Paulauskas, P. Datskos, S. Smirnov, Strong and electrically conductive graphene-based composite fibers and laminates, ACS applied materials & interfaces 7(20) (2015) 10702-10709.

[32] S. Feng, Q. Guo, Z. Li, G. Fan, Z. Li, D.-B. Xiong, Y. Su, Z. Tan, J. Zhang, D. Zhang, Strengthening and toughening mechanisms in graphene-Al nanolaminated composite micro-pillars, Acta Materialia 125 (2017) 98-108.

[33] W. Gao, The chemistry of graphene oxide, Graphene oxide, Springer2015, pp. 61-95.

[34] V. Georgakilas, J.N. Tiwari, K.C. Kemp, J.A. Perman, A.B. Bourlinos, K.S. Kim, R. Zboril, Noncovalent functionalization of graphene and graphene oxide for energy materials, biosensing, catalytic, and biomedical applications, Chemical reviews 116(9) (2016) 5464-5519.

[35] Y. Kim, J. Lee, M.S. Yeom, J.W. Shin, H. Kim, Y. Cui, J.W. Kysar, J. Hone, Y. Jung, S. Jeon, S.M. Han, Strengthening effect of single-atomic-layer graphene in metal-graphene nanolayered composites, Nature communications 4 (2013) 2114.

[36] S.W. Chang, A.K. Nair, M.J. Buehler, Nanoindentation study of size effects in nickel-graphene nanocomposites, Phil Mag Lett 93(4) (2013) 196-203.

[37] D.-B. Xiong, M. Cao, Q. Guo, Z. Tan, G. Fan, Z. Li, D. Zhang, Graphene-and-copper artificial nacre fabricated by a preform impregnation process: bioinspired strategy for strengthening-toughening of metal matrix composite, Acs Nano 9(7) (2015) 6934-6943.

[38] Z. Hu, G. Tong, D. Lin, C. Chen, H. Guo, J. Xu, L. Zhou, Graphene-reinforced metal matrix nanocomposites–a review, Materials Science and Technology 32(9) (2016) 930-953.

[39] I. Ovid'Ko, A. Sheinerman, Competition between plastic deformation and fracture processes in metal–graphene layered composites, Journal of Physics D: Applied Physics 47(49) (2014) 495302.

[40] K. Chu, J. Wang, Y.-p. Liu, Z.-r. Geng, Graphene defect engineering for optimizing the interface and mechanical properties of graphene/copper composites, Carbon 140 (2018) 112-123.

[41] A.C. Van Duin, S. Dasgupta, F. Lorant, W.A. Goddard, ReaxFF: a reactive force field for hydrocarbons, The Journal of Physical Chemistry A 105(41) (2001) 9396-9409.

[42] M. Chen, S. Quek, Z. Sha, C. Chiu, Q. Pei, Y. Zhang, Effects of grain size, temperature and strain rate on the mechanical properties of polycrystalline graphene–A molecular dynamics study, Carbon 85 (2015) 135-146.

[43] Z. Song, V.I. Artyukhov, B.I. Yakobson, Z. Xu, Pseudo Hall–Petch strength reduction in polycrystalline graphene, Nano letters 13(4) (2013) 1829-1833.

[44] G. Jung, Z. Qin, M.J. Buehler, Molecular mechanics of polycrystalline graphene with enhanced fracture toughness, Extreme Mechanics Letters 2 (2015) 52-59.

[45] A. Alian, S. Meguid, Hybrid molecular dynamics–finite element simulations of the elastic behavior of polycrystalline graphene, International Journal of Mechanics and Materials in Design (2017) 1-13.

[46] S. Dixit, A. Mahata, D.R. Mahapatra, S.V. Kailas, K. Chattopadhyay, Multi-layer graphene reinforced aluminum–Manufacturing of high strength composite by friction stir alloying, Composites Part B: Engineering 136 (2018) 63-71.

[47] A. Mokhalingam, D. Kumar, A. Srivastava, Mechanical Behaviour of Graphene Reinforced Aluminum Nano composites, Materials Today: Proceedings 4(2) (2017) 3952-3958.

[48] S. Hino, Y. Okada, K. Iwasaki, M. Kijima, H. Shirakawa, Electronic structures of cumulene type carbyne model compounds: a typical example of one-dimensional quantum well, Chemical physics letters 372(1-2) (2003) 59-65.

[49] A. Timoshevskii, S. Kotrechko, Y. Matviychuk, Atomic structure and mechanical properties of carbyne, Phys Rev B 91(24) (2015).

[50] X. Liu, G. Zhang, Y.-W. Zhang, Tunable mechanical and thermal properties of one-dimensional carbyne chain: Phase transition and microscopic dynamics, The Journal of Physical Chemistry C 119(42) (2015) 24156-24164.

[51] A. Milani, M. Tommasini, V. Barbieri, A. Lucotti, V. Russo, F. Cataldo, C.S. Casari, Semiconductor-to-metal transition in carbon-atom wires driven by sp2 conjugated end groups, The Journal of Physical Chemistry C 121(19) (2017) 10562-10570.

[52] D. Wendinger, R.R. Tykwinski, Odd [n] Cumulenes (n= 3, 5, 7, 9): synthesis, characterization, and reactivity, Accounts of chemical research 50(6) (2017) 1468-1479.

[53] M. Franz, J.A. Januszewski, D. Wendinger, C. Neiss, L.D. Movsisyan, F. Hampel, H.L. Anderson, A. Görling, R.R. Tykwinski, Cumulene rotaxanes: stabilization and study of [9] cumulenes, Angewandte Chemie International Edition 54(22) (2015) 6645-6649.

[54] Q. Yuan, F. Ding, Formation of carbyne and graphyne on transition metal surfaces, Nanoscale 6(21) (2014) 12727-12731.

[55] C.S. Casari, M. Tommasini, R.R. Tykwinski, A. Milani, Carbon-atom wires: 1-D systems with tunabble properties, Nanoscale 8(8) (2016) 4414-4435.

[56] D.A. Prenzel, Synthesis and Investigation of New Carbon Allotropes on Surface, in Solution, and in the Gas Phase, 2016.

[57] D. Prenzel, R.W. Kirschbaum, W.A. Chalifoux, R. McDonald, M.J. Ferguson, T. Drewello, R.R. Tykwinski, Polymerization of acetylene: polyynes, but not carbyne, Organic Chemistry Frontiers 4(5) (2017) 668-674.

[58] F. Banhart, Chains of carbon atoms: A vision or a new nanomaterial?, Beilstein journal of nanotechnology 6(1) (2015) 559-569.

[59] M. Liu, V.I. Artyukhov, H. Lee, F. Xu, B.I. Yakobson, Carbyne from first principles: chain of C atoms, a nanorod or a nanorope, ACS Nano 7(11) (2013) 10075-82.

[60] A.K. Nair, S.W. Cranford, M.J. Buehler, The minimal nanowire: Mechanical properties of carbyne, Epl 95(1) (2011).

[61] J.A. Januszewski, D. Wendinger, C.D. Methfessel, F. Hampel, R.R. Tykwinski, Synthesis and Structure of Tetraarylcumulenes: Characterization of Bond-Length Alternation versus Molecule Length, Angewandte Chemie International Edition 52(6) (2013) 1817-1821.

[62] W.A. Chalifoux, R.R. Tykwinski, Synthesis of polyynes to model the sp-carbon allotrope carbyne, Nat Chem 2(11) (2010) 967-71.

[63] C.S. Casari, A. MIlani, Carbyne: from the elusive allotrope to stable carbon atom wires, MRS Communications (2018) 1-13.

[64] L. Shi, P. Rohringer, K. Suenaga, Y. Niimi, J. Kotakoski, J.C. Meyer, H. Peterlik, M. Wanko, S. Cahangirov, A. Rubio, Confined linear carbon chains as a route to bulk carbyne, Nature materials 15(6) (2016) 634-639.

[65] S. Heeg, L. Shi, L.V. Poulikakos, T. Pichler, L. Novotny, Carbon nanotube chirality determines properties of encapsulated linear carbon chain, Nano letters 18(9) (2018) 5426-5431.

[66] Z. Salman, A. Nair, S. Tung, One-dimensional carbon chains as electrical sensors for single-stranded DNA, Nano/Micro Engineered and Molecular Systems (NEMS), 2017 IEEE 12th International Conference on, IEEE, 2017, pp. 677-681.

[67] P.B. Sorokin, H. Lee, L.Y. Antipina, A.K. Singh, B.I. Yakobson, Calcium-decorated carbyne networks as hydrogen storage media, Nano letters 11(7) (2011) 2660-2665.

[68] A. Nitzan, M.A. Ratner, Electron transport in molecular wire junctions, Science 300(5624) (2003) 1384-1389.

[69] G. Zhang, X. Fang, Y. Yao, C. Wang, Z. Ding, K. Ho, Electronic structure and transport of a carbon chain between graphene nanoribbon leads, Journal of Physics: Condensed Matter 23(2) (2010) 025302.

[70] P. Tarakeshwar, P.R. Buseck, H.W. Kroto, Pseudocarbynes: charge-stabilized carbon chains, The journal of physical chemistry letters 7(9) (2016) 1675-1681.

[71] K.J. Hemker, W.D. Nix, Nanoscale deformation: seeing is believing, Nature materials 7(2) (2008) 97-98.

[72] W.D. Nix, J.R. Greer, G. Feng, E.T. Lilleodden, Deformation at the nanometer and micrometer length scales: Effects of strain gradients and dislocation starvation, Thin Solid Films 515(6) (2007) 3152-3157.

[73] D. Mordehai, M. Kazakevich, D.J. Srolovitz, E. Rabkin, Nanoindentation size effect in single-crystal nanoparticles and thin films: A comparative experimental and simulation study, Acta Materialia 59(6) (2011) 2309-2321.

[74] A. Misra, R. Hoagland, Plastic flow stability of metallic nanolaminate composites, Journal of materials science 42(5) (2007) 1765-1771.

[75] J. Sun, B. Bhushan, Nanomanufacturing of bioinspired surfaces, Tribology International 129 (2019) 67-74.

[76] M. Kang, Y.M. Park, B.H. Kim, Y.H. Seo, Micro-and nanoscale surface texturing effects on surface friction, Applied Surface Science 345 (2015) 344-348.

[77] M. Shafiei, A.T. Alpas, Nanocrystalline nickel films with lotus leaf texture for superhydrophobic and low friction surfaces, Applied Surface Science 256(3) (2009) 710-719.

[78] R.P. Nair, M. Zou, Surface-nano-texturing by aluminum-induced crystallization of amorphous silicon, Surface and Coatings Technology 203(5-7) (2008) 675-679.

[79] M. Zou, L. Cai, H. Wang, Adhesion and friction studies of a nano-textured surface produced by spin coating of colloidal silica nanoparticle solution, Tribology Letters 21(1) (2006) 25.

[80] M. Zou, L. Cai, H. Wang, D. Yang, T. Wyrobek, Adhesion and friction studies of a selectively micro/nano-textured surface produced by UV assisted crystallization of amorphous silicon, Tribology Letters 20(1) (2005) 43-52.

[81] B. Bhushan, Y.C. Jung, Natural and biomimetic artificial surfaces for superhydrophobicity, self-cleaning, low adhesion, and drag reduction, Progress in Materials Science 56(1) (2011) 1-108.

[82] N. Lin, D. Li, J. Zou, R. Xie, Z. Wang, B. Tang, Surface texture-based surface treatments on Ti6Al4V titanium alloys for tribological and biological applications: A mini review, Materials 11(4) (2018) 487.

[83] Z. Guo, Y. Meng, C. Su, H. Wu, An on-chip micro-friction tester for tribology research of silicon based MEMS devices, Microsystem Technologies 14(1) (2008) 109-118.

[84] L. Chen, J. Zhang, Design and properties of self-assembled ordered films for nanolubrication, Surfactants in tribology 4 (2015) 97-150.

[85] K. Ellinas, S.P. Pujari, D.A. Dragatogiannis, C.A. Charitidis, A. Tserepi, H. Zuilhof, E. Gogolides, Plasma micro-nanotextured, scratch, water and hexadecane resistant, superhydrophobic, and superamphiphobic polymeric surfaces with perfluorinated monolayers, ACS applied materials & interfaces 6(9) (2014) 6510-6524.

[86] R.A. Fleming, M. Zou, Nanostructure-Textured Surfaces with Low Friction and High Deformation Resistance, Tribology Transactions 61(1) (2018) 80-87.

[87] W. Tidwell, D. Scott, H. Wang, R. Fleming, M. Zou, Nanoindentation study of deformation-resistant Al/a-Si core–shell nanostructures, Acta Materialia 59(15) (2011) 6110-6116.

[88] R.A. Fleming, M. Zou, The effects of confined core volume on the mechanical behavior of Al/a-Si core-shell nanostructures, Acta Materialia 128 (2017) 149-159.

[89] R.A. Fleming, J.A. Goss, M. Zou, Material dimensionality effects on the nanoindentation behavior of Al/a-Si core-shell nanostructures, Applied Surface Science 412 (2017) 96-104.

Chapter 3

Computational Methods

Many of the specifics of the computational methods used in this research are discussed in the individual papers (chapters 4-7). This chapter provides a broad overview of the computational methods used in this work to provide context for the work discussed in later chapters. Molecular dynamics and subcategories related to this method are discussed first (later utilized in chapters 4, 5 and 7). The "patchwork quilt" method for generating the polycrystalline graphene sheets used in chapter 5 is also presented. Density functional theory is then discussed, along with some basic principles associated with this method (later utilized in chapter 6). Finally, the coupled atomistic and discrete dislocation method is presented (later utilized in chapter 7).

3.1 Molecular dynamics

Molecular dynamics (MD) is a commonly used atomistic method for modeling a large variety of material phenomena in the Å to sub-micron range [1]. These phenomena include dislocation nucleation [2], crack propagation [3] and amorphous structures [4]. The simulations developed in chapters 4 and 5 use MD exclusively, while simulations in chapter 7 use MD as part of a multiscale model. MD lacks the precision of quantum mechanical methods, but it is far less computationally expensive, and can operate at higher length and time scales. All MD simulations in this work are performed using the Large-scale Atomic/Molecular Massively Parallel Simulator (LAMMPS) [1].

3.1.1 Interatomic potentials

The atomic motion in MD is governed by Newton's 2nd Law, based on forces derived from the potential energy of the atoms. Thus, MD treats atoms as classical particles, ignoring quantum

effects in a direct sense, though quantum mechanical methods such as density functional theory are often used to derive potentials for MD. A "potential" is a function that describes an atom's potential energy based on its neighbors, environment, bonding, charge, etc. Choosing an appropriate potential is key to developing an accurate MD model.

For metals, the embedded atom method (EAM) [5] is commonly used to capture the behavior of metallic bonding. EAM is a semiempirical multibody potential where an atom's energy is a combination of the local electron density and a pair-wise potential based on neighboring atoms. EAM potentials have been developed for many different metals, and computed properties such as lattice constants, elastic constants, vacancy formation energies, and surface energies are in good agreement with experiment [6]. One of the main limitations to EAM is an inability to model dynamic changes to bonding, such as might occur between different types of atoms in alloyed materials [7]. This is less of a concern if interactions between the unlike materials are non-bonding van der Waals interactions, as is the case between Ni and graphene [8-12]. Thus, an EAM potential is used for Ni-Ni interactions in the Ni-graphene simulations of chapters 4 and 5.

The modified EAM potential (MEAM) is similar to EAM, but with angular dependencies included [13]. MEAM can still predict the mechanical properties of metals similar to EAM and in good agreement with experiment [13-15], but it is also able to consider some directional bonding, allowing for modeling some nonmetallic systems [16]. MEAM potentials have also been used to model amorphous metals and alloys [17-19], with some improvement over EAM [18]. An MEAM potential is used for all interactions in the MD part of the multiscale model developed for Al/amorphous-Si (Al/a-Si) in chapter 7.

For covalently bonded carbon-based polymers, a good choice of potential is the adaptive intermolecular reactive empirical bond order (AIREBO) potential [20]. This potential includes a

torsional term, a reactive bond order term for short-range interactions, and a Lennard-Jones term for long range interactions. AIREBO can be implemented alongside EAM, which is why it is the chosen potential for C-C interactions in the Ni-graphene simulations of chapters 4 and 5.

A Lennard-Jones potential is often used for materials which interact primarily through van der Waals interactions. This is generally the relationship between graphene and Ni. There are numerous examples of Lennard-Jones potentials being used to model interactions between Ni and graphene in recent computational research [21-28]. A Lennard-Jones potential is used for the Ni-C interactions in chapters 4 and 5. Other factors related to this potential are discussed in section 5.2.4.

3.1.2 Virial stress calculations

The per-atom stresses obtained in chapters 4 and 5 are calculated from the virial definition of stress given by Thompson et al. [29]. This is a measure of the average stress of each atom in a group for a periodic system. One of the main advantages of this method for calculating stress is that it is independent of the interatomic potential being used [30], which is ideal when using more complex hybrid potential systems, as is done in chapters 4 and 5.

3.1.3 Common neighbor analysis and centrosymmetry

When identifying deformations in crystalline systems, it is useful to have a way to visually identify different crystal structures, such as FCC or BCC. Faken et al. outlined the method of common neighbor analysis (CNA) whereby an atom's local structure can be identified based on its local structural environment [31], with a cutoff radius determining what constitutes that environment. A more advanced version of this is Adaptive CNA where an optimal cutoff radius is

used for each particle [32]. This method is used to identify and visualize dislocations in chapter 4, as implemented from the open source software OVITO [33].

Another way to quantify disorder in a crystalline system is using the centrosymmetry parameter [34]. This parameter characterizes local lattice disorder from a given crystal structure (such as FCC). The value for the centrosymmetry of an atom is on a spectrum where zero is a perfect lattice and larger numbers correspond to the degree to which the atom is out-of-lattice. This is different from CNA, where atoms are discretely part of a crystal group (FCC, BCC, etc.) or simply labeled as "Other". Centrosymmetry is useful when it is important to know the degree to which atoms are disordered rather than simply knowing their structure type. Centrosymmetry is used to identify and visualize dislocations and disorder in chapters 5 and 7.

3.1.4 Generating polycrystalline graphene by Voronoi tessellation

Multiple different polycrystalline sheets are generated for simulations in chapter 5. The method used to produce one of these sheets is analogous to making a patchwork quilt, to which polycrystalline graphene has been compared [35, 36]. Each differently oriented grain in this analogy is a patch of the quilt.

The first step in the "patchwork quilt" process for generating polycrystalline graphene is to produce a pattern for the polycrystalline sheet. This is done using periodic Voronoi tessellation. Voronoi tessellation is a process for partitioning a 2-D space such that a set of seed points are bounded within regions, where all space in a given region is closer to the seed point enclosed within that region than to any other seed point. Voronoi tessellation is performed using the open source software Voro++ [37]. A set of seed points are passed to the program as input, and vertices for polycrystalline grain partitions are returned as output. The grain vertices are then sorted

counterclockwise (CCW), and a set of vectors connecting the edges of each vertex are recorded for each grain.

After acquiring vertices and CCW vectors for each grain, an atomic coordinate file is produced for a single graphene sheets using Python. A copy of this sheet is produced for each grain, and then rotated at a random angle between 0° and 30° (this covers all possible rotations of graphene based on its symmetry [38]). Grains are generated by removing all atoms from the copied sheet that are not enclosed by the grain vectors recorded earlier. This is done in two stages for each grain. In the first stage, all atoms that are above the topmost vertex, below the bottommost vertex, left of the leftmost vertex and right of the rightmost vertex are removed. The remaining atoms form a square enclosing the grain's vertices. In the second stage, each atom has a vector drawn from each grain vertex. The cross product of the grain vector for that vertex and the vertex-to-atom vector is also taken for each vertex. If the cross product related to each vertex is greater than zero, then the atom is within the boundaries of the grain and it is kept as part of that grain. If any cross product is less than zero, the atom is outside the grain and it is removed. A schematic of this process is shown in Figure 3.1 for two example atoms.

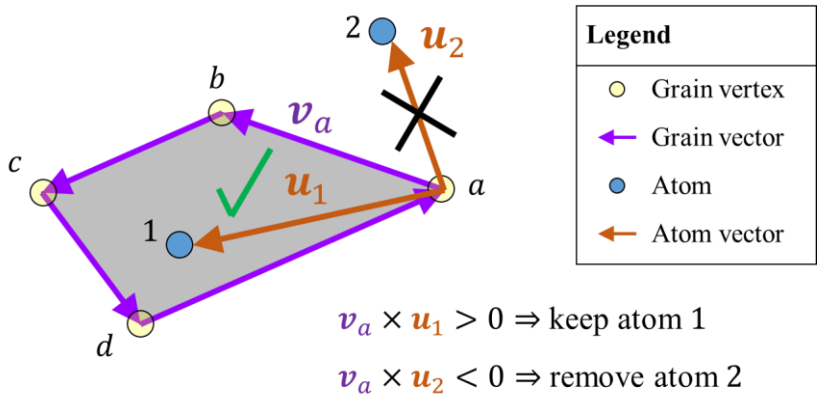

Figure 3.1. Schematic showing how atoms 1 and 2 are either included or excluded depending on whether the cross product of grain vectors with vertex-to-atom vectors are greater than or less than zero. For an atom to be included it must pass this test for each grain vertex, which in this example is vertices *a*, *b*, *c* and *d*.

Because each grain is from an independent sheet, the process of preparing grains can be performed in parallel, which is convenient for polycrystalline sheets that are large and/or have many grains. After all grain are prepared, they are assembled into a single atomic coordinate file containing a polycrystalline graphene sheet. The polycrystalline sheet can then be relaxed in MD to equilibrate grain boundaries. Figure 3.2(a) shows the starting Voronoi diagram pattern for a polycrystalline sheet, with the final polycrystalline graphene sheet generated from that pattern shown in Figure 3.2(b-c).

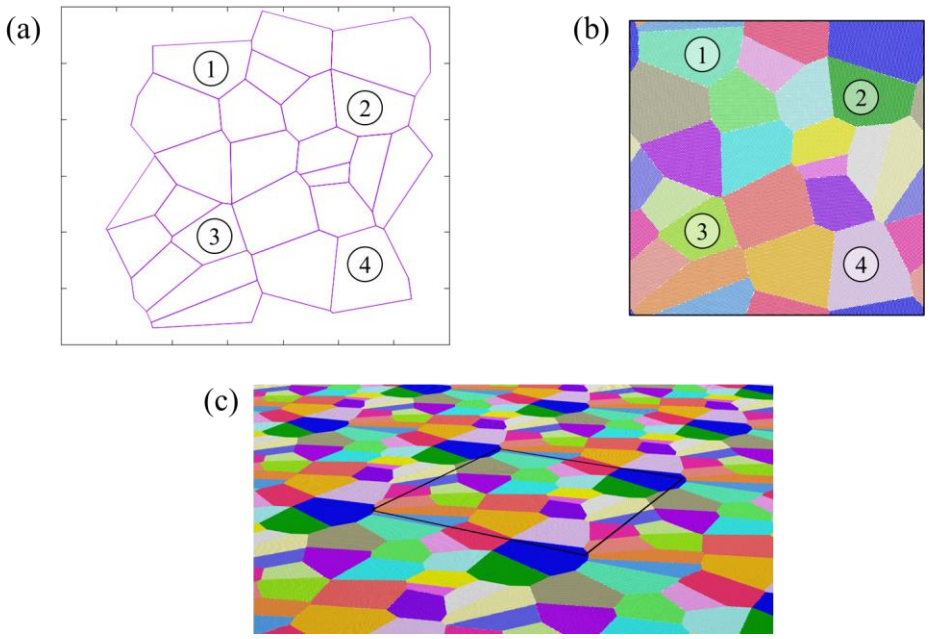

Figure 3.2. (a) Voronoi diagram produced by Voro++ for a 25 grain polycrystalline sheet with dimensions 500 × 500 Å and periodic boundaries. (b) Final polycrystalline graphene sheet based on Voronoi diagram. The grains labeled 1, 2, 3, 4 in (a) and (b) are included to allow readers to easily connect the diagram in (a) to the periodic polycrystalline sheet in (b). (c) Perspective view of polycrystalline sheet with periodic images shown, demonstrating the periodicity of the generated sheet. The black boundary shows the dimensions of the original sheet.

3.2 Density functional theory

In general, MD cuts computational costs by not accounting for individual electrons and by neglecting quantum mechanical effects. Many MD potentials, such as ReaxFF, derive interatomic behavior from higher order methods [39], which allows for some chemical effects such as bond

breaking. But these potentials cannot incorporate atom combinations for which they are not prepared. To analyze unknown chemical reactions and atomic behavior to a high level of accuracy requires that electron behavior and quantum mechanics be considered explicitly. However, simulations where Schrodinger's Equation is solved for electrons in every atomic shell becomes unwieldy for all but the simplest of problems. Density functional theory (DFT) considers electrons as an electron density around the nuclei rather than individual electrons. This reduces the $3N$ degrees of freedom needed for a system of N electrons to 3 degrees of freedom, which greatly cuts down on complexity and computation time. The most popular methods in computational quantum mechanics today utilize DFT, with Kohn-Sham's method [40] being the most common [7]. DFT is used to model the carbyne-Ni nanocomposite in chapter 6 due to the present lack of interatomic potentials for C and Ni in MD that can also capture carbyne's structure. The DFT simulation in that chapter is implemented using Quantum-Espresso [41].

3.2.1 Exchange-correlation functional

A correction to the Kohn-Sham Hamiltonian is required with the approximation of individual electrons as an electron density; it is called the exchange-correlation functional [7]. The two most commonly used types of exchange-correlation functionals are the local-density approximation (LDA) and the generalized gradient approximation (GGA). For LDA, the functional depends only on the local density. This can result in some problems, such as LDA's tendency to overbind [42]. GGA corrects for this by including both the local density and its gradient, which can lead to improved accuracy [43]. Some GGA functionals are parametrized to fit experimental data, but the GGA functional developed by Perdew, Burke and Ernzerhof (PBE) allows for more flexibility in choice of system by using fundamental constants as parameters [44]. A PBE functional is used for C and Ni atoms in the DFT simulations of chapter 6.

3.2.2 Pseudopotentials

One simplification often made in DFT is to consider only valence bands in simulated atoms, treating the inner electron shells and nucleus as an inert, yet charged, core [7]. Interactions between valence electrons and the core are governed by pseudopotentials. These pseudopotentials can vary in the way they are prepared, such as including relativistic effects [45]. One way to improve computational efficiency is by incorporating the projector augmented wave (PAW) method when developing pseudopotentials [46]. PAW is used to smooth the wave function near the atomic core, which allows for fewer Fourier components to achieve a good approximation. The pseudopotentials used in chapter 6 have PAW incorporated in them.

3.2.3 Correction for van der Waals interactions

One limitation of typical GGA functionals is that they do not allow for long-range van der Waals interactions. This is a problem for modeling materials that are expected to interact primarily through van der Waals interactions, such as graphene and Ni. Grimme introduced a semiempirical dispersive term that can be added to the total energy of the DFT system to correct for van der Waals forces [47]. The dispersion correction is incorporated in the model of chapter 6.

3.2.4 Bader charge analysis

In the quantum theory of atoms in molecules (QTAIM), space is divided into atomic regions based on the topology of the electron charge density [48]. QTAIM is the basis for Bader charge analysis, which is used to separate space into atomic volumes based on surfaces over which the flux of the gradient of the electron density approaches zero (also called a “zero flux” surface) [49-52]. In this way the overall charge density can be split into separate Bader volumes, and the local charge of atoms can be approximated, as is done in chapter 6.

3.3 Coupled atomistic and discrete dislocation method (CADD)

MD is a substantial length and time scale improvement over DFT, but it still has limitations. The typical length scale limit of MD is around 100 nm, and the upper limit of that scale requires incredible computational time that is unfeasible for most research problems. On the other hand, continuum models can operate effectively from the μm range to the macroscale. Multiscale methods seek to combine two length scales so that one provides inputs and boundary conditions for the other (usually from smaller scale to larger scale). In this way researchers can observe and explain macroscopic behavior based on nanoscopic principles. The coupled atomistic and discrete dislocation (CADD) method is a multiscale model that couples an atomistic region to a continuum region [53-55].

Multiscale methods are generally differentiated based on four main criteria: governing formulation (energy-based or force-based), coupling boundary conditions (strong or weak), handshake region (present or not), and treatment of the continuum (linear elastic or more complex) [56]. CADD's governing formulation is force-based, meaning that equilibrium is achieved as forces approach zero rather than by minimizing energy. The coupling boundary conditions for CADD are strong, meaning there are atoms in the atomistic region that are constrained to move as though fixed to finite elements in the continuum, and elements in the continuum that are constrained to move as though fixed to atoms in the atomistic region. CADD does not include a handshake region, which means that the transition between the atomistic and continuum regions is abrupt. In fact, the atomistic region in CADD completely ignores the continuum when forces are being computed [56]. The continuum for CADD is a discrete dislocation framework [57], which is more complex than a simple linear elastic continuum in that it accommodates discrete

dislocations. The CADD multiscale method is used in chapter 7 to model Al/a-Si core-shell nanorods.

3.3.1 Continuum-atomistic coupling

Within the CADD algorithm, the continuum region is a finite element mesh of increasing refinement close to the atomistic region, as shown in Figure 3.3(a). The continuum region equilibrates via the conjugate gradient method and can move both continuum and pad nodes. The continuum region has a Dirichlet boundary condition in the form of interface atoms, shown in Figure 3.3(b), that are fixed in the continuum. The atomistic region equilibrates based on whatever atomistic method is being applied and can move both bulk and interface atoms. The atomistic region also has a Dirichlet boundary condition in the form of pad atoms which it considers to be fixed. During simulations with CADD, the atomistic and continuum regions alternate equilibration, with coupling being accomplished by the movement of interface and pad atoms respectively. Note that the region encompassing the pad/interface in CADD is not considered a handshake region because the separation between the continuum and atomistic regions is abrupt rather than gradual. The atomistic region used in chapter 7 is modeled using MD.

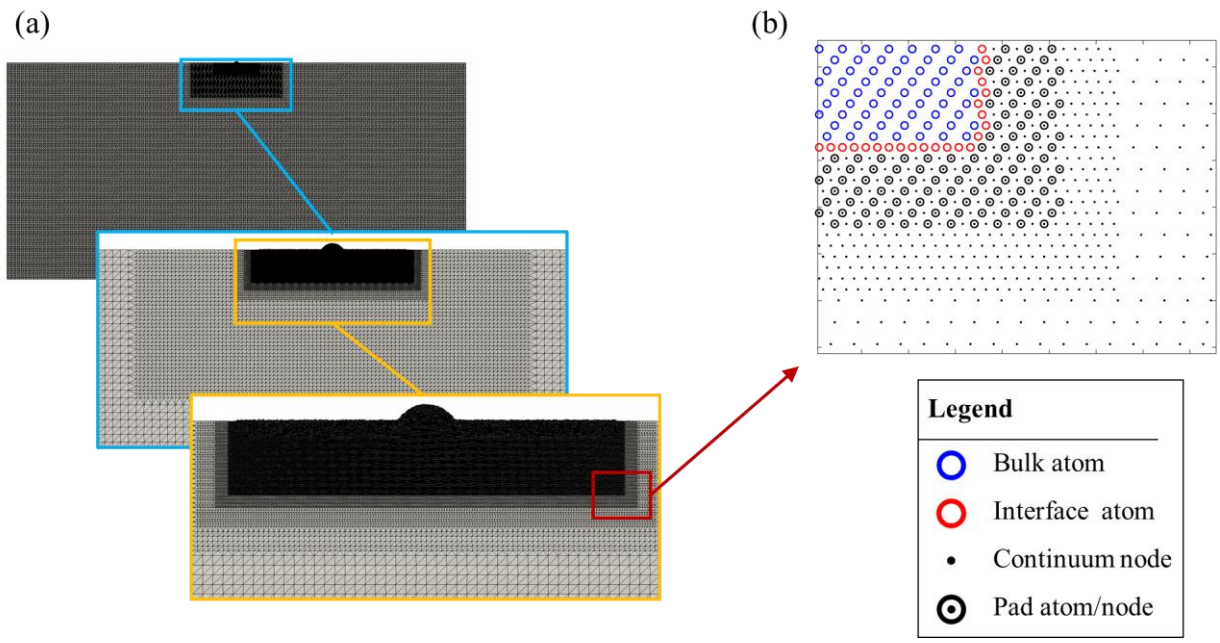

Figure 3.3. (a) FEM mesh for continuum region used in CADD with zoomed in views approaching the atomistic region. (b) Zoomed-in view of the atomistic-continuum interface, showing the different types of atoms/nodes considered in coupling the atomistic and continuum regions in CADD.

3.3.2 Dislocation detection and passing

The most unique aspect of CADD is its method for detecting dislocations in the atomistic region, and then passing those dislocation to the continuum region as discrete dislocations. Shilkrot et al. provide a detailed overview of this process [55]. A detection band of elements is present in the atomistic region a short distance from the atomistic-continuum interface. The detection band is monitored for deformations that indicate the presence of a new dislocation in the atomistic region that is approaching the continuum. This is done by finding the Burger's vector that minimizes the norm of the difference between Lagrangian strain and plastic slip strain. If the minimizing Burger's vector is zero, then no dislocation is present. Otherwise the minimizing Burger's vector is the Burger's vector that is approaching the atomistic-continuum interface. A displacement field is then added to the atomistic region, while at the same time a dislocation core is added to the continuum. In this way the dislocation is eliminated in the atomistic region and passed to the continuum region.

3.3.3 Implementation of CADD for Al/a-Si core-shell nanorods

CADD has been shown to be among the most accurate and efficient multiscale methods of its kind [56], however, it does have limitations. While the atomistic region may contain some 3-D aspects, the nature of CADD's dislocation detection algorithm requires that it only handle problems that are essentially 2-D in nature. This is why the work in chapter 7 models semicylindrical core-shell nanorods to study core-shell variations. One of CADD's other limitations is that it is designed to model only one material in both the continuum region and the atomistic-continuum interface. This work develops a two-material formulation for CADD that extends to both the atomistic and continuum regions. This formulation is covered in section 7.2.

References

[1] S. Plimpton, Fast Parallel Algorithms for Short-Range Molecular-Dynamics, J Comput Phys 117(1) (1995) 1-19.

[2] V. Yamakov, D. Wolf, S.R. Phillpot, A.K. Mukherjee, H. Gleiter, Dislocation processes in the deformation of nanocrystalline aluminium by molecular-dynamics simulation, Nature materials 1(1) (2002) 45.

[3] C.L. Rountree, R.K. Kalia, E. Lidorikis, A. Nakano, L. Van Brutzel, P. Vashishta, Atomistic aspects of crack propagation in brittle materials: Multimillion atom molecular dynamics simulations, Annual Review of Materials Research 32(1) (2002) 377-400.

[4] V.L. Deringer, N. Bernstein, A. Bartok, M.J. Cliffe, R.N. Kerber, L.E. Marbella, C.P. Grey, S.R. Elliott, G. Csányi, Realistic atomistic structure of amorphous silicon from machine-learning-driven molecular dynamics, The journal of physical chemistry letters (2018).

[5] S. Foiles, M. Baskes, M. Daw, Embedded-atom-method functions for the fcc metals Cu, Ag, Au, Ni, Pd, Pt, and their alloys, Phys Rev B 33(12) (1986) 7983.

[6] H. Sheng, M. Kramer, A. Cadien, T. Fujita, M. Chen, Highly optimized embedded-atom-method potentials for fourteen fcc metals, Phys Rev B 83(13) (2011) 134118.

[7] R. LeSar, Introduction to computational materials science: fundamentals to applications, Cambridge University Press2013.

[8] S.M. Kozlov, F. Viñes, A. Görling, Bonding mechanisms of graphene on metal surfaces, The Journal of Physical Chemistry C 116(13) (2012) 7360-7366.

[9] I. Hamada, M. Otani, Comparative van der Waals density-functional study of graphene on metal surfaces, Phys Rev B 82(15) (2010) 153412.

[10] M. Vanin, J.J. Mortensen, A. Kelkkanen, J.M. Garcia-Lastra, K.S. Thygesen, K.W. Jacobsen, Graphene on metals: A van der Waals density functional study, Phys Rev B 81(8) (2010) 081408.

[11] W.-B. Zhang, C. Chen, P.-Y. Tang, First-principles study for stability and binding mechanism of graphene/Ni (111) interface: Role of vdW interaction, The Journal of chemical physics 141(4) (2014) 044708.

[12] W. Zhao, S.M. Kozlov, O. Höfert, K. Gotterbarm, M.P. Lorenz, F. Vines, C. Papp, A. Görling, H.-P. Steinrück, Graphene on Ni (111): coexistence of different surface structures, The Journal of Physical Chemistry Letters 2(7) (2011) 759-764.

[13] M. Baskes, Determination of modified embedded atom method parameters for nickel, Materials Chemistry and Physics 50(2) (1997) 152-158.

[14] B.-J. Lee, M. Baskes, H. Kim, Y.K. Cho, Second nearest-neighbor modified embedded atom method potentials for bcc transition metals, Phys Rev B 64(18) (2001) 184102.

[15] B. Jelinek, S. Groh, M.F. Horstemeyer, J. Houze, S.-G. Kim, G.J. Wagner, A. Moitra, M.I. Baskes, Modified embedded atom method potential for Al, Si, Mg, Cu, and Fe alloys, Phys Rev B 85(24) (2012) 245102.

[16] C.-L. Kuo, P. Clancy, MEAM molecular dynamics study of a gold thin film on a silicon substrate, Surf Sci 551(1-2) (2004) 39-58.

[17] F. Cherne, M. Baskes, R. Schwarz, Atomistic simulations of the phase stability and elastic properties of nickel–zirconium alloys, Journal of non-crystalline solids 317(1-2) (2003) 45-51.

[18] F. Cherne, M. Baskes, P. Deymier, Properties of liquid nickel: A critical comparison of EAM and MEAM calculations, Phys Rev B 65(2) (2001) 024209.

[19] Y. Lü, P. Entel, Impact of medium-range order on the glass transition in liquid Ni-Si alloys, Phys Rev B 84(10) (2011) 104203.

[20] S.J. Stuart, A.B. Tutein, J.A. Harrison, A reactive potential for hydrocarbons with intermolecular interactions, J Chem Phys 112(14) (2000) 6472-6486.

[21] S.W. Chang, A.K. Nair, M.J. Buehler, Geometry and temperature effects of the interfacial thermal conductance in copper- and nickel-graphene nanocomposites, Journal of physics. Condensed matter : an Institute of Physics journal 24(24) (2012) 245301.

[22] S.W. Chang, A.K. Nair, M.J. Buehler, Nanoindentation study of size effects in nickel-graphene nanocomposites, Phil Mag Lett 93(4) (2013) 196-203.

[23] Y. Kim, J. Lee, M.S. Yeom, J.W. Shin, H. Kim, Y. Cui, J.W. Kysar, J. Hone, Y. Jung, S. Jeon, S.M. Han, Strengthening effect of single-atomic-layer graphene in metal-graphene nanolayered composites, Nature communications 4 (2013) 2114.

[24] Y. Yan, J. Lv, S. Liu, Chirality and grain boundary effects on indentation mechanical properties of graphene coated on nickel foil, Nanotechnology 29(16) (2018) 165703.

[25] Y. Yan, S. Zhou, S. Liu, Atomistic simulation on nanomechanical response of indented graphene/nickel system, Computational Materials Science 130 (2017) 16-20.

[26] S. Huang, B. Wang, M. Feng, X. Xu, X. Cao, Y. Wang, Carbon nanoscrolls fabricated from graphene nanoribbons using Ni nanowire templates: A molecular dynamics simulation, Surf Sci 634 (2015) 3-8.

[27] R. Rasuli, K. Mostafavi, J. Davoodi, Molecular dynamics simulation of graphene growth on Ni (100) facet by chemical vapor deposition, Journal of Applied Physics 115(2) (2014) 024311.

[28] X. Liu, F. Wang, H. Wu, W. Wang, Strengthening metal nanolaminates under shock compression through dual effect of strong and weak graphene interface, Applied Physics Letters 104(23) (2014) 231901.

[29] A.P. Thompson, S.J. Plimpton, W. Mattson, General formulation of pressure and stress tensor for arbitrary many-body interaction potentials under periodic boundary conditions, J Chem Phys 131(15) (2009) 154107.

[30] S.J. Plimpton, A.P. Thompson, Computational aspects of many-body potentials, MRS bulletin 37(5) (2012) 513-521.

[31] D. Faken, H. Jónsson, Systematic analysis of local atomic structure combined with 3D computer graphics, Computational Materials Science 2(2) (1994) 279-286.

[32] A. Stukowski, Structure identification methods for atomistic simulations of crystalline materials, Model Simul Mater Sc 20(4) (2012) 045021.

[33] A. Stukowski, Visualization and analysis of atomistic simulation data with OVITO-the Open Visualization Tool, Model Simul Mater Sc 18(1) (2010).

[34] C.L. Kelchner, S. Plimpton, J. Hamilton, Dislocation nucleation and defect structure during surface indentation, Phys Rev B 58(17) (1998) 11085.

[35] P.Y. Huang, C.S. Ruiz-Vargas, A.M. van der Zande, W.S. Whitney, S. Garg, J.S. Alden, C.J. Hustedt, Y. Zhu, J. Park, P.L. McEuen, Imaging grains and grain boundaries in single-layer graphene: An atomic patchwork quilt, arXiv preprint arXiv:1009.4714 (2010).

[36] P.Y. Huang, C.S. Ruiz-Vargas, A.M. van der Zande, W.S. Whitney, M.P. Levendorf, J.W. Kevek, S. Garg, J.S. Alden, C.J. Hustedt, Y. Zhu, Grains and grain boundaries in single-layer graphene atomic patchwork quilts, Nature 469(7330) (2011) 389-392.

[37] C. Rycroft, Voro++: A three-dimensional Voronoi cell library in C++, (2009).

[38] K. Kim, Z. Lee, W. Regan, C. Kisielowski, M. Crommie, A. Zettl, Grain boundary mapping in polycrystalline graphene, ACS nano 5(3) (2011) 2142-2146.

[39] A.C. Van Duin, S. Dasgupta, F. Lorant, W.A. Goddard, ReaxFF: a reactive force field for hydrocarbons, The Journal of Physical Chemistry A 105(41) (2001) 9396-9409.

[40] W. Kohn, L.J. Sham, Self-consistent equations including exchange and correlation effects, Physical review 140(4A) (1965) A1133.

[41] P. Giannozzi, S. Baroni, N. Bonini, M. Calandra, R. Car, C. Cavazzoni, D. Ceresoli, G.L. Chiarotti, M. Cococcioni, I. Dabo, QUANTUM ESPRESSO: a modular and open-source software project for quantum simulations of materials, Journal of physics: Condensed matter 21(39) (2009) 395502.

[42] Z.P. Xu, M.J. Buehler, Interface structure and mechanics between graphene and metal substrates: a first-principles study, J Phys-Condens Mat 22(48) (2010).

[43] C. Fiolhais, F. Nogueira, M.A. Marques, A primer in density functional theory, Springer Science & Business Media2003.

[44] J.P. Perdew, K. Burke, M. Ernzerhof, Generalized gradient approximation made simple, Phys Rev Lett 77(18) (1996) 3865.

[45] W. Koch, M.C. Holthausen, A chemist's guide to density functional theory, John Wiley & Sons2015.

[46] P.E. Blöchl, Projector augmented-wave method, Phys Rev B 50(24) (1994) 17953.

[47] S. Grimme, Semiempirical GGA-type density functional constructed with a long-range dispersion correction, Journal of computational chemistry 27(15) (2006) 1787-1799.

[48] R. Bader, T. Nguyen-Dang, Quantum theory of atoms in molecules–Dalton revisited, Advances in Quantum Chemistry, Elsevier1981, pp. 63-124.

[49] G. Henkelman, A. Arnaldsson, H. Jónsson, A fast and robust algorithm for Bader decomposition of charge density, Computational Materials Science 36(3) (2006) 354-360.

[50] E. Sanville, S.D. Kenny, R. Smith, G. Henkelman, Improved grid-based algorithm for Bader charge allocation, Journal of computational chemistry 28(5) (2007) 899-908.

[51] W. Tang, E. Sanville, G. Henkelman, A grid-based Bader analysis algorithm without lattice bias, Journal of Physics: Condensed Matter 21(8) (2009) 084204.

[52] M. Yu, D.R. Trinkle, Accurate and efficient algorithm for Bader charge integration, The Journal of chemical physics 134(6) (2011) 064111.

[53] L. Shilkrot, R. Miller, W. Curtin, Coupled atomistic and discrete dislocation plasticity, Phys Rev Lett 89(2) (2002) 025501.

[54] R.E. Miller, L. Shilkrot, W.A. Curtin, A coupled atomistics and discrete dislocation plasticity simulation of nanoindentation into single crystal thin films, Acta Materialia 52(2) (2004) 271-284.

[55] L. Shilkrot, R.E. Miller, W.A. Curtin, Multiscale plasticity modeling: coupled atomistics and discrete dislocation mechanics, Journal of the Mechanics and Physics of Solids 52(4) (2004) 755-787.

[56] R.E. Miller, E.B. Tadmor, A unified framework and performance benchmark of fourteen multiscale atomistic/continuum coupling methods, Model Simul Mater Sc 17(5) (2009) 053001.

[57] M. Fivel, Discrete dislocation dynamics: principles and recent applications, in: O. Cazacu (Ed.), Multiscale Modeling of Heterogenous Materials: From Microstructure to Macro-scale Properties, John Wiley & Sons2008, pp. 17-36.

Chapter 4

Paper 1: Dislocation Nucleation in Nickel-Graphene Nanocomposites Under Mode I Loading

Abstract

Graphene has superior mechanical properties, and previous studies have shown that it can be used as a fiber laminate in metal-graphene nanocomposites. Our research outlines the advantages and limitations for different Ni-graphene nanocomposite laminates. Using molecular dynamics, Ni-graphene nanocomposites are studied under mode I loading normal to the graphene laminate plane. The stress intensity factor (K_I) is predicted for the nanocomposite at varying distances between a simulated crack and the graphene sheet(s) in the Ni-matrix. We find that K_I of the Ni-matrix is reduced with the addition of graphene sheet. However, for 1-layer of graphene sheet in Ni-matrix K_I increases with increased spacing between the crack and the graphene sheet. This is due to the change in the crack-generated stress field in the region between the Ni-matrix containing the crack and the graphene sheet, which leads to the lower stress values at which dislocation nucleation occurs compared to single crystal Ni. For multiple layers of graphene sheets in Ni-matrix, we find that failure occurs exclusively by delamination at a lower stress than the 1-layer case. This research concludes that fabricated Ni-graphene nanocomposites can be tuned for optimal fracture strength by the structural arrangement of graphene sheets with in the Ni-matrix.

4.1 Introduction

Ever since it was first synthesized in 2004 [1] graphene has been the subject of much researched for use as a fiber in composite materials. Among the desirable qualities, graphene possesses an exceptional tensile strength of 130 GPa, and a Young's modulus at 1 TPa [2, 3]. To take full advantage of graphene's strengthening effect as a fiber requires that graphene be deposited

in layered sheets rather than dispersed throughout the matrix as graphene flakes [2]. With its 2D geometry graphene sheets provide a maximum surface to volume ratio, giving it the potential for exceptionally high aspect ratios [3].

Within the last several years single and multi-layer graphene sheets have become feasible within a metal matrix through such methods as liquid phase exfoliation [4, 5], thermal exfoliation [6], and chemical vapor deposition [2, 7, 8]. Experiments performed by Kim et al. demonstrated the strengthening effect of 1-layer metal-graphene nanocomposites through nanopillar compression tests [2]. It is found that a single graphene sheet gave nickel 3.3 times greater yield strength than single crystal nickel [2]. This dramatic strength increase is attributable to the difficulty that propagated dislocations have of traveling through graphene sheets; indeed computational models supported the inhibiting effect of graphene on simulated nanopillar compression tests in metal-graphene nanocomposites [2]. The nano-indentation studies by Chang et al. found that increasing the number of layers of graphene sheets led to decreases in the hardness of the metal-graphene nanocomposite, as well as increase in the maximum elastic deformation before dislocation loops began to propagate through the Ni-matrix [9]. Thus it should be possible to tune a metal-graphene nanocomposite's nano-indentation behavior for a desired hardness or maximum elastic deformation.

Dislocations that emerge within a metal-matrix under mode I loading will be affected by the presence of graphene sheet(s). As metal-graphene nanocomposites are entering use in real-world applications [8, 10, 11] it is necessary to understand metal-graphene's possible failure modes. This study focuses on predicting the stress intensity factor under mode I loading (K_I) at the first emergence of dislocations in Ni-graphene using molecular dynamics. This paper aims to predict the degree to which K_I changes in a Ni-graphene nanocomposite based on the number of

graphene sheets present, the crack geometry used, and the distance between the sheets and the crack. With these results we will be able to predict the structure of Ni-graphene layups that will have optimal fracture strength.

4.2 Method

In this study, we use molecular dynamics to simulate Ni-graphene nanocomposites under mode I loading in order to predict the K_I values for these nanocomposites. Ni-graphene samples are comprised of 1 and 3 layer graphene sheets sandwiched between two single crystal Ni blocks, as shown in Figure 4.1. Previous studies [12, 13] have shown that the Ni (111) plane has lattice constants similar to graphene, allowing the graphene to adhere better to the Ni interface, hence this orientation is chosen for the studies carried out here. For each simulation cell the *x*, *y* and *z* axes correspond to the lattice vectors $[11\bar{2}]$, $[111]$ and $[1\bar{1}0]$ respectively. Two different crack geometries chosen for this research: an embedded penny crack and a through-thickness elliptical crack (see Figures 4.1(a-b)). The penny crack is inserted in the block normal to the *y* axis. The elliptical crack is inserted into the block along the *z* axis, with its major axis oriented parallel to the *x* axis. The penny crack can experience dislocations in any of its slip planes [14], while the symmetries of the elliptical crack make dislocations likely to be symmetric along the *z* axis. Both cracks have a half-crack length of 50 Å.

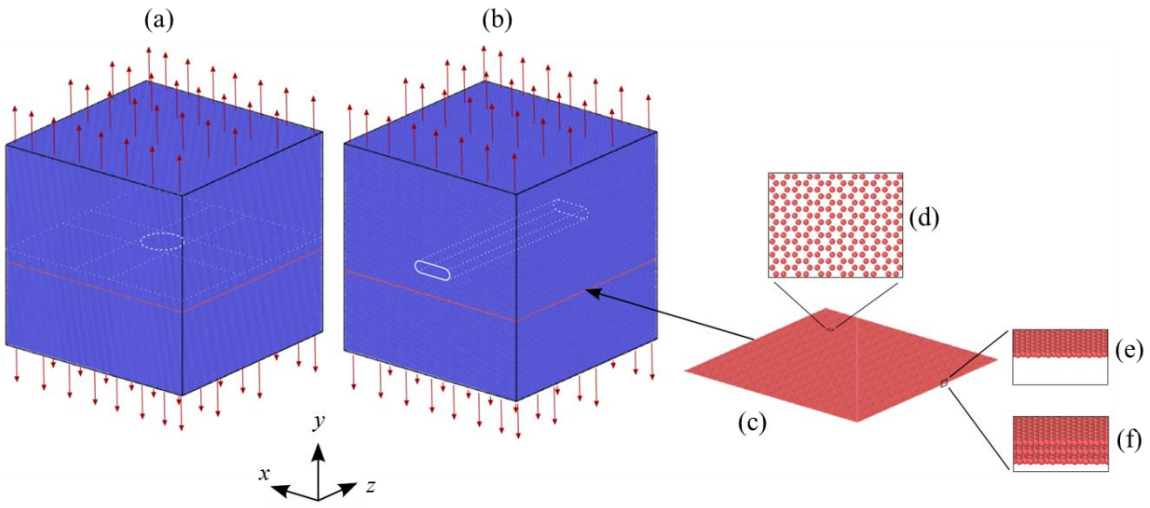

Figure 4.1. Ni-graphene samples for the (a) penny crack and (b) elliptical crack. In both cases the crack face is outlined in white for visualization. The Miller indices corresponding to the *x*, *y*, and *z* axes are $[11\bar{2}]$, $[111]$, and $[1\bar{1}0]$ respectively. Red arrows above and below the samples indicate the direction of loading. (c) Graphene sheet(s) inserted within the Ni matrix. The samples shown here are for graphene at 42.7 Å from the bottom face of the crack. (d) Top-view of the graphene sheet oriented normal to the *y* axis. (e) Perspective side-view of 1-layer graphene sheet. (f) Perspective side-view of 3-layer graphene sheets.

The dimensions of the samples are 500×500×500 Å for both the penny crack and the elliptical crack models. 1-layer and 3-layer sheets of graphene are inserted at a distance δ from the base of the crack, where

$$\delta = m \cdot d \,. \tag{4.1}$$

In eq. (4.1) d is the Ni (111) lattice parameter (6.098 Å), and m is an integer value, making δ a multiple of the Ni (111) lattice parameter. The m values chosen for this simulation are 1, 4, 7, 11 and 15. The graphene sheets are oriented to be parallel to the crack face. The simulation samples used in this research are single crystal Ni, 1-layer of graphene in Ni-matrix, and 3-layers of graphene in Ni-matrix. The penny crack is generated during the simulation by preventing bonding between a top and bottom group of atoms. These groups of atoms are selected to be within cylindrical regions above and below the *y* plane around *y* = 50 Å, with a radius of 50 Å and a height chosen to enclose three layers of Ni atoms in each cylinder. The elliptical crack is generated by

removing atoms in a chosen region. The width of the elliptical crack is chosen to be 100 Å, such that the half crack length is the same as that of the penny crack. The thickness of the elliptical crack is 25 Å.

The embedded-atom method interatomic potential [15] is used for interactions between Ni atoms , while adaptive intermolecular reactive empirical bond order potential [16] is used for interactions between carbon atoms. Interactions between Ni and C atoms are governed by a Lennard-Jones potential, which has been shown to effectively model interactions between Ni and C [12, 17], and with parameters chosen that are ideal for interactions between Ni-C in sheet-sheet interactions [18].

The simulations are carried out using LAMMPS [19] under fully periodic boundary conditions. The samples are minimized using the conjugate gradient method. The initial relaxation uses an NVT ensemble at 1K, followed by isothermal-isobaric conditions (NPT ensemble). After equilibrium is reached, a tensile load is simulated in the *y* direction by applying a uniform strain, with a strain rate of $0.001\ \mathrm{ps}^{-1}$. After each application of strain, the samples are relaxed using both the NVT and NPT ensembles to bring it to an equilibrium state. Values for the stress intensity factor under mode I loading (K_I) are computed using the *y* component of the virial stress computed using LAMMPS [20]. For the penny crack the K_I value is computed by [14]

$$K_I = \frac{2}{\pi}\sigma\sqrt{\pi a}\,, \tag{4.2}$$

where a is the half crack length of 50 Å and σ is the stress corresponding to the first dislocation nucleation from the crack tip for each simulation. For the elliptical crack we use linear elastic fracture mechanics to estimate K_I to be [21]

$$K_I = \sigma\sqrt{W \tan\left(\frac{\pi a}{W}\right)}\ , \tag{4.3}$$

where W is the width of the sample, in this case 500 Å. This approach to compute K_I using molecular dynamics was previously used for BCC Iron [14]. The visualization tool OVITO [22] is used to find the dislocations in the samples, which are identified by coloring atoms based on common neighbor analysis.

4.3 Results

The stress-strain curves for the penny crack geometry are shown in Figure 4.2(a) for single crystal Ni, 1-layer and 3-layer Ni-graphene samples. Different color plots indicate different distances between the bottom crack face and the graphene sheet. Unloading first occurs for single crystal Ni and 1-layer Ni-graphene via dislocation nucleation (~ 6 GPa) and propagation. Multiple slip systems are present for the penny crack, as shown in Figure 4.2(b), with the dislocation loops propagating in the $(\bar{1}11)$, $(1\bar{1}1)$ and $(11\bar{1})$ planes. The graphene sheet in 1-layer Ni-graphene effectively inhibits dislocation loop propagation, as shown in Figure 4.2(c). For the penny crack geometry the plasticity begins between 2.02%-2.14% strain, with the $\delta = 1d$ case being the only exception, occurring instead at 1.52% strain. For the $\delta = 1d$ case the dislocation loop is emitted at stress of 4.5 GPa than in other 1-layer cases due to bending in the graphene sheet, enacted because of the close proximity of the stress concentration at the penny crack-tip to the graphene sheet.

It is found that 3-layer Ni-graphene samples experience delamination before dislocation is nucleated in the Ni matrix, and occurs at lower stress levels (~2 GPa) than in the 1-layer case (5-6 GPa). The stress field in Figure 4.2(d) shows unloading occurring about the graphene-graphene interface, leading to delamination. The strain at which delamination occurs is at 0.81% for the 3-

layer Ni-graphene layups. The similar strain at which delamination occurs is due to cracks in the 3-layer samples not developing enough stress to nucleate a dislocation in Ni matrix. The delamination in the 3-layer case is due to graphene's weak bonding with other graphene sheets compared to its stronger bonding with Ni [9, 14, 23], indicating that tuned Ni-graphene nanocomposites utilizing multiple graphene layers will experience delamination before any crack-tip plasticity.

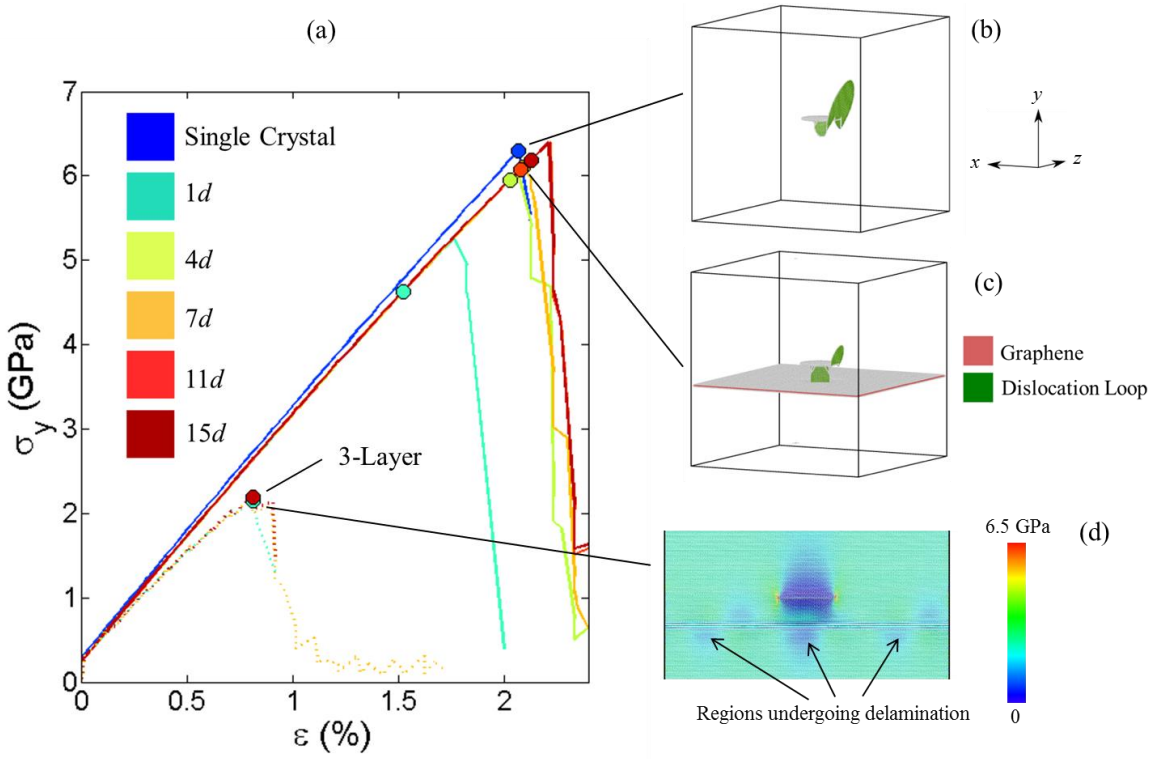

Figure 4.2. (a) Stress vs strain curves for the penny crack simulation, with points (circle dots) indicating the nucleation of the first dislocation in single crystal Ni and 1-layer of graphene in Ni matrix cases and the maximum stress before delamination for 3-layer Ni-graphene case. (b) Dislocation nucleation from the single crystal Ni penny crack, with FCC atoms removed and dislocation loops colored green for visualization. The *x, y* and *z* axes correspond to the directions $[11\bar{2}]$, [111] and $[1\bar{1}0]$ respectively. (c) One of the dislocation loops nucleated from the penny crack is inhibited by the graphene sheet for $\delta = 7d$ case, with graphene colored in pink. (d) The stress distribution in *x-y* plane of 3-layer Ni-graphene sample for $\delta = 7d$, with a slice taken at z = 250 Å. The low stress regions developing at the graphene sheet demonstrate the beginning of the delamination behavior inherent in 3-layer Ni-graphene. Dislocation nucleation is not observed for 3-layer Ni-graphene nanocomposite in any crack geometry.

The stress-strain curves for the elliptical crack geometry are shown in Figure 4.3(a) single crystal Ni, 1-layer, and 3-layer Ni-graphene samples. The active slip system for the elliptical crack geometry during unloading is in the $(11\bar{1})$ plane. The Burgers vector for the dislocation propagating from the single crystal Ni elliptical crack is in the $[112]$ direction as shown in Figure 4.3(b). When graphene is present, dislocation loops are emitted from the elliptical crack tip with the same Burgers vector as in the single crystal Ni case, shown in Figure 4.3(c). For the elliptical crack geometry cases plastic behavior begins between 1.62%-1.76% strain. Unlike the penny crack, the $\delta = 1d$ case for the elliptical crack does not emit dislocations early because of the greater distance between the elliptical crack tip and the graphene sheet. The difference in strain-to-plasticity for the penny and elliptical cracks is based on their geometry. For both the penny and elliptical crack geometries whenever a dislocation reaches a graphene sheet, it is blocked, in agreement with previous studies [2, 9], but continued tensile loading normal to the graphene will effectively prevent further plastic deformation in Ni and leads to delamination at Ni-graphene interface (see Fig.2a & 3a). The 3-layer Ni-graphene samples for elliptical crack case delaminates between graphene sheets at a stress of 2 GPa similar to the penny crack case.

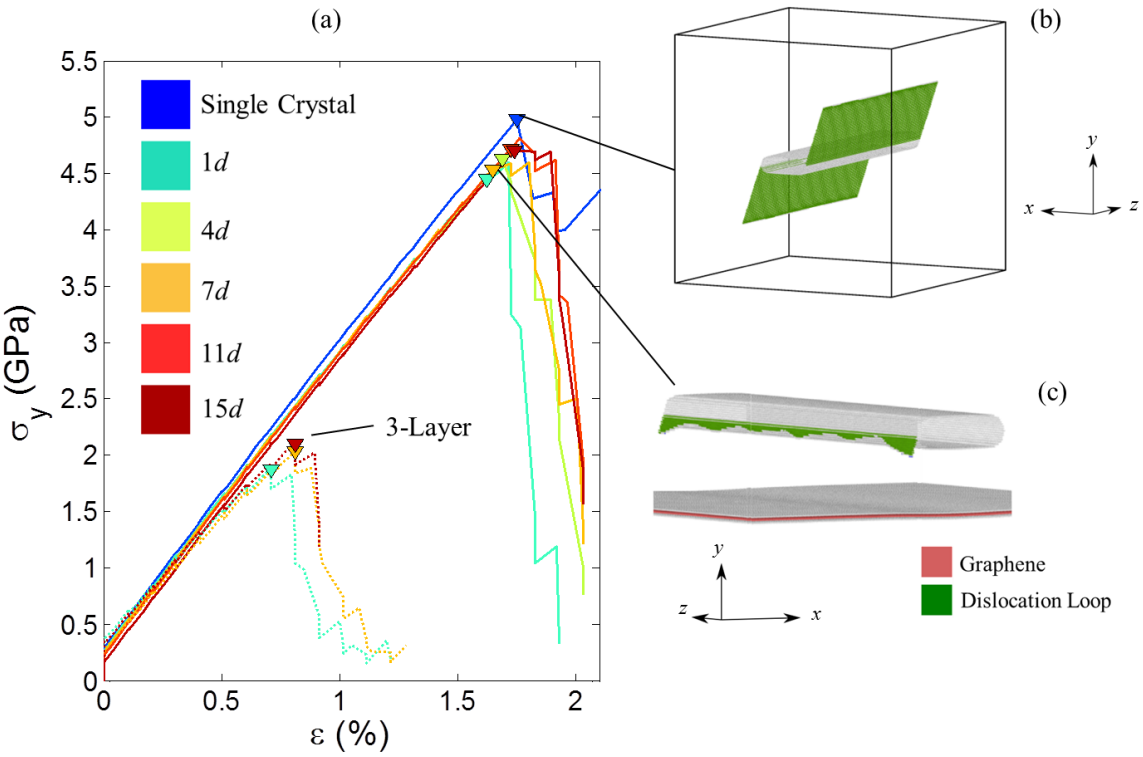

Figure 4.3. (a) Stress vs strain curves for the elliptical crack layups, with points indicating the nucleation of the first dislocation (single crystal Ni and 1-layer Ni-graphene) or maximum stress before delamination for 3-layer Ni-graphene case. (b) Dislocations nucleated from the single crystal Ni elliptical crack, with FCC atoms removed and dislocations are colored in green for visualization. The *x*, *y* and *z* axes correspond to the directions $[11\bar{2}]$, $[111]$ and $[1\bar{1}0]$ respectively. (c) Initial dislocation nucleation from the elliptical crack in for 1-layer Ni-graphene case with distance of graphene at $\delta = 7d$ from the crack tip.

Stress intensity factors (K_I) are calculated using eq. (4.2) and (4.3) for both penny and elliptical crack geometries and are listed in Table 4.1. The higher K_I values for the elliptical crack samples are due to the difference in crack geometry. Table 4.1 also includes the percent decrease in K_I for single crystal Ni when graphene is added. The maximum drop (26.6%) in K_I is found for penny crack case when $\delta = 1d$. It is found that for both crack geometries K_I approaches the level of single crystal Ni as δ increases, with the lowest percent decrease being 1.7% (for the $\delta = 15d$ case of the penny crack geometry). This is demonstrated in Figure 4.4(a) (with Figure 4.4(b) illustrating the distance $\delta = m \cdot d$ for clarity). The K_I values decrease with closer proximity because the stress field generated at the crack tip is more confined when the graphene sheet is in

close proximity to the crack plane (i.e. for smaller values of m), leading to a dislocation nucleation at lower stress intensity compared to the single crystal Ni case.

Table 4.1. Results of the simulations for a given crack geometry and Ni-graphene layup. The K_I values and strain are each found at the nucleation of the first dislocation. The percent decrease in K_I is the percent difference between the Ni-graphene sample and the single crystal Ni sample of the same crack geometry.

Crack Geometry	Layup	m	K_I $\left(\text{MPa}\sqrt{\text{m}}\right)$	% Decrease in K_I	Strain (%)
Penny	Single Crystal	NA	0.503	NA	2.07%
	1-Layer	1	0.369	26.6%	1.52%
		4	0.474	5.6%	2.03%
		7	0.487	3.2%	2.09%
		11	0.485	3.6%	2.08%
		15	0.494	1.7%	2.13%
Elliptical	Single Crystal	NA	0.635	NA	1.75%
	1-Layer	1	0.567	10.6%	1.62%
		4	0.590	7.1%	1.69%
		7	0.578	8.9%	1.65%
		11	0.601	5.3%	1.72%
		15	0.600	5.6%	1.74%

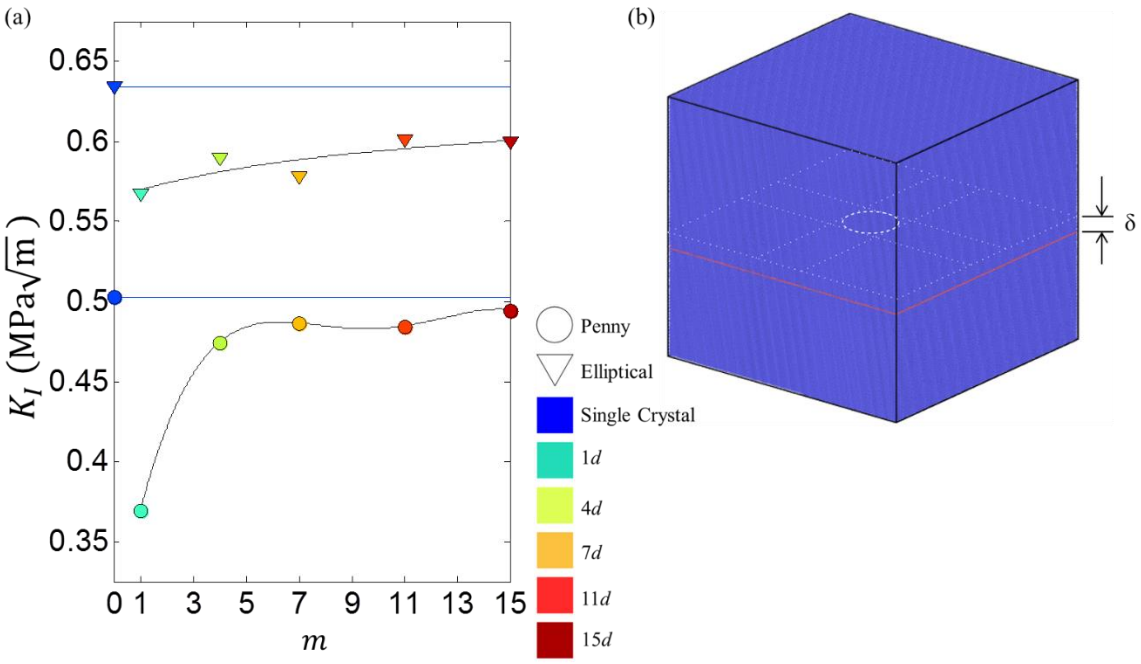

Figure 4.4. (a) Stress intensity K_I vs distance between crack and 1-layer graphene for penny and elliptical cracks. Single crystal Ni K_I values are also shown where $m = 0$. (b) Representation of distance δ between the crack and graphene sheet, where $\delta = m \cdot d$.

In order to test the effect when all dislocation loops emitted by the crack are inhibited by graphene sheets, and to further confine the stress field generated at the crack tip, we conduct another study with a single sheet of graphene added both above and below the crack plane. For this simulation the first sheet is inserted at a distance $\delta = 7d$ below the crack plane, as in the previous simulations, and a second graphene sheet is inserted a distance $\delta = 7d$ above the crack plane. This layup is tested for both the penny and elliptical crack geometries. It is found that the dislocations emitted for both crack geometries are completely inhibited by the top and bottom graphene sheets. The K_I values predicted for the penny crack and the elliptical crack are 0.476 MPa$\sqrt{\text{m}}$ and 0.566 MPa$\sqrt{\text{m}}$ respectively. These values are slightly smaller than the K_I values in the 1 layer case (bottom only) $\delta = 7d$ layup (found in Table 4.1), implying that the further confinement of the stress field by two graphene sheets leads to a decrease in the K_I value. Hence,

the orientation of graphene sheet(s) (parallel or perpendicular to crack plane) in Ni matrix could play a significant role in the fracture properties of Ni-graphene nanocomposites.

4.4 Conclusions

In this research, we found that the stress intensity factor for a Ni-graphene nanocomposite increases as the distance between the crack and the graphene sheet increases. This effect is caused by the graphene's confinement of the stress intensity generated at the crack tip in the Ni-matrix. This allows for Ni-graphene nanocomposites to be tuned in order to confine stress intensity in the Ni-matrix for desired fracture strength. In addition, graphene prevents the transmission of dislocations between different regions of the Ni-matrix. These mechanical properties make Ni-graphene an attractive candidate for future nanocomposite design. We also found that for multilayer graphene nanocomposites are prone to delamination at the graphene-graphene interface. The strengthening effect of multilayer graphene is still significant [24], so knowing these limitations with multilayer-graphene nanocomposites would require more graphene sheets aligned parallel to tensile loading than normal to the graphene sheets. The stress field confinement by graphene sheet(s) discussed here could be useful to tune fracture properties of bioinspired nanocomposites that mimic bone and nacre like structures.

Acknowledgements

AKN and SM acknowledge support from Arkansas Economic Development Commission (#16-EPS3-0001). This work was supported in part by the National Science Foundation under the grants ARI#0963249, MRI#0959124 and EPS#0918970, and a grant from Arkansas Science and Technology Authority, managed by Arkansas High Performance Computing Center.

References

[1] K.S. Novoselov, A.K. Geim, S.V. Morozov, D. Jiang, Y. Zhang, S.V. Dubonos, I.V. Grigorieva, A.A. Firsov, Electric field effect in atomically thin carbon films, Science 306(5696) (2004) 666-9.

[2] Y. Kim, J. Lee, M.S. Yeom, J.W. Shin, H. Kim, Y. Cui, J.W. Kysar, J. Hone, Y. Jung, S. Jeon, S.M. Han, Strengthening effect of single-atomic-layer graphene in metal-graphene nanolayered composites, Nature communications 4 (2013) 2114.

[3] I.A. Ovid'ko, Metal-Graphene Nanocomposites with Enhanced Mechanical Properties: A Review, Rev Adv Mater Sci 38(2) (2014) 190-200.

[4] Y. Hernandez, High-yield production of graphene by liquid-phase exfoliation of graphite, Nature Nanotechnol. 3 (2008) 563-568.

[5] P. Blake, Graphene-based liquid crystal device, Nano Lett. 8 (2008) 1704-1708.

[6] H.C. Schniepp, Functionalized single graphene sheets derived from splitting graphite oxide, J. Phys. Chem. B 110 (2006) 8535-8539.

[7] X. Li, W. Cai, J. An, S. Kim, J. Nah, D. Yang, R. Piner, A. Velamakanni, I. Jung, E. Tutuc, S.K. Banerjee, L. Colombo, R.S. Ruoff, Large-area synthesis of high-quality and uniform graphene films on copper foils, Science 324(5932) (2009) 1312-4.

[8] S. Bae, Roll-to-roll production of 30-inch graphene films for transparent electrodes, Nature Nanotechnol. 5 (2010) 574-578.

[9] S.W. Chang, A.K. Nair, M.J. Buehler, Nanoindentation study of size effects in nickel-graphene nanocomposites, Phil Mag Lett 93(4) (2013) 196-203.

[10] A.K. Geim, Graphene: status and prospects, Science 324 (2009) 1530-1534.

[11] A.K. Geim, K.S. Novoselov, The rise of graphene, Nat Mater 6(3) (2007) 183-91.

[12] Z.P. Xu, M.J. Buehler, Interface structure and mechanics between graphene and metal substrates: a first-principles study, J Phys-Condens Mat 22(48) (2010).

[13] M. Fuentes-Cabrera, M.I. Baskes, A.V. Melechko, M.L. Simpson, Bridge structure for the graphene/Ni(111) system: A first principles study, Phys Rev B 77(3) (2008).

[14] C.H. Ersland, I.R. Vatne, C. Thaulow, Atomistic modeling of penny-shaped and through-thickness cracks in bcc iron, Model Simul Mater Sc 20(7) (2012).

[15] M.S. Daw, M.I. Baskes, Semiempirical, Quantum-Mechanical Calculation of Hydrogen Embrittlement in Metals, Phys Rev Lett 50(17) (1983) 1285-1288.

[16] S.J. Stuart, A.B. Tutein, J.A. Harrison, A reactive potential for hydrocarbons with intermolecular interactions, J Chem Phys 112(14) (2000) 6472-6486.

[17] L. Bardotti, P. Jensen, A. Hoareau, M. Treilleux, B. Cabaud, Experimental observation of fast diffusion of large antimony clusters on graphite surfaces, Phys Rev Lett 74(23) (1995) 4694-4697.

[18] S.P. Huang, D.S. Mainardi, P.B. Balbuena, Structure and dynamics of graphite-supported bimetallic nanoclusters, Surf Sci 545(3) (2003) 163-179.

[19] S. Plimpton, Fast Parallel Algorithms for Short-Range Molecular-Dynamics, J Comput Phys 117(1) (1995) 1-19.

[20] A.P. Thompson, S.J. Plimpton, W. Mattson, General formulation of pressure and stress tensor for arbitrary many-body interaction potentials under periodic boundary conditions, J Chem Phys 131(15) (2009) 154107.

[21] Z. Qin, M.J. Buehler, Carbon dioxide enhances fragility of ice crystals, J Phys D Appl Phys 45(44) (2012).

[22] A. Stukowski, Visualization and analysis of atomistic simulation data with OVITO-the Open Visualization Tool, Model Simul Mater Sc 18(1) (2010).

[23] S.W. Chang, A.K. Nair, M.J. Buehler, Geometry and temperature effects of the interfacial thermal conductance in copper- and nickel-graphene nanocomposites, Journal of physics. Condensed matter : an Institute of Physics journal 24(24) (2012) 245301.

[24] R.J. Young, I.A. Kinloch, L. Gong, K.S. Novoselov, The mechanics of graphene nanocomposites: a review, Compos. Sci. Technol. 72 (2012) 1459-1476.

Chapter 5

Paper 2: Failure mechanisms in pre-cracked Ni-graphene nanocomposites

Abstract

Graphene is a 2-D material with superior mechanical properties and is highly desirable as a filler in nanocomposite materials. However, the mechanical properties of the resulting nanocomposite are anisotropic, with strengthening or weakening depending on the loading direction. The presence of graphene also introduces new failure mechanisms to the matrix it is embedded within. In addition, the structure of graphene, pristine or polycrystalline, can affect its interfacial properties in the nanocomposite. We use molecular dynamics to predict the failure mechanisms of Ni-graphene nanocomposites for different loading directions with a crack present in the Ni matrix. We observe a variety of failure mechanisms including dislocation nucleation, graphene bond breaking, and delamination. We also compare the yield stress and strain of nanocomposites with either pristine or polycrystalline graphene. We find that graphene of either kind can improve the yield stress of Ni by 27-76% when loaded parallel to the graphene sheet. We also find that, compared to pristine graphene, polycrystalline graphene can improve the yield stress of a Ni-graphene nanocomposite by up to 27%. This is explained by the higher interfacial shear stress of polycrystalline graphene on Ni's (111) surface compared to pristine graphene. This is in part related to the wrinkling of graphene sheets, which differs between polycrystalline and pristine sheets. Our research indicates that metal-graphene nanocomposites benefit from graphene's polycrystalline structure when superior mechanical properties are desired.

5.1 Introduction

For many of its potential applications graphene of a near-pristine structure is desirable. However, producing pristine monolayered graphene sheets is an ongoing challenge for manufacturers of graphene. Generally, graphene sheets have a polycrystalline structure. Studies have shown that the grain boundaries present in polycrystalline graphene lead to lower strength compared to pristine graphene [1-5]. However, depending on the grain structure, graphene's strength may be only slightly diminished [6-8], or can even show some improvement [9].

As a 2-D material, graphene has an incredibly high aspect ratio and specific surface area, which makes it an attractive candidate for use in nanocomposite materials [10]. Research has shown that the inclusion of graphene provides metal matrixes with greatly enhanced mechanical properties [11-16]. Part of the enhancement that metal-graphene nanocomposites show is greater resistance to some failure mechanisms. Kim et al. showed both experimentally and computationally that dislocations are inhibited by graphene sheets, preventing plastic deformation from propagating between regions within a metal matrix separated by graphene [12]. This has been shown to occur under both indentation [17], tension [18], and compression [19].

Not all failure mechanisms of metal-graphene nanocomposites show improvements over pure metal. The presence of graphene makes delamination a prominent failure mode at the metal-graphene interface [20-22]. The propensity for delamination depends in part on stress concentrations present in the matrix due to defects, like cracks, which ultimately produce dislocations. Dislocations in the metal matrix pile up at the graphene sheet, where stress further concentrates until delamination is initiated [18].

Experiments have shown that graphene's ability to improve the mechanical properties of a nanocomposite is dependent on its ability to transfer load between different regions of the matrix in which it is present [23-25]. Computational work by Sharma et al. has shown that graphene is more effective at load transfer within a matrix than carbon nanotubes, particularly at higher temperatures [26]. The efficiency of graphene's load transfer is dependent on the interfacial shear stress between graphene and the surrounding matrix [27-29]. Wrinkles present in graphene may affect interfacial shear stress by changing the degree of contact between graphene and the matrix. Previous research shows that graphene sheets tend to wrinkle [30-32], and that this can dramatically affect their mechanical properties [33-36]. Yang et al. studied fracture in nickel-graphene nanocomposites using MD simulations and found that slip at the nickel/graphene interface and wrinkling in the graphene sheet changed the stress distribution along the graphene layers [16]. This led to a release of stress in metal layers near the graphene sheet. We note that their study considered only pristine graphene, hence different mechanisms that would arise due to polycrystalline graphene remain unexplored.

The presence of graphene will affect the yield behavior of metal matrixes possessing preexisting cracks, but the way that loading and crack orientation affects failure mechanisms of such nanocomposites has not yet been considered. In addition, the effect that the structure of graphene (pristine or polycrystalline) has on the strength of nanocomposites needs further study. This research uses molecular dynamics to predict the yield stress and strain for nanocomposite samples consisting of a pre-cracked Ni matrix with either pristine or polycrystalline graphene sandwiched within it. We consider the failure mechanisms of the nanocomposites under tension with different loading directions and crack orientations. Our previous study [18] used a single crack orientation and loading direction and only pristine graphene.

The novelty of this research is in comparing the mechanical properties of polycrystalline graphene to pristine graphene in the context of metal matrix nanocomposite. This includes comparing the interfacial shear stress between Ni and either pristine or polycrystalline graphene and how the stress field from the crack tip interacts with the graphene. Moreover, we compare the wrinkling of pristine and polycrystalline graphene sandwiched in a Ni matrix; we also analyze the effect this has on the stress distribution of contiguous Ni layers. The results of this study will be important in the context of nanocomposites because polycrystalline graphene is what is generally used in experimental graphene-based nanocomposites. Computational studies of nanocomposites that model only pristine graphene may neglect important effects inherent in graphene's polycrystalline structure and its unique characteristics within matrixes.

5.2 Methods

In this study, we use molecular dynamics (MD) method to predict the yield stress of a Ni-graphene nanocomposite with an embedded elliptical crack depending on its loading direction, crack orientation, and graphene structure. Yield occurs by either dislocation nucleation within the Ni matrix or delamination of the graphene sheet from the Ni matrix. We compare these results to Ni samples with no graphene included.

5.2.1 Ni matrix and description of different cases

We choose Ni as the metal matrix in the nanocomposite because the lattice constant for graphene is similar to that of Ni's (111) face, giving graphene a strong adhesion to the Ni surface [37-39]. For each simulation cell the *x, y* and *z* axes correspond to the lattice vectors $[11\bar{2}]$, $[111]$, and $[1\bar{1}0]$ respectively. We employ periodic boundary conditions at each boundary. A typical simulation cell for this study is shown in Figure 5.1(a). The Ni matrix has an elliptical crack

introduced by selective atom removal, with the crack oriented such that its major axis is parallel or perpendicular to the graphene sheet, as shown in Table 5.1. In all simulations, we deposit graphene on the Ni's (111) plane, which is the *x*-*z* plane. Each simulation cell has either zero, one or two sheets present, as shown in Figure 5.1(b). The dimensions of the simulation cell are approximately 500 × 500 × 20 Å. The cracks present in the metal matrix are through-thickness elliptical cracks, with a crack length of 100 Å and an initial opening of 25 Å.

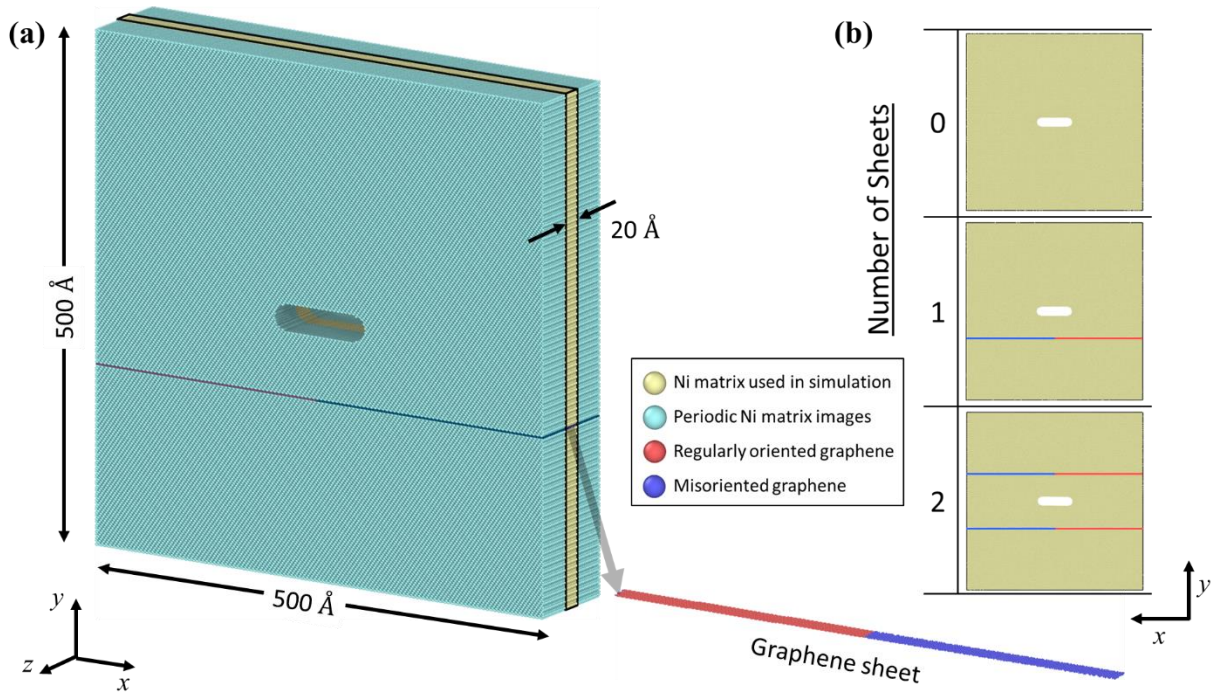

Figure 5.1. (a) Example of typical Ni-graphene sample with periodic images of the sample shown. The graphene sheet shown is polycrystalline with a single grain boundary in the unit cell. The grains are colored differently. Yellow atoms are Ni used in simulation, turquoise atoms are periodic images of the Ni matrix, red atoms are regularly oriented graphene, blue atoms are misoriented graphene. The elliptical crack in the Ni matrix has a crack length of 100 Å. (b) Layout of graphene present in simulation samples, with zero, one and two sheets present. Polycrystalline sheets with the crack-oriented parallel to the graphene sheet are shown here.

Loading during the simulation can occur either in the *x* direction, parallel to the graphene sheet, or in the *y* direction, normal to the graphene sheet. In both cases the elliptical crack in the Ni matrix can be oriented such that its semi-major axis is either parallel with or normal to the

graphene sheet. This gives four distinct cases of loading direction and crack orientation that are organized and shown in Table 5.1. For case 1 the loading direction and crack orientation are in the *x* direction, parallel to the graphene sheet. For case 2 the loading direction is the *x* direction, parallel to the graphene sheet, while the crack is oriented in the *y* direction, normal to the graphene sheet. For case 3 the loading direction is in the *y* direction, normal to the graphene sheet, while the crack is oriented in the *x* direction, parallel to the graphene sheet. For case 4 both the loading direction and crack orientation are in the *y* direction, normal to the graphene sheet. Each of these cases is considered in this simulation because the relationship between crack and loading direction relative to the graphene sheet plays a major role in the potential failure behavior of the Ni-graphene nanocomposite. When the loading direction and crack orientation are parallel to one another there is no strongly defined crack tip, which occurs for cases 1 and 4. When the loading direction and crack orientation are orthogonal to one another the crack forms a defined crack tip at which stress concentrates, which occurs for cases 2 and 3.

Table 5.1. Key to different Ni-graphene loading directions and crack orientations used in the simulations.

	Case 1	Case 2	Case 3	Case 4
Loading direction relative to graphene sheet	∥	∥	⊥	⊥
Crack orientation relative to graphene sheet	∥	⊥	∥	⊥
Visualization	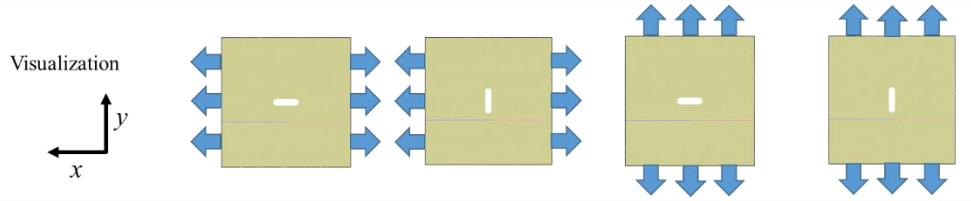			

5.2.2 Graphene layup in pristine and polycrystalline model for single grain boundary

Samples with graphene present are generated with either one or two sheets. A single pristine or polycrystalline graphene sheet is sandwiched within a Ni matrix by first removing a

single close-packed layer of Ni atoms around 75 Å below the center of the elliptical crack. For samples with two sheets present, a second sheet is inserted 75 Å above the center of the elliptical crack. This distance allows stress concentration build-up at the crack tip to affect the graphene sheet, but won't lead to dislocations before general failure begins [18]. A pristine sheet is a graphene sheet where all the graphene has one orientation that is continuous at the periodic boundary. A polycrystalline sheet has a regularly oriented graphene region (graphene which is oriented in the same direction as pristine graphene), and a misoriented region. These two regions meet at one grain boundary centered beneath the elliptical crack in the Ni matrix, and one grain boundary located at the periodic interface.

Polycrystalline graphene sheets are created for the model by first generating an oversized graphene sheet for each desired grain. Grains are then cut from the oversized sheet in the shape desired for the final grain structure. Regularly oriented grains have a symmetric periodic image, allowing it to act as a single unbroken grain. Misoriented grains have a nonsymmetric periodic image, which means that an additional grain boundary is formed at the simulation cell's periodic boundary. Thus, each regular grain only has two boundaries, each parallel to the *z* axis, while each misoriented grain has four different boundaries, two parallel to the *z* axis and two parallel to the *x* axis. Since no loading is done parallel to the *z* axis, the stress concentration generated at the misoriented grain's periodic boundary is minimal compared to the stress concentration at the regular-grain/misoriented-grain interface. A regularly oriented grain is a grain with an orientation of 0°. Angles for the misoriented grains are chosen based on experimental observation of polycrystalline graphene sheet orientations [40] which found that grains with misorientation angles closer to 0° and 30° were more common than middle range angles, though middle range angles were still present. Additionally, polycrystalline graphene sheets with high angle grain

misorientations have been shown experimentally to have higher strength than graphene sheets with lower angle grain misorientations [7]. We use misoriented angles of 15° and 30° to encompass both less common and more common misoriented boundaries, as well as sheets that have lower and higher strength. An example of the regular-grain/misoriented-grain boundary is shown in Figure 5.2. Note that the defects we see at our polycrystalline grain boundary are similar to the Stone-Wales defects that have been observed at polycrystalline graphene grain boundaries both computationally [41] and experimentally [40].

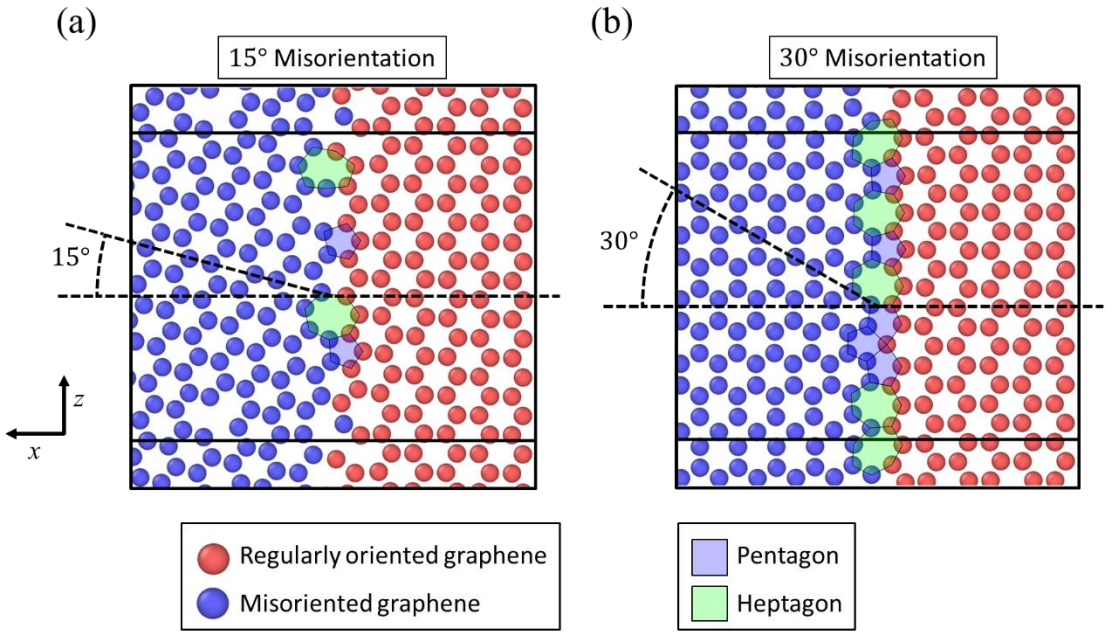

Figure 5.2. Grain boundary between regularly oriented graphene sheets and misoriented graphene sheets, with periodic images shown. Also shown are pentagon and heptagon defects present at the grain boundaries. (a) Polycrystalline graphene sheet with misoriented grain at 15° with the regularly oriented grain. (b) Polycrystalline graphene sheet with misoriented grain at 30° with the regularly oriented grain. Note that regularly oriented graphene sheets are symmetric at the periodic boundary while misoriented graphene has a nonsymmetric boundary, essentially forming a separate grain boundary with itself.

The rectangular straight-edged grain boundaries in our polycrystalline graphene structure is designed to study the effect that a single grain boundary near an elliptical crack has on the yield stress of a Ni-graphene nanocomposite. The behavior we observe with this polycrystalline

graphene grain structure can then be further investigated for more complex polycrystalline geometries.

5.2.3 Ni-graphene model for polycrystalline graphene structure with multiple grain boundaries

To further study the effect of multiple grain boundaries, we also develop a Ni-graphene sample with substantially increased thickness in the *z* direction such that the nanocomposite model is a cube with 500 Å on each side, as shown in Figure 5.3(a). This allows for the inclusion of a square graphene sheet, with multiple grain boundaries and more realistic non-rectangular grain shapes within the nanocomposite. The graphene we use in this study is either pristine or polycrystalline, with a fixed size of 500 × 500 Å. Polycrystalline graphene sheets have either 4 grains, 10 grains, or 25 grains, which gives them an average grain size of approximately 250 Å, 158 Å, or 100 Å respectively. Each grain is given a random orientation, with grain shape chosen randomly by Voronoi tessellation using the open source software library Voro++ [42]. An example of one of these polycrystalline graphene sheets is shown in Figure 5.3(b).

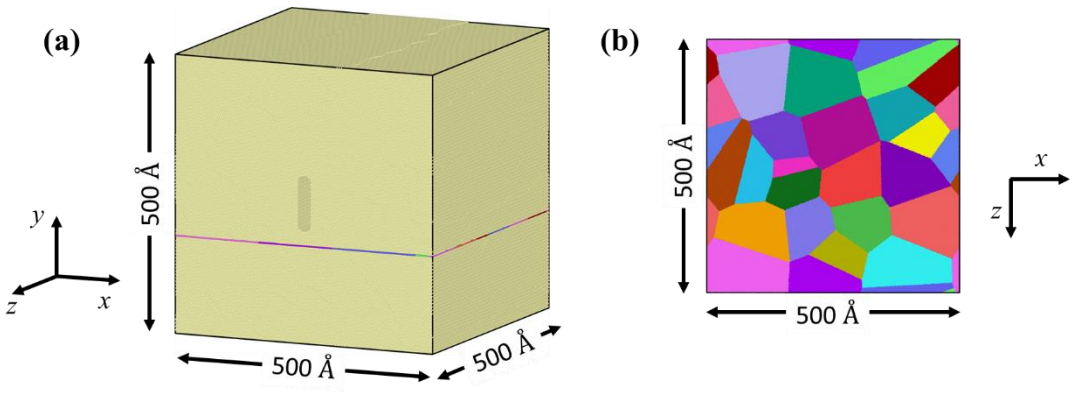

Figure 5.3. (a) Larger case sample with multiple grains to further compare pristine graphene sheets to polycrystalline graphene sheets. (b) Polycrystalline graphene sheet with 100 Å grain size. Each grain has graphene at a different random orientation.

5.2.4 Simulation specifics

The interatomic potential setup we use for Ni-graphene is obtained from the work of Chang et al., who studied the size effects of Ni-graphene nanocomposites under indentation [17]. Chang et al.'s work was in qualitative agreement with the experimental and computational work of Mordehai et al. [43]. In this study we use an embedded-atom method interatomic potential (EAM) [44, 45] for Ni-Ni interactions. For carbon-carbon interactions, an adaptive intermolecular reactive empirical bond order potential (AIREBO) [46] is used. The AIREBO potential has been successfully used to study the mechanical properties of polycrystalline graphene sheets in previous studies [5, 41]. To validate our use of this potential we test a pristine graphene sheet independently, using all the simulation parameters discussed below and assuming a graphene thickness of 3.4 Å [47]. We find that graphene has a Young's modulus of ~0.88 TPa. This is in good agreement with experimental measurements by Lee et al. who found a Young's modulus of graphene of 1.0 TPa [48]. We are also in very close agreement with Pei et al., who also used the AIREBO potential and found the Young's modulus of ~0.86 TPa for graphene [47].

A Lennard-Jones potential is used to govern Ni-carbon interactions, with a well depth and size cross of 0.023049 eV and 2.852 Å respectively, obtained from Huang et al. [49]. Lennard-Jones potentials are often used in Ni-carbon interactions when modeling Ni-graphene [12, 17, 50-55]; this is because of the van der Waals interactions present between Ni and graphene [56-60]. We note that Ni-graphene interactions can be sensitive to the type of interatomic potential used [61-64]. However, we believe the use of a Lennard-Jones potential is still reasonable as our focus is on the effects of graphene's geometric structure in strengthening the Ni matrix, and we are assuming that both pristine and polycrystalline graphene are charge neutral.

MD simulations are performed using the Large-scale Atomic/Molecular Massively Parallel Simulator (LAMMPS) [65]. The simulation initially undergoes energy minimization by the conjugate gradient method followed by relaxation under isothermal-isobaric conditions (NPT ensemble), and a temperature of 300 K. The simulation consists of three steps. First, a tensile load is simulated by applying a uniform strain in the *x* direction for cases 1 and 2, and in the *y* direction for cases 3 and 4. The strain rate is 0.001 ps^{-1}, during which the NPT ensemble is active. This continues for 1 ps, at which point 0.1% strain is reached in the loading direction. Second, we perform an energy minimization to allow atoms to reach a more stable state. Third, an NPT ensemble is applied without additional strain for 2.5 ps to bring the system into an equilibrium state. This process is repeated throughout the simulation, with values of stress for the system recorded as well as the accompanying strain. Stress fields for all cases are calculated using the virial stress definition by Thompson et al. [66].

Multiple simulations are performed for each sample. Each simulation is given a different number seed to generate velocities for atoms in the simulation. The yield stress and strain values for each sample reported in the results is the average yield stress and strain of the simulations for that sample. Error bars in plots are generated using the first standard deviation of the relevant values for the simulations.

We use the open source software OVITO [67] to visualize samples and locate dislocations when they appear. We examine each sample to find the strain at which the first yield event occurs. Yield events are either dislocation nucleation in the Ni matrix, or delamination at the Ni-graphene interface. Only yield stresses and strains are reported here, but stress vs. strain curves can be viewed in Appendix A.

5.3 Results and Discussion

5.3.1 Analysis of Ni-graphene samples with single grain boundary

We perform tensile tests on cases 1-4 as listed in Table 5.1 that correspond to samples shown in Figures 5.1 and 5.2. The stress at first yield for each of the tested samples are shown in Figure 5.4. Each of the different cases (1-4) experience failure with some distinct characteristics that are discussed separately in sections 5.3.1.1 – 5.3.1.4. In every case with graphene present, and where dislocations are nucleated, dislocations are prevented from passing through the graphene sheet into different regions of the Ni matrix, as seen experimentally [12]. In cases where yield occurs by dislocation nucleation, the dislocations are Shockley partial dislocations. Specific yield stress values will be discussed on a case by case basis.

In general, samples with multiple graphene sheets have dislocations that nucleate at slightly higher stress than samples with only one graphene sheet. We observe that cases with polycrystalline graphene in the Ni matrix consistently have dislocations nucleate at higher stress than their pristine counterparts, even though previous studies have found that pristine graphene has superior mechanical properties compared to polycrystalline graphene [5, 68]. We note that those models were investigating graphene on its own, not as part of a nanocomposite structure. The improved mechanical properties we see have more to do with the interaction of the specific graphene structure and the Ni matrix rather than the strength of the graphene sheet alone.

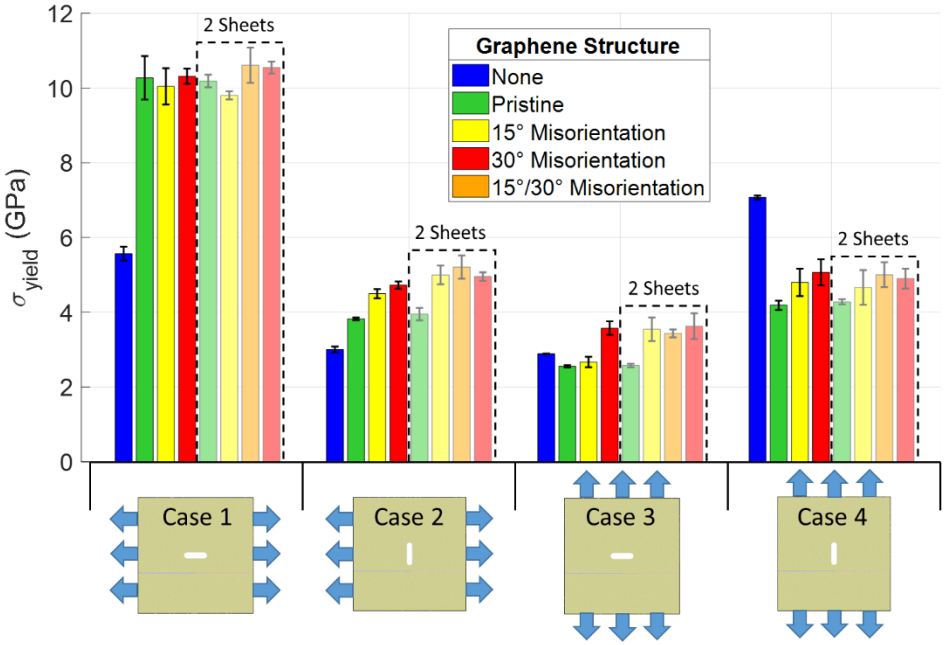

Figure 5.4. Stress at first dislocation in Ni graphene nanocomposites vs. graphene structure and sample loading direction and crack orientations. Models with 2 sheets are in dashed boxes. In cases 1 and 2 the strength of the Ni matrix is supplemented by the graphene sheet. The difference in yield stress is due to stress concentration generated by the crack, which is much higher in case 2. In cases 3 and 4 the Ni matrix hardly receives any support from the graphene sheet because of its normal orientation relative to the load. The difference in yield stress is again due to stress concentration generated by the crack, which is higher in case 3. Case 4 yields by delamination at the interface of Ni and graphene, before stress level raises to generate dislocations.

5.3.1.1 Case 1: loading direction and crack orientation parallel to graphene sheet

The pure Ni sample in case 1 has yield stress around 5.6 GPa and a yield strain of around 2.5%. The case 1 samples containing pristine graphene have yield stress of 10.3 and 10.2 GPa and yield strain of 5.8% and 5.7% for 1 and 2 sheets respectively. The case 1 samples with polycrystalline graphene have an average yield stress of 10.2 and 10.3 GPa and an average yield strain of 5.9% and 6.0% for 1 and 2 sheets respectively.

All case 1 samples with graphene perform substantially better than pure Ni, with a minimum 76% increase in yield stress and a minimum 131% increase in yield strain. The difference in yield stress between pristine and polycrystalline samples is not substantial. The

inclusion of two separate pristine or polycrystalline graphene sheets provides little to no improvement to yield stress or strain.

In two of the samples, we observe bond breaking in the graphene sheet before dislocation nucleation is initiated, as shown in Figure 5.5. This occurs in both 1 and 2 sheet samples with 15° misoriented graphene. Bond breaking in 15° misoriented samples likely caused them to perform poorly compared to pristine samples. All other case 1 samples experienced no bond breaking in the graphene sheet prior to dislocation nucleation. Immediately before the breaking of bonds in graphene, at around 3.7-3.8% strain, we observe the formation of nanowires, as seen in previous computational work [69, 70].

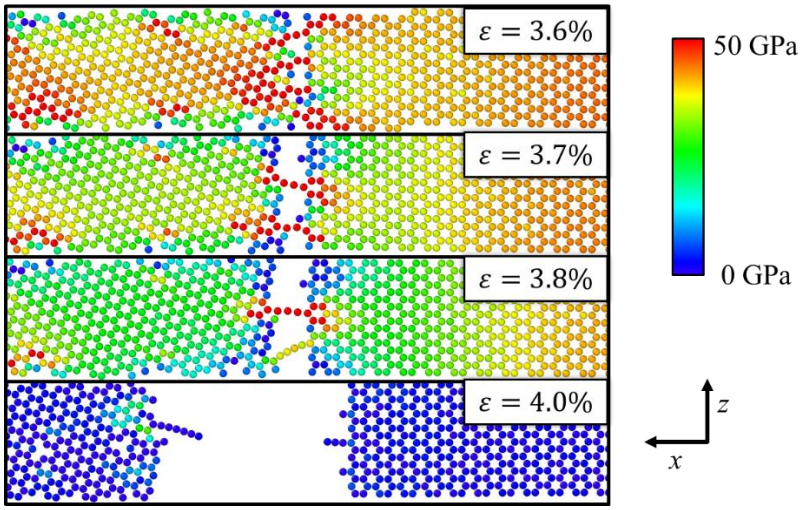

Figure 5.5. Breaking of graphene sheet for case 1 sample with one 15° misoriented graphene sheet. Only carbon atoms are shown. Atoms are colored based on their per-atom stress in the *x* direction. This breaking happens before any dislocation nucleation in the Ni matrix. Samples with pristine or 30° misoriented graphene sheets did not experience any bond breaking in the sheet before dislocation nucleation.

In comparing the different cases (1-4), we find that the highest yield stress by far occurs in case 1, where both loading direction and crack orientation are parallel to the graphene sheet. In case 1 dislocations only occur at very high stress. This is because stress concentration at a crack tip is the primary cause of initial dislocation. In case 1 the defined crack tip is not sharp, rather it

is a blunt crack. When dislocations finally do occur for this case they are catastrophic and widespread due to the very high strain at which they begin, as shown in the failure process in Figure 5.6.

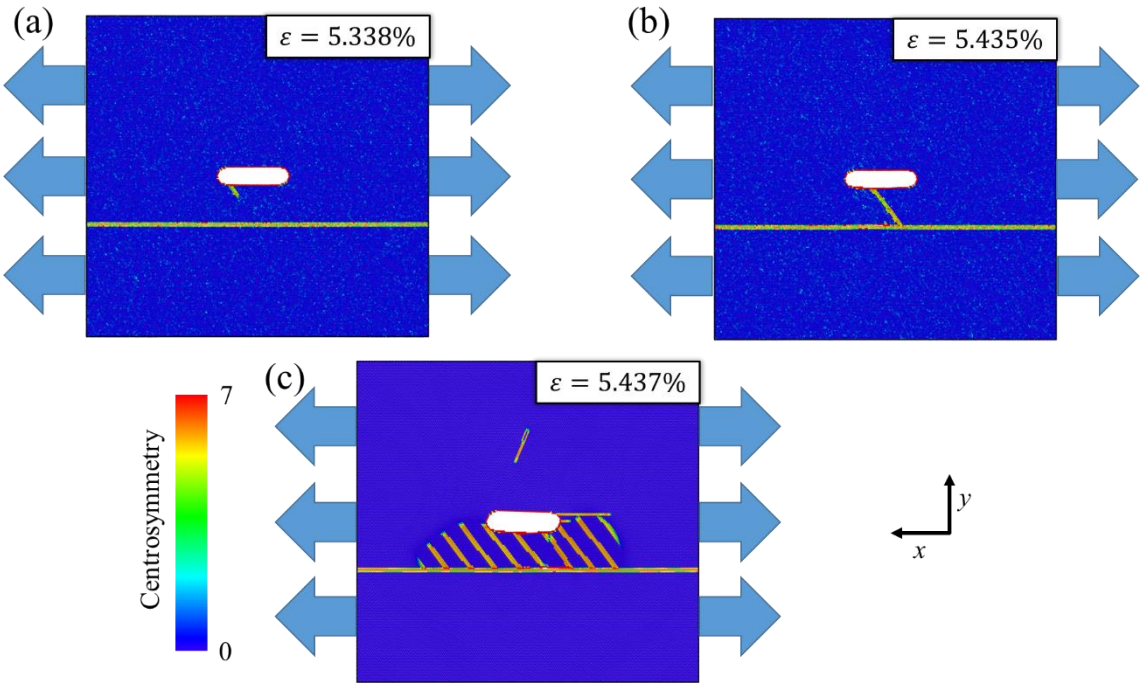

Figure 5.6. Development of dislocations in case 1 sample with pristine graphene. (a) Dislocation begins to nucleate from blunted crack edge. (b) Dislocation fully nucleates and is inhibited by the graphene sheet. (c) Widespread dislocation nucleation, with dislocations being inhibited by the graphene sheet. (This occurs even when the graphene sheet breaks, as the presence of the graphene sheet keeps the upper Ni layers from directly contacting the lower Ni layers.) Atoms are colored based on centrosymmetry [71]. Note that widespread dislocations are inhibited by the graphene sheet from crossing into the lower region of the Ni matrix.

5.3.1.2 Case 2: loading direction parallel to graphene sheet, crack orientation normal to graphene sheet

The pure Ni sample in case 2 has yield stress around 3.0 GPa and a yield strain around 1.3%. This is lower than case 1 due to higher stress concentration at the crack tip in case 2 geometry. Case 2 samples with pristine graphene have yield stress around 3.8 and 4.0 GPa and yield strain around 1.9% and 2.0% for 1 and 2 sheets respectively. Case 2 samples with

polycrystalline graphene have an average yield stress of around 4.6 GPa and 5.1 GPa and an average yield strain of around 2.4% and 2.7% for 1 and 2 sheets respectively.

The sharp crack tip in case 2 samples with graphene present cause dislocations to nucleate at stress levels that are 49-63% lower than in case 1. The dislocations in case 2 are emitted from the crack tip, unlike the widespread dislocation behavior seen in case 1. All case 2 samples with graphene performed better than pure Ni, with a minimum of 27% increase in yield stress and a minimum 48% increase in yield strain. Samples with misoriented graphene sheets show higher yield stress and strain than samples with pristine sheets, with an average 21% increase in yield stress and 26% increase in yield strain for single sheet samples, and an average 28% increase in yield stress and 35% increase in yield strain for samples with two sheets.

5.3.1.3 Case 3: loading direction normal to graphene sheet, crack orientation parallel to graphene sheet

The pure Ni sample in case 3 has yield stress around 2.9 GPa and a yield strain around 1.1%. This is close to the case 2 values because they both have high stress concentration at the crack tip. Case 3 samples with pristine graphene have yield stress around 2.6 GPa and yield strain around 0.9% for both 1 and 2 sheets. Case 3 samples with polycrystalline graphene have an average yield stress around 3.1 and 3.5 GPa and an average yield strain around 1.2% and 1.4% for 1 and 2 sheets respectively.

Compared to pure Ni, samples with pristine graphene show a 10% decrease in yield stress and a 18% decrease in yield strain. In contrast, when compared to pure Ni, samples with misoriented graphene show an average 7% increase in yield stress and a 9% increase in yield strain with one sheet, and an average 21% increase in yield stress and a 27% increase in yield strain with

two sheets. This means that polycrystalline graphene shows an average 27% increase in yield stress and 44% increase in yield strain over pristine graphene in case 3 samples.

In case 3 delamination occurs shortly after the first dislocation nucleation, and initiates at the point of contact between the dislocation and the graphene sheet. This effect is shown in Figure 5.7, where a dislocation moving to the Ni-graphene interface begins the delamination process. The point of contact between the dislocation and graphene sheet is a line defect at which stress concentrates, exceeding the maximum stress before delamination must occur. This stress concentration ultimately separates the graphene sheet from Ni (111) surface. This occurs for all samples with graphene present, whether pristine or polycrystalline.

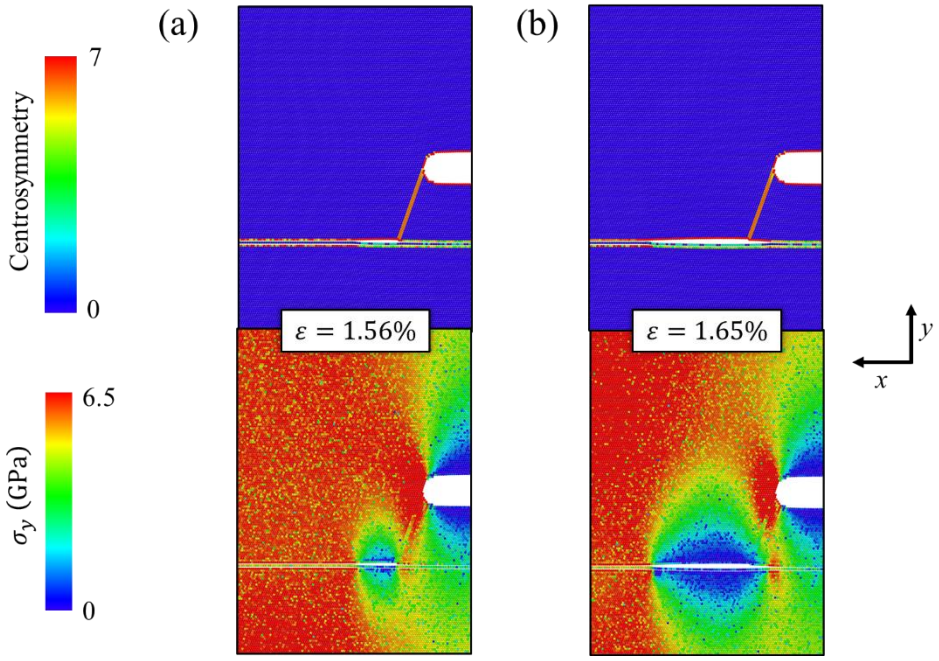

Figure 5.7. Mechanisms of delamination for a typical case 3 sample, with delamination initiated at contact between dislocation and graphene sheet. Sample shows a 15° misoriented graphene sheet. (a) Dislocation contacting graphene sheet, generating a stress concentration at the graphene sheet at 1.56% strain. (b) Delamination developing from dislocation point of contact at 1.65% strain. Top figures are colored by centrosymmetry while bottom figures are colored by stress in the *y* direction. A stress concentration is generated at the point of contact between the dislocation and the graphene sheet, which quickly initiates delamination.

5.3.1.4 Case 4: loading direction and crack orientation normal to graphene sheet

The pure Ni sample in case 4 has yield stress around 7.1 GPa and yield strain around 2.7%. This is more like case 1 because of the lower stress concentration based on the crack orientation. Case 4 samples with pristine graphene have yield stress around 4.2 and 4.3 GPa and yield strain around 1.5% and 1.6% for 1 and 2 sheets respectively. Case 4 samples with polycrystalline graphene have an average yield stress around 4.9 GPa and an average yield strain around 1.8% for both 1 and 2 sheets.

In case 4 delamination occurs without any dislocation nucleation for all samples with graphene present. Compared to pure Ni, samples with pristine sheets show an average 40% decrease in yield stress and 43% decrease in yield strain. Samples with polycrystalline sheets delaminate at higher yield stress/strain than samples with pristine sheets, with an average 31% decrease in yield stress and 33% decrease in yield strain when compared to pure Ni. Polycrystalline sheets provide an average 15% increase in yield stress and 16% increase in yield strain over pristine graphene.

Delamination occurs in case 4 for the same reason that dislocations are generated catastrophically in case 1. With a blunt crack tip in the Ni matrix, the stress to initiate dislocations in the nanocomposite is close to pure Ni, which is around 5.6 and 7.1 GPa for cases 1 and 4 respectively. Based on our results in case 4, the stress needed to initiate delamination is between 4.0-5.0 GPa when there is no sharp crack tip present in the Ni matrix. The stress at which delamination occurs in case 4 samples is higher than the stress at which dislocations are emitted in case 3 samples. This is because there are no dislocations to initiate delamination in case 4 samples, rather delamination is widespread and rapid when it begins.

5.3.1.5 Summary of Ni-graphene samples with single grain boundary (cases 1 – 4)

Based on sections 5.3.1.1 – 5.3.1.4 we see that the inclusion of graphene in a Ni-matrix results in a composite material with increased strength parallel to the graphene sheet, and decreased strength normal to the graphene sheet. Cases 1 and 2 both show that when loading is parallel to the graphene sheet the stress at yield is improved. Cases 3 and 4 show that loading normal to the graphene sheet generally leads to lower stress for yield.

Our results in the different cases shows that the orientation of graphene relative to loading direction has a significant impact on the material properties of nanocomposites. Yazdandoost et al. prepared nanocrystalline Ni-graphene, with graphene dispersed at random orientations, and tested it under nanoindentation [15]. They found that specific graphene orientations were better able to strengthen the nanocomposite, with orientations normal to the compressive load being ideal in their case. Alian et al. also found that the orientation of graphene sheets greatly affects the mechanical properties of nanocomposites possessing them in testing polymer-graphene nanocomposite under nanoindentation [72].

When we compare our samples with pristine graphene to those with polycrystalline graphene, we determine that stress at yield is affected by the structure of the graphene sheet. Generally, Ni-graphene samples with polycrystalline graphene have higher stress and strain at yield than Ni-graphene samples with pristine graphene. The cause of polycrystalline graphene's improved properties in Ni-graphene is investigated further in section 5.3.2.

5.3.2 Analysis of Ni-graphene samples with multiple grain boundaries

Pristine graphene is known to have higher strength than polycrystalline graphene. However, our results for case 1 shows that the inclusion of pristine or polycrystalline graphene in

the Ni-graphene nanocomposite produce approximately the same yield stress, while in case 2 polycrystalline graphene produces higher yield stress than pristine graphene. We want to determine whether this effect carries over when comparing pristine graphene sheets to polycrystalline sheets that possess multiple non-rectangular grain boundaries. We study this by simulating a tensile load on the larger Ni-graphene model previously outlined in the methods section. This study is carried out for both case 1 and case 2 samples because in these cases graphene is under a tensile loading, where the difference in strength between pristine and polycrystalline graphene should play a dominant role.

5.3.2.1 Comparison of yield stress

The yield stress for the larger case 1 and 2 samples is shown in Figure 5.8. For case 1 samples with pristine or polycrystalline graphene with grain sizes of 250 Å, 158 Å, or 100 Å, the yield stress is around 9.9, 10.2, 10.4, and 10.3 GPa and the yield strain is around 5.4%, 5.7%, 5.8%, and 5.8% respectively. The difference in yield stress for case 1 samples with pristine or polycrystalline graphene is minimal. We also find that there is no obvious pattern in yield stress for different grain sizes.

For case 2 samples with pristine graphene or polycrystalline graphene with grain sizes of 250 Å, 158 Å or 100 Å, the yield stress is around 3.8, 5.1, 5.2, and 5.3 GPa and the yield strain is around 2.0%, 2.5%, 2.7%, and 2.8% respectively. Case 2 samples with polycrystalline graphene have an average 36% higher yield stress than samples with pristine graphene. We find that case 2 samples with polycrystalline graphene have higher yield stress than samples with pristine graphene. We also find that case 2 samples with polycrystalline graphene have higher yield stress with decreasing grain size.

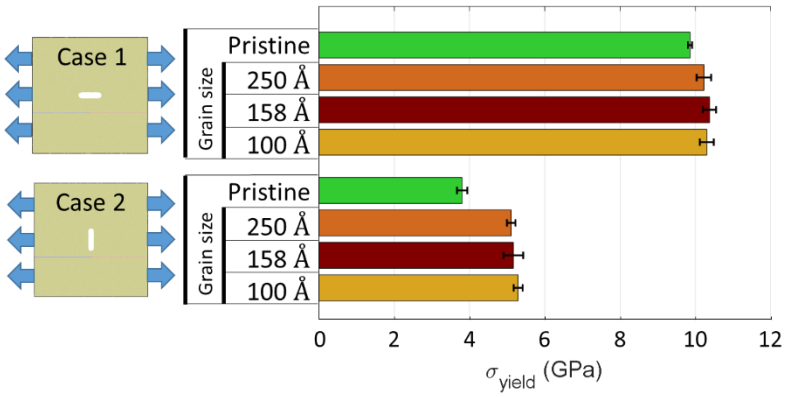

Figure 5.8. Stress at first dislocation for samples with multiple grain boundaries for cases 1 and 2. Stress is shown for samples with pristine graphene and polycrystalline graphene with different average grain size. For case 1 the yield stress for samples with polycrystalline graphene is slightly higher than for samples with pristine graphene. There is no specific trend in the yield stress for samples with polycrystalline graphene of differently sized grains. For case 2, all samples with polycrystalline graphene have noticeably higher stress at yield than the sample with pristine graphene. In addition, stress at yield is slightly higher in polycrystalline samples with smaller grain size for case 2.

5.3.2.2 Interfacial shear stress

In our simulations the entire sample is loaded in the loading direction simultaneously. However, the stress concentration generated at the crack tip provides an extra load that can be transferred from the upper region of the Ni matrix to the lower Ni region by interfacial shear stress between the graphene sheet and Ni layers. This can be analyzed using the shear stress of the total system because interfacial shear stress dominates the shear stress behavior in the different samples, and far from the Ni/graphene interface the shear stress is negligible.

The shear stress vs. displacement for the different samples are shown in Figure 5.9. The samples with polycrystalline graphene consistently approach a mostly steady shear stress that continues until around the point of dislocation. For case 1, the shear stress in the sample with pristine graphene increases and decreases periodically, with peak shear stress higher than shear stress in the samples with polycrystalline graphene, as shown in Figure 5.9(a). For case 2, shear stress in the samples with pristine graphene also alternates between high and low values, but at a

lower peak shear stress than samples with polycrystalline graphene, as shown in Figure 5.9(b). The samples with pristine graphene go through wide fluctuations in shear stress, indicating that there are periods where shear stress is relieved during the simulation before once again increasing.

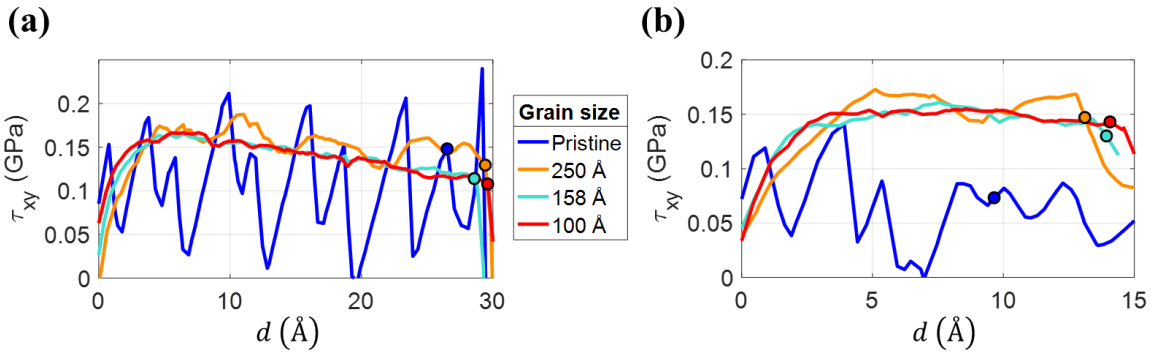

Figure 5.9. Shear stress vs. displacement *d* for Ni-graphene nanocomposite samples with multiple grain boundaries during simulation for (a) case 1 samples, and (b) case 2 samples. Circles on the curve represent the point at which dislocation nucleation initiates in the Ni matrix. Note that pristine samples show several drops in shear stress during displacement, while the polycrystalline samples show more stable shear stress behavior. This indicates that the polycrystalline graphene sheets are more efficient at transferring load from the Ni matrix than the pristine graphene sheet.

The low shear stress seen in samples with pristine graphene, particularly in case 2, indicate that pristine graphene has lower interfacial shear stress than polycrystalline graphene. This means that pristine graphene is less effective at transferring the load generated by the stress concentration from the upper Ni-matrix, which results in lower yield stress and strain. This is in agreement with experimental work which shows that higher interfacial shear stress corresponds to higher interfacial bonding, which in turn leads to higher load transfer and yield strength [23, 27-29]. The shear stress behavior in samples with pristine graphene may correspond to either wrinkling in the sheet itself, or stick-slip motion of the sheet with either of the contiguous Ni layers.

5.3.2.3 Wrinkling in graphene sheets

As discussed in the introduction, the wrinkling of graphene sheets has an impact on the stress distribution at its interface with a metal matrix. We investigate the wrinkling of the graphene

sheet in each of the different Ni-graphene samples with multiple grain boundaries, as well as the effect it has on the per-atom stress in the Ni layer directly above the graphene sheet, as shown in Figure 5.10(a). We do this for case 2 samples at a strain of 1.8%, which is just before dislocation nucleation occurs for the sample with pristine graphene.

The wrinkling of the pristine and polycrystalline graphene sheets is quantified by the deviation in height from the mean height of the sheet in the *y* direction (normal to the sheet), as shown in Figure 5.10(b). We find that the sandwiched polycrystalline sheets have height distributions that are more normal in the *x* direction and more uniform in the z direction than the sandwiched pristine sheet.

To better represent the height distribution of the graphene sheet, we find the variance in height for different sections of the graphene sheet across the *x* direction, with a bin width of 5 Å. Variance is computed by $\mathrm{Var}(y) = \sum(y - \bar{y})^2$, summing over all atoms in the bin. The resulting plot is shown in Figure 5.10(c). This result further demonstrates the waviness of the pristine sheet as compared to the polycrystalline sheets. We observe that the pristine sheet has greater fluctuation in height than the polycrystalline sheets, meaning that the pristine sheet is more wrinkled than the polycrystalline sheets. We also observe that polycrystalline sheets with larger grain size experience slightly higher peaked fluctuation than polycrystalline sheets with smaller grain sizes, implying that smaller grains in a polycrystalline sheet further inhibit the overall sheet's ability to wrinkle.

The effect the wrinkling of the graphene sheet has on the Ni layer directly above the graphene sheet is demonstrated by the stress fields shown in Figure 5.10(d). We find the average stress field of the Ni layer above the graphene sheet for each of our samples with a bin width of 5 Å, as shown in Figure 5.10(e). We observe that the pristine sample exhibits a higher peak stress and a more rapid drop-off in stress about the peak in the *x* direction than the polycrystalline

samples. This higher peak stress will lead to earlier dislocation nucleation. We also observe that samples with polycrystalline graphene of smaller grain size experience lower peak stress and more gradual stress drop-off than samples with polycrystalline graphene of larger grain sizes.

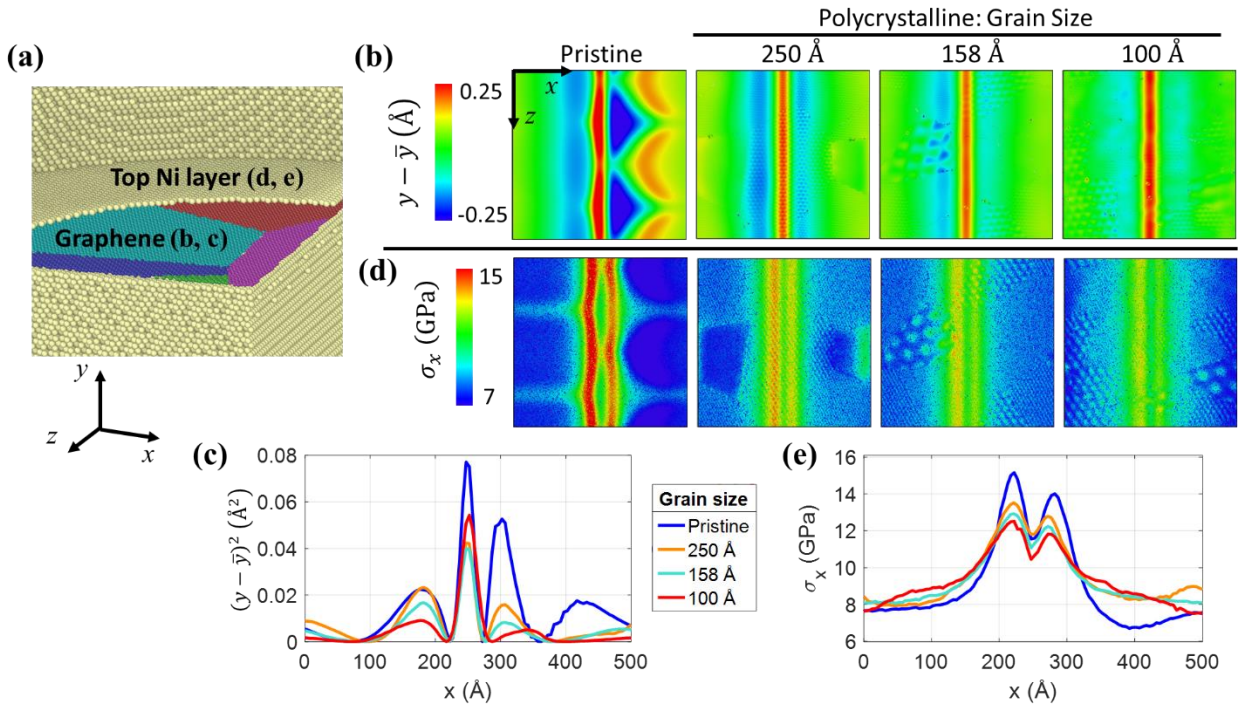

Figure 5.10. (a) Visual to clarify the atom layers used in generating fields for parts (b) and (d) and distributions for parts (c) and (e), with atoms cleared to aid in visualization. Samples are case 2, with either pristine or polycrystalline graphene with different grain sizes. The sample shows a polycrystalline graphene sheet with a grain size of 100 Å. (b) Field showing positional deviation from the mean in the *y* direction for atoms in the graphene sheet. (c) Variance in height (*y* direction) vs. position in the *x* direction for atoms in the graphene sheet, demonstrating the degree of wrinkling present in the sheet. The pristine sheet shows greater variance, and therefore more wrinkling, compared to the polycrystalline sheets. (d) Stress fields in the *x* direction for the Ni layer directly above the graphene sheet for pristine and polycrystalline graphene sheets with varying numbers of grains. (e) Distribution of stress. The strain of the sample is around 1.8% for all fields and distributions.

To compare the wrinkling of the graphene sheet directly with the stress present in contiguous Ni layers, we find the total variance in the graphene sheet and compare it to the peak stress present in the Ni layer directly above the sheet. A plot of this comparison is shown in Figure 5.11 for both case 1 and case 2 samples. We also list polycrystalline graphene grain sizes on the

plot for further analysis. These values are taken at strain levels around 1.8%, which is close to the point of dislocation for the sample with pristine sheet in case 2. We find that case 1 shows no definable relationship between graphene sheet height variance, stress in contiguous Ni layers, or graphene grain size. However, height variance in the graphene sheet is significantly higher for the sample with pristine graphene. Case 2 shows a strong relationship between graphene sheet height variance, stress in contiguous Ni layers and graphene grain size. For case 2 we find that with increasing grain size we have increasing height variance, which corresponds to increasing stress in the Ni layer above the sheet, which will lead to dislocation nucleation in the Ni matrix at lower strain. Our results for case 2 related to the wrinkling of graphene are in agreement with experimental work on Ni-graphene by Li et al. who found that wrinkles in monolayer graphene inhibit their stress transfer efficiency [36]. These results are also in agreement with Jiang et al. who found that well contacted graphene is beneficial to the load transfer effect in Ni-graphene nanocomposite [25].

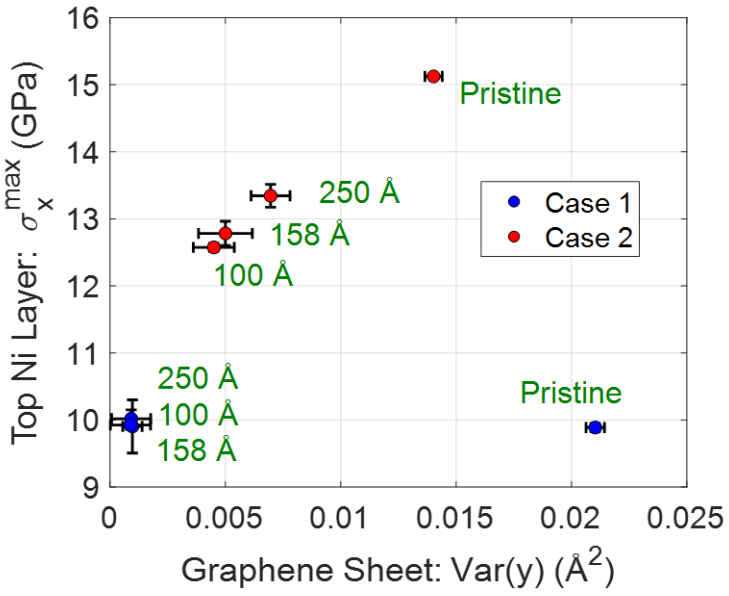

Figure 5.11. Peak *x* component of stress in Ni layer above the graphene sheet vs. variance in height (*y* direction) for graphene sheet for Ni-graphene samples with multiple grain boundaries. Samples

are either case 1 or case 2. Grain sizes are listed beside points in the plot except where graphene is pristine.

5.3.2.4 Summary of Ni-graphene samples with multiple grain boundaries

Our analysis of the larger case 2 Ni-graphene samples demonstrates that pristine graphene sheets experience greater wrinkling than polycrystalline graphene sheets, with fluctuations in shear stress showing points at which the sheet distorts and wrinkles. For case 2 samples, greater wrinkling in pristine and polycrystalline graphene sheets corresponds to higher stresses in the Ni layer in contact with the sheet, which leads to dislocation nucleation at lower strain in the Ni matrix. This agrees with the results from our 500 × 500 × 20 Å Ni-graphene samples and provides an explanation for the behavior they exhibit.

Polycrystalline graphene provides improvements to the mechanical properties of Ni-graphene nanocomposites because of its improved interfacial bonding. Improving the metal/graphene interface strength should improve the mechanical properties of a metal-graphene nanocomposite. Cao et al. found that in-situ grown graphene had improved interfacial bonding with Cu, leading to improvements in the mechanical properties of Cu-graphene nanocomposites [73]. Based on our research, in-situ growth of small-grain polycrystalline graphene could provide better interfacial bonding than large-grain graphene sheets.

5.4. Conclusions

The failure modes we observe in Ni-graphene are dependent on the crack orientation and loading direction to which the nanocomposites are subjected. The failure modes we observe are catastrophic dislocation nucleation, singular dislocation nucleation, delamination initiated after dislocation nucleation, and delamination. The presence of graphene in a Ni matrix, where loading is applied parallel to the graphene sheet, provides for a 27-76% improvement in yield stress and a

48-131% improvement in yield strain over pure Ni depending on the orientation of the crack in the matrix. This improvement in metal-graphene nanocomposite can be further increased, if the graphene is polycrystalline, with an increase in yield stress up to 28% and an increase in yield strain up to 35% over samples with pristine graphene. When graphene is added to a Ni matrix and loading is applied normal to the graphene sheet, we find that the presence of graphene can lead to a decrease in yield stress by as much as 40% for pristine graphene. In this case, polycrystalline graphene can provide a 15-27% increase in yield stress and a 16-44% increase in yield strain compared to pristine graphene.

We find that the superior performance of polycrystalline graphene is due to its improved interfacial shear stress, which is affected by wrinkling that occurs less significantly in polycrystalline than in pristine graphene. Wrinkling in graphene sheets alters the Ni/graphene interface, which affects graphene's interfacial shear stress in the Ni matrix, making the sheet less efficient at load transfer within the matrix. Decreasing the grain size of polycrystalline graphene can further decrease wrinkling, which increases the yield stress of the Ni-graphene sample. Thus our research predicts that polycrystalline graphene will better improve the mechanical properties in Ni-graphene nanocomposites than pristine graphene. This may also apply to other metal-graphene nanocomposites. This is encouraging as graphene is typically found in a polycrystalline form. Our research also indicates that nanocomposites utilizing graphene are advantaged by flaws present in the 2-D material, such as a polycrystalline structure. Identifying flaws in 2-D materials that provide such advantages may enhance future 2-D material based nanocomposite design.

Acknowledgements

We sincerely thank the partial support from Center for Advanced Surface Engineering, under the National Science Foundation Grant No. IIA- 1457888 and the Arkansas EPSCoR Program,

ASSET III, Funding for this research. Authors would like to acknowledge the support in part by the National Science Foundation – United States under the grants ARI#0963249, MRI#0959124 and EPS#0918970, and a grant from Arkansas Science and Technology Authority, managed by Arkansas High Performance Computing Center.

References

[1] J. Zhang, J. Zhao, J. Lu, Intrinsic strength and failure behaviors of graphene grain boundaries, ACS Nano 6(3) (2012) 2704-11.

[2] G.H. Lee, R.C. Cooper, S.J. An, S. Lee, A. van der Zande, N. Petrone, A.G. Hammerberg, C. Lee, B. Crawford, W. Oliver, J.W. Kysar, J. Hone, High-strength chemical-vapor-deposited graphene and grain boundaries, Science 340(6136) (2013) 1073-6.

[3] P.Y. Huang, C.S. Ruiz-Vargas, A.M. van der Zande, W.S. Whitney, M.P. Levendorf, J.W. Kevek, S. Garg, J.S. Alden, C.J. Hustedt, Y. Zhu, Grains and grain boundaries in single-layer graphene atomic patchwork quilts, Nature 469(7330) (2011) 389-392.

[4] J. Kotakoski, J.C. Meyer, Mechanical properties of polycrystalline graphene based on a realistic atomistic model, Phys Rev B 85(19) (2012) 195447.

[5] M. Chen, S. Quek, Z. Sha, C. Chiu, Q. Pei, Y. Zhang, Effects of grain size, temperature and strain rate on the mechanical properties of polycrystalline graphene–A molecular dynamics study, Carbon 85 (2015) 135-146.

[6] A. Zandiatashbar, G.H. Lee, S.J. An, S. Lee, N. Mathew, M. Terrones, T. Hayashi, C.R. Picu, J. Hone, N. Koratkar, Effect of defects on the intrinsic strength and stiffness of graphene, Nature communications 5 (2014) 3186.

[7] H.I. Rasool, C. Ophus, W.S. Klug, A. Zettl, J.K. Gimzewski, Measurement of the intrinsic strength of crystalline and polycrystalline graphene, Nature communications 4 (2013) 2811.

[8] R. Grantab, V.B. Shenoy, R.S. Ruoff, Anomalous strength characteristics of tilt grain boundaries in graphene, Science 330(6006) (2010) 946-948.

[9] G. Lopez-Polin, C. Gomez-Navarro, V. Parente, F. Guinea, M.I. Katsnelson, F. Perez-Murano, J. Gomez-Herrero, Increasing the elastic modulus of graphene by controlled defect creation, Nature Physics 11(1) (2015) 26-31.

[10] S. Stankovich, D.A. Dikin, G.H. Dommett, K.M. Kohlhaas, E.J. Zimney, E.A. Stach, R.D. Piner, S.T. Nguyen, R.S. Ruoff, Graphene-based composite materials, nature 442(7100) (2006) 282-286.

[11] D.-B. Xiong, M. Cao, Q. Guo, Z. Tan, G. Fan, Z. Li, D. Zhang, Graphene-and-copper artificial nacre fabricated by a preform impregnation process: bioinspired strategy for strengthening-toughening of metal matrix composite, Acs Nano 9(7) (2015) 6934-6943.

[12] Y. Kim, J. Lee, M.S. Yeom, J.W. Shin, H. Kim, Y. Cui, J.W. Kysar, J. Hone, Y. Jung, S. Jeon, S.M. Han, Strengthening effect of single-atomic-layer graphene in metal-graphene nanolayered composites, Nature communications 4 (2013) 2114.

[13] Z. Hu, G. Tong, D. Lin, C. Chen, H. Guo, J. Xu, L. Zhou, Graphene-reinforced metal matrix nanocomposites–a review, Materials Science and Technology 32(9) (2016) 930-953.

[14] I.A. Ovid'ko, Metal-Graphene Nanocomposites with Enhanced Mechanical Properties: A Review, Rev Adv Mater Sci 38(2) (2014) 190-200.

[15] F. Yazdandoost, A.Y. Boroujeni, R. Mirzaeifar, Nanocrystalline nickel-graphene nanoplatelets composite: Superior mechanical properties and mechanics of properties enhancement at the atomistic level, Physical Review Materials 1(7) (2017) 076001.

[16] Z. Yang, D. Wang, Z. Lu, W. Hu, Atomistic simulation on the plastic deformation and fracture of bio-inspired graphene/Ni nanocomposites, Applied Physics Letters 109(19) (2016) 191909.

[17] S.W. Chang, A.K. Nair, M.J. Buehler, Nanoindentation study of size effects in nickel-graphene nanocomposites, Phil Mag Lett 93(4) (2013) 196-203.

[18] S.E. Muller, A.K. Nair, Dislocation Nucleation in Nickel-Graphene Nanocomposites Under Mode I Loading, Jom 68(7) (2016) 1909-1914.

[19] Y. ZhenYu, S. Jian, L. ZiXing, H. WenJun, Strenghening mechanism of graphene/Ni nanolayered composite nanowires under uniaxial compression, SCIENCE CHINA Physics, Mechanics & Astronomy 59(3) (2016) 634603.

[20] J.A. Robinson, M. LaBella, M. Zhu, M. Hollander, R. Kasarda, Z. Hughes, K. Trumbull, R. Cavalero, D. Snyder, Contacting graphene, Applied Physics Letters 98(5) (2011) 053103.

[21] T. Yoon, W.C. Shin, T.Y. Kim, J.H. Mun, T.-S. Kim, B.J. Cho, Direct measurement of adhesion energy of monolayer graphene as-grown on copper and its application to renewable transfer process, Nano letters 12(3) (2012) 1448-1452.

[22] C. Gong, D. Hinojos, W. Wang, N. Nijem, B. Shan, R.M. Wallace, K. Cho, Y.J. Chabal, Metal–graphene–metal sandwich contacts for enhanced interface bonding and work function control, Acs Nano 6(6) (2012) 5381-5387.

[23] Z. Ren, N. Meng, K. Shehzad, Y. Xu, S. Qu, B. Yu, J. Luo, Mechanical properties of nickel-graphene composites synthesized by electrochemical deposition, Nanotechnology 26(6) (2015) 065706.

[24] H. Yue, L. Yao, X. Gao, S. Zhang, E. Guo, H. Zhang, X. Lin, B. Wang, Effect of ball-milling and graphene contents on the mechanical properties and fracture mechanisms of graphene nanosheets reinforced copper matrix composites, Journal of Alloys and Compounds 691 (2017) 755-762.

[25] J. Jiang, X. He, J. Du, X. Pang, H. Yang, Z. Wei, In-situ fabrication of graphene-nickel matrix composites, Materials Letters 220 (2018) 178-181.

[26] S. Sharma, P. Kumar, R. Chandra, Mechanical and thermal properties of graphene–carbon nanotube-reinforced metal matrix composites: A molecular dynamics study, J Compos Mater 51(23) (2017) 3299-3313.

[27] G. Guo, Y. Zhu, Cohesive-shear-lag modeling of interfacial stress transfer between a monolayer graphene and a polymer substrate, Journal of Applied Mechanics 82(3) (2015) 031005.

[28] K. Fu, X. Zhang, C. Shi, E. Liu, F. He, J. Li, N. Zhao, C. He, An approach for fabricating Ni@ graphene reinforced nickel matrix composites with enhanced mechanical properties, Materials Science and Engineering: A (2017).

[29] L. Gong, I.A. Kinloch, R.J. Young, I. Riaz, R. Jalil, K.S. Novoselov, Interfacial stress transfer in a graphene monolayer nanocomposite, Advanced Materials 22(24) (2010) 2694-2697.

[30] J.C. Meyer, A.K. Geim, M.I. Katsnelson, K.S. Novoselov, T.J. Booth, S. Roth, The structure of suspended graphene sheets, arXiv preprint cond-mat/0701379 (2007).

[31] T.M. Paronyan, E.M. Pigos, G. Chen, A.R. Harutyunyan, Formation of ripples in graphene as a result of interfacial instabilities, ACS nano 5(12) (2011) 9619-9627.

[32] M.S. Bronsgeest, N. Bendiab, S. Mathur, A. Kimouche, H.T. Johnson, J. Coraux, P. Pochet, Strain relaxation in CVD graphene: wrinkling with shear lag, Nano letters 15(8) (2015) 5098-5104.

[33] J. Huang, Q. Han, A Molecular Dynamics Study on Wrinkles in Graphene with Simply Supported Boundary under In-Plane Shear, Journal of Nanomaterials 2017 (2017).

[34] Z. Ye, C. Tang, Y. Dong, A. Martini, Role of wrinkle height in friction variation with number of graphene layers, AIP, 2012.

[35] H. Qin, Y. Sun, J.Z. Liu, Y. Liu, Mechanical properties of wrinkled graphene generated by topological defects, Carbon 108 (2016) 204-214.

[36] Z. Li, I.A. Kinloch, R.J. Young, K.S. Novoselov, G. Anagnostopoulos, J. Parthenios, C. Galiotis, K. Papagelis, C.-Y. Lu, L. Britnell, Deformation of wrinkled graphene, Acs Nano 9(4) (2015) 3917-3925.

[37] Z.P. Xu, M.J. Buehler, Interface structure and mechanics between graphene and metal substrates: a first-principles study, J Phys-Condens Mat 22(48) (2010).

[38] M. Fuentes-Cabrera, M.I. Baskes, A.V. Melechko, M.L. Simpson, Bridge structure for the graphene/Ni(111) system: A first principles study, Phys Rev B 77(3) (2008).

[39] G. Bertoni, L. Calmels, A. Altibelli, V. Serin, First-principles calculation of the electronic structure and EELS spectra at the graphene/Ni (111) interface, Phys Rev B 71(7) (2005) 075402.

[40] K. Kim, Z. Lee, W. Regan, C. Kisielowski, M. Crommie, A. Zettl, Grain boundary mapping in polycrystalline graphene, ACS nano 5(3) (2011) 2142-2146.

[41] Z. Song, V.I. Artyukhov, B.I. Yakobson, Z. Xu, Pseudo Hall–Petch strength reduction in polycrystalline graphene, Nano letters 13(4) (2013) 1829-1833.

[42] C. Rycroft, Voro++: A three-dimensional Voronoi cell library in C++, (2009).

[43] D. Mordehai, M. Kazakevich, D.J. Srolovitz, E. Rabkin, Nanoindentation size effect in single-crystal nanoparticles and thin films: A comparative experimental and simulation study, Acta Materialia 59(6) (2011) 2309-2321.

[44] M.S. Daw, M.I. Baskes, Semiempirical, Quantum-Mechanical Calculation of Hydrogen Embrittlement in Metals, Phys Rev Lett 50(17) (1983) 1285-1288.

[45] S. Foiles, M. Baskes, M. Daw, Embedded-atom-method functions for the fcc metals Cu, Ag, Au, Ni, Pd, Pt, and their alloys, Phys Rev B 33(12) (1986) 7983.

[46] S.J. Stuart, A.B. Tutein, J.A. Harrison, A reactive potential for hydrocarbons with intermolecular interactions, J Chem Phys 112(14) (2000) 6472-6486.

[47] Q. Pei, Y. Zhang, V. Shenoy, A molecular dynamics study of the mechanical properties of hydrogen functionalized graphene, Carbon 48(3) (2010) 898-904.

[48] C. Lee, X.D. Wei, J.W. Kysar, J. Hone, Measurement of the elastic properties and intrinsic strength of monolayer graphene, Science 321 (2008) 385-388.

[49] S.-P. Huang, D.S. Mainardi, P.B. Balbuena, Structure and dynamics of graphite-supported bimetallic nanoclusters, Surf Sci 545(3) (2003) 163-179.

[50] Y. Yan, J. Lv, S. Liu, Chirality and grain boundary effects on indentation mechanical properties of graphene coated on nickel foil, Nanotechnology 29(16) (2018) 165703.

[51] Y. Yan, S. Zhou, S. Liu, Atomistic simulation on nanomechanical response of indented graphene/nickel system, Computational Materials Science 130 (2017) 16-20.

[52] S. Huang, B. Wang, M. Feng, X. Xu, X. Cao, Y. Wang, Carbon nanoscrolls fabricated from graphene nanoribbons using Ni nanowire templates: A molecular dynamics simulation, Surf Sci 634 (2015) 3-8.

[53] R. Rasuli, K. Mostafavi, J. Davoodi, Molecular dynamics simulation of graphene growth on Ni (100) facet by chemical vapor deposition, Journal of Applied Physics 115(2) (2014) 024311.

[54] S.W. Chang, A.K. Nair, M.J. Buehler, Geometry and temperature effects of the interfacial thermal conductance in copper- and nickel-graphene nanocomposites, Journal of physics. Condensed matter : an Institute of Physics journal 24(24) (2012) 245301.

[55] X. Liu, F. Wang, H. Wu, W. Wang, Strengthening metal nanolaminates under shock compression through dual effect of strong and weak graphene interface, Applied Physics Letters 104(23) (2014) 231901.

[56] S.M. Kozlov, F. Viñes, A. Görling, Bonding mechanisms of graphene on metal surfaces, The Journal of Physical Chemistry C 116(13) (2012) 7360-7366.

[57] I. Hamada, M. Otani, Comparative van der Waals density-functional study of graphene on metal surfaces, Phys Rev B 82(15) (2010) 153412.

[58] M. Vanin, J.J. Mortensen, A. Kelkkanen, J.M. Garcia-Lastra, K.S. Thygesen, K.W. Jacobsen, Graphene on metals: A van der Waals density functional study, Phys Rev B 81(8) (2010) 081408.

[59] W.-B. Zhang, C. Chen, P.-Y. Tang, First-principles study for stability and binding mechanism of graphene/Ni (111) interface: Role of vdW interaction, The Journal of chemical physics 141(4) (2014) 044708.

[60] W. Zhao, S.M. Kozlov, O. Höfert, K. Gotterbarm, M.P. Lorenz, F. Vines, C. Papp, A. Görling, H.-P. Steinrück, Graphene on Ni (111): coexistence of different surface structures, The Journal of Physical Chemistry Letters 2(7) (2011) 759-764.

[61] J.A. Elliott, Y. Shibuta, H. Amara, C. Bichara, E.C. Neyts, Atomistic modelling of CVD synthesis of carbon nanotubes and graphene, Nanoscale 5(15) (2013) 6662-6676.

[62] T. Olsen, J. Yan, J.J. Mortensen, K.S. Thygesen, Dispersive and covalent interactions between graphene and metal surfaces from the random phase approximation, Phys Rev Lett 107(15) (2011) 156401.

[63] J. Zheng, Y. Wang, L. Wang, R. Quhe, Z. Ni, W.-N. Mei, Z. Gao, D. Yu, J. Shi, J. Lu, Interfacial properties of bilayer and trilayer graphene on metal substrates, Scientific reports 3 (2013) 2081.

[64] P. Lazar, S. Zhang, K.r. Šafářová, Q. Li, J.P. Froning, J. Granatier, P. Hobza, R. Zbořil, F. Besenbacher, M. Dong, Quantification of the interaction forces between metals and graphene by quantum chemical calculations and dynamic force measurements under ambient conditions, ACS nano 7(2) (2013) 1646-1651.

[65] S. Plimpton, Fast Parallel Algorithms for Short-Range Molecular-Dynamics, J Comput Phys 117(1) (1995) 1-19.

[66] A.P. Thompson, S.J. Plimpton, W. Mattson, General formulation of pressure and stress tensor for arbitrary many-body interaction potentials under periodic boundary conditions, J Chem Phys 131(15) (2009) 154107.

[67] A. Stukowski, Visualization and analysis of atomistic simulation data with OVITO-the Open Visualization Tool, Model Simul Mater Sc 18(1) (2010).

[68] B. Mortazavi, G. Cuniberti, Atomistic modeling of mechanical properties of polycrystalline graphene, Nanotechnology 25(21) (2014) 215704.

[69] B. Yang, S. Wang, Y. Guo, J. Yuan, Y. Si, S. Zhang, H. Chen, Strength and failure behavior of a graphene sheet containing bi-grain-boundaries, RSC Advances 4(97) (2014) 54677-54683.

[70] S. Wang, B. Yang, J. Yuan, Y. Si, H. Chen, Large-scale molecular simulations on the mechanical response and failure behavior of a defective graphene: cases of 5–8–5 defects, Scientific reports 5 (2015) 14957.

[71] C.L. Kelchner, S. Plimpton, J. Hamilton, Dislocation nucleation and defect structure during surface indentation, Phys Rev B 58(17) (1998) 11085.

[72] A. Alian, M. Dewapriya, S. Meguid, Molecular dynamics study of the reinforcement effect of graphene in multilayered polymer nanocomposites, Materials & Design 124 (2017) 47-57.

[73] M. Cao, D.-B. Xiong, Z. Tan, G. Ji, B. Amin-Ahmadi, Q. Guo, G. Fan, C. Guo, Z. Li, D. Zhang, Aligning graphene in bulk copper: Nacre-inspired nanolaminated architecture coupled with in-situ processing for enhanced mechanical properties and high electrical conductivity, Carbon 117 (2017) 65-74.

Chapter 6

Paper 3: Carbyne as a fiber in metal-matrix nanocomposites: A first principles study

Abstract

Carbyne is a lightweight 1-D carbon allotrope with exceptional mechanical properties, making it an ideal candidate as a fiber in metal-matrix nanocomposites. However, carbyne is also unstable in many environments, which may negatively affect its potential mechanical contributions. In this study, we use density functional theory to predict the maximum local stiffness in a nanocomposite composed of carbyne within a nickel (Ni) matrix. We compute the local specific stiffness of carbyne-Ni from energy-strain relations, allowing us to avoid the ambiguity of volume approximations inherent in materials with less than three dimensions. We use Bader charge analysis to study how charge transfers within the nanocomposite and its effect on local specific stiffness. We find that carbyne enhances the local specific stiffness of carbyne-Ni nanocomposites when it is dielectrically screened from the Ni matrix using graphene sheets, with ~25% increase in specific stiffness over a graphene-Ni nanocomposite. When carbyne is not dielectrically screened its bond structure breaks down, carbon's average electronic charge per-atom increases, and there is ~60% drop in the local specific stiffness compared to the dielectrically screened case.

6.1 Introduction

Carbon allotropes have material properties which vary widely depending on their dimensionality, including 0-D, quasi 1-D, and 2-D allotropes in the form of fullerenes, carbon nanotubes and graphene respectively [1]. One carbon allotrope that is on the cutting edge of current research is carbyne (shown in Figure 6.1(a)), a 1-D material consisting of *sp*-hybridized carbon atoms forming a chain [2]. There has been much advancement in producing and identifying this

elusive allotrope by experiments over the past several years [3-6]. The motivation for synthesizing carbyne lies in part on its exceptional mechanical properties and light weight. Experiments have found that carbyne has a tensile strength of around 270 GPa [7], which is twice that of graphene [8]. Carbyne has also been predicted to have a Young's modulus of around 3 TPa [9], three times greater than graphene [8]. One potential application for carbyne, the smallest nanowire, is as a fiber in metal-matrix nanocomposites. Carbon allotropes often contribute toward stronger and lighter-weight composites, traits desirable in many sectors including the automotive and aerospace industries [10]. The novelty here lies in the convergence of dimensions, i.e. 1D to 3D coupling. The utilization of 1-D materials like carbyne for nanocomposites has excellent application opportunities in both engineering and biomedical fields [11].

Carbyne chains have either a cumulene structure with repeating double bonds, or a polyyne structure with alternating single and triple bonds [12]. For a theoretical chain of infinite length carbyne's polyyne structure is favorable and cumulene is unstable [13]. However, for chains of finite length cumulene can be stable, and indeed favorable; this is likely due to the presence of edge atoms [14]. The predominant structure carbyne takes is highly dependent on the materials it interacts with. Yuan et al. investigated carbyne forming on transition metal surfaces using first principles [15]. They found that carbyne forms a polyyne structure on copper surfaces, while cumulene is favorable on nickel (Ni). The chains they investigated were low in number of atoms, but it is worth noting that shorter carbyne chains tend to possess greater strength than longer carbyne chains [14, 16].

Because of the instability of linear carbon chains, [17, 18], it is important to determine the stability of carbyne and changes that may affect its structure, such as kinking [19-21], and changes to bond length [21]. Carbyne chains of sufficient length may transition into a different carbon

allotrope altogether. Gao et al. investigated graphene growth on Ni (111) surface and found that carbyne chains consisting of less than 12 atoms will remain stable as linear chains on a Ni (111) surface, while chains with 12 or more carbon atoms will tend to produce “graphene islands” [22]. The instability of carbyne can be countered by preparing its environment against the formation of undesirable bonds and charge distortion [23]. One method for preserving carbyne’s stability is by confining it within carbon nanotubes [5, 24-26]; this protects the inner carbyne chain from external interactions by acting as a dielectric screen [27]. Similarly, graphene may also serve as an effective dielectric screen for carbyne in a nanocomposite, as shown in Figure 6.1(b). This could prove particularly effective as carbon wires are one of the secondary structures that form during yielding in graphene [28-30]. If multiple graphene sheets are stacked and breakage begins in an interior sheet, any resulting carbyne may be stabilized by the surrounding sheets, which could improve local stiffness in the material.

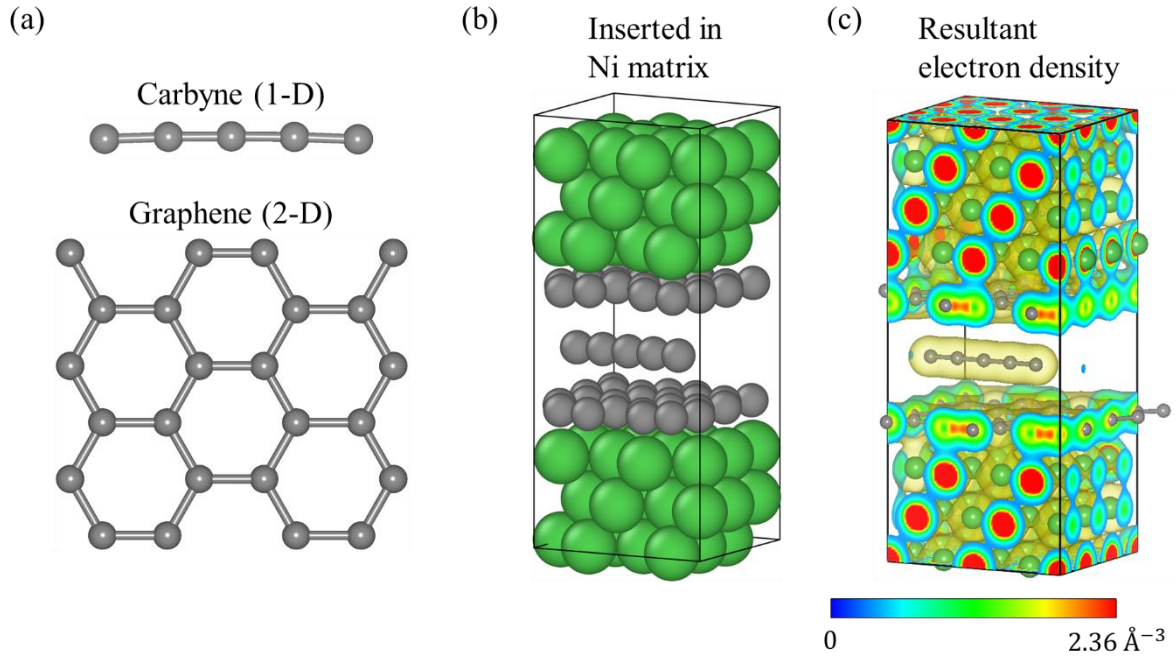

Figure 6.1. (a) Visual of carbyne (in its cumulene form) and graphene. (b) Visual of nanocomposite composed of carbyne sandwiched by graphene, which is itself embedded in a Ni matrix. (c) Visual of electron density isosurfaces of nanocomposite, with the isosurface level set at 0.337 $Å^{-3}$.

The combination of organic compounds with metals can produce materials with unique and desirable properties [31]. As methods for carbyne synthesis improve [5, 32, 33] it is important to explore some of the potential advantages and disadvantages of carbyne-based nanocomposites. In this study, we model a nanocomposite consisting of multiple small carbyne chains sandwiched within a Ni matrix. We use first principles to predict the maximum local stiffness of the material around the carbyne. We also investigate the use of graphene to dielectrically screen carbyne from charge distortions caused by the Ni matrix. We compare carbyne's contribution to the local stiffness when it is either screened or unscreened, and how this changes with the number of carbyne chains. We use Ni as the metal matrix in our investigation because of the stability of carbon chains deposited on Ni substrates as predicted computationally [15, 22, 34, 35] and observed experimentally [21]. We investigate how the local electron density distribution between carbyne chains and Ni affects the local stiffness of the nanocomposite. This study provides direction for further research and development of carbyne-metal nanocomposites.

6.2 Methods

Effectively modeling carbyne-Ni nanocomposites requires us to consider the bond structure of carbyne and how it might change in the presence of Ni. We do this from first principles using density functional theory (DFT) as implemented in Quantum-Espresso [36]. The PBE generalized gradient exchange correlation functional [37] and projected augmented wave (PAW) pseudopotentials [38] are used to treat Ni and C interactions for all simulations, with a kinetic energy cutoff of 558 eV. Spin-polarization is included for calculations using Ni. Grimme's DFT-D2 van der Waals correction [39] is used in all calculations. Convergence in relaxation is reached when all force components on atoms are less than 26 meV/Å, and the change in total energy is less than 1 meV/atom. Periodic boundaries are present in all simulations, and the first Brillouin zone

is sampled with a 2×1×2 *k*-point mesh. We test our number of *k*-points on a single carbyne chain and compare it to a finer mesh with 16 *k*-points and find a maximum difference in bond length and elastic stiffness is less than 1%. These differences are small enough to give us confidence in our choice of *k*-points to capturing carbyne's mechanical behavior. Visuals in this study are generated using OVITO [40] and the electron density is plotted using VESTA [41].

The Ni block is oriented such that the *x*, *y* and *z* axes correspond to the $[11\bar{2}]$, $[111]$ and $[1\bar{1}0]$ directions respectively. After relaxation the Ni block, which consists of 72 atoms, has dimensions of 8.47 × 11.96 × 7.33 Å in the *x*, *y* and *z* directions respectively. This corresponds to a lattice parameter of around 3.45 Å, which is 3% smaller than the pre-relaxed experimental value of 3.52 Å [42]. When graphene sheets are added to the Ni matrix they are aligned parallel to the Ni (111) plane. Graphene is slightly strained from its perfect lattice by -0.56% and -0.65% in the *x* and *z* directions respectively to match the Ni block dimensions. With these box dimensions a single graphene sheet in a vacuum with periodic boundary conditions experiences no rippling while two stacked sheets each experience rippling amplitude of less than $6x10^{-5}$ Å. This indicates that the compressive strain we apply to graphene in the *x* and *z* directions will not significantly affect its mechanical properties.

In our model we use finite length carbyne chains, each consisting of 5 atoms in a cumulene structure. Carbyne chains with this number of atoms are the strongest predicted by Timoshevskii et al. [14], and have been shown to provide excellent strength while connecting graphene sheets [43]. To ensure that this length of chain will not experience pre-strain due to our tight simulation cell, we perform two separate tests with a single carbyne chain aligned in the *x* direction with a simulation cell the size of our Ni block, and with a much larger simulation cell. After relaxing the chain in both simulations, we find that the chain experiences little to no change in bond length,

structure or orientation. This indicates that a chain of this length will not experience pre-strain from its periodic image in the smaller simulation cell. We use the relaxed chain from the smaller simulation cell as the initial chain introduced when generating nanocomposites. The relaxed bond lengths of the single chain are 1.296 Å for the two outer bonds and 1.286 Å for the two inner bonds.

Our carbyne chains are not capped by hydrogen, allowing us to focus directly on the interactions between carbyne, graphene and Ni without the addition of hydrogen. We test the effect that not using hydrogen will have by preparing a carbyne chain of cumulene structure capped by two hydrogen atoms at each end. After the chain is relaxed we find that the outer C-C bond lengths of the chain with hydrogen is 0.0016 Å longer than the chain without hydrogen while the inner C-C bond is 0.009 Å shorter. These represent a 0.12% increase and a 0.07% decrease in bond lengths respectively. This shows that hydrogen end groups do not affect carbyne's bond structure substantially. We perform tensile tests on the carbyne chain with hydrogen end groups and find that there is only a 0.17% increase in the predicted elastic stiffness of the chain with hydrogen compared to the single chain without hydrogen, which is insignificant. We also note that carbyne has demonstrated stability on a Ni surface without hydrogen [15, 21], and finite-sized carbyne has been shown to be stable without it [14, 43].

To generate nanocomposite samples, we first create a Ni slab by displacing the top half of the Ni block 15 Å upward (in the *y* direction), followed by relaxing in the *x* and *z* directions. Nanocomposite samples are then generated by introducing carbyne and/or graphene in the vacuum region and lowering the slab such that the Ni surface is around 3 Å from the fiber material. The sample is then relaxed in the *y* direction to obtain the final structure.

The final relaxed structures for pure Ni and the Ni-based nanocomposites are shown in Figure 6.2. The atoms are not constrained during relaxation. Note that the carbyne chains in Figure 6.2(c-d) remain straight while the chains present in Figure 6.2(e-f) become kinked with extended bond lengths. The rippling amplitude experienced by the graphene sheets with Ni alone is around 0.002 Å. When one or two carbyne chains are also present, graphene's rippling amplitude increases to around 0.13 Å or 0.08 Å respectively. For convenience, we use a laminate code to denote the nanocomposite structures being modeled, as outlined in Table 6.1. Structures are referenced by their original layup, so the chains shown in Figure 6.2(e-f) will still be referenced as carbyne, though they would more appropriately be called carbon chains, with a possible formation of Ni carbide.

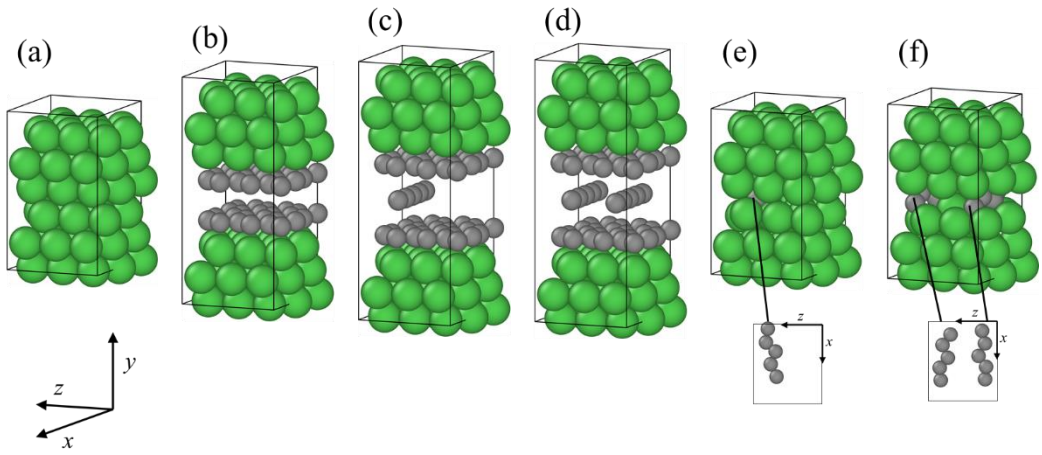

Figure 6.2. Relaxed Ni and Ni-based nanocomposite samples being studied: (a) Ni, (b) $[\mathrm{Ni/gr}]_s$, (c) $[\mathrm{Ni/gr/\bar{c}}]_s$, (d) $[\mathrm{Ni/gr/\overline{2c}}]_s$, (e) $[\mathrm{Ni/\bar{c}}]_s$, (f) $[\mathrm{Ni/\overline{2c}}]_s$. Note that in (e) and (f) the Ni block has enveloped the embedded carbyne chains; insets below the figure show a view of the carbyne chains from above with Ni atoms removed, revealing that the chains have developed kinks.

Table 6.1. Laminate code denoting all nanocomposite structures being modeled. The subscript *s* indicates that the structure's layers are repeated in reverse order, while a bar indicates a layer being in the middle and not repeated.

Laminate Code	**Description of structures and nanocomposites**
c	Single carbyne chain
$2c$	Two carbyne chains
$[\mathrm{gr}]_s$	Two graphene sheets
$[\mathrm{gr}/\bar{c}]_s$	Two graphene sheets enclosing single carbyne chain
$[\mathrm{gr}/\overline{2c}]_s$	Two graphene sheets enclosing two carbyne chains
Ni	Pure Ni
$[\mathrm{Ni}/\mathrm{gr}]_s$	Ni enclosing two graphene sheets
$[\mathrm{Ni}/\mathrm{gr}/\bar{c}]_s$	Ni enclosing two graphene sheets enclosing single carbyne chain
$[\mathrm{Ni}/\mathrm{gr}/\overline{2c}]_s$	Ni enclosing two graphene sheets enclosing two carbyne chains
$[\mathrm{Ni}/\bar{c}]_s$	Ni enclosing single carbyne chain
$[\mathrm{Ni}/\overline{2c}]_s$	Ni enclosing two carbyne chains

In this study, we test the maximum contribution carbyne can make to the local stiffness of a Ni matrix it is embedded within. Tensile loading is simulated by uniformly straining samples in the *x* direction followed by relaxation in the *y* and *z* directions [44-48]. Each sample has a separate simulation performed for each degree of strain, with strain values ranging from 0% to 2% in increments of 0.25%. Cumulene's structure should not change due to strain since our maximum strain well below the predicted strain at which cumulene transitions to polyyne [49]. Since the carbyne chain is of finite-length, and to determine its maximum contribution to loading in the nanocomposite, we fix the free ends of carbyne chains during straining in the *x* direction.

To quantify the local stiffness of our samples along the fiber direction (*x* direction) we find their elastic stiffness C_{11} using the relation

$$C_{11} = \frac{1}{V} \cdot \frac{\partial^2 E_{total}}{\partial \varepsilon^2}, \tag{6.1}$$

where E_{total} is the total energy and V is the sample volume. We fit a second-degree Taylor polynomial to the sample's energy vs. strain curve and take double the coefficient of the quadratic term as $\frac{\partial^2 E_{total}}{\partial \varepsilon^2}$ [45, 46]. To approximate the volume for samples without Ni, each graphene sheet is assumed to have a thickness of 3.35 Å [50], and each carbyne chain is assumed to have a cross section of 3.35 × 3.35 Å [16].

6.3 Results and discussion

We perform tensile tests, as outlined in section 6.2, for all samples described in Table 6.1. The elastic stiffness for each sample is shown in Figure 6.3. We find that a single carbyne chain has 7% higher stiffness than two chains when no other materials are present. This is likely because the single chain has a linear 5-atom carbyne structure; when a second chain is introduced slight distortions caused by the chains interacting disrupts their linear carbyne structure. On the other hand, the two-chain sample with graphene has 13% higher stiffness than the one-chain sample with graphene. In this case the single carbyne chain is already distorted out of its linear chain structure by the presence of graphene sheets; the addition of a second chain does little to increase the distortion, serving only to increase stiffness.

We observe ~70-90% increase in stiffness over pure Ni when graphene with or without carbyne is added to the Ni matrix. It is noteworthy that the $[\mathrm{Ni/gr/\bar{c}}]_s$ sample which includes only a single chain has 3% lower local stiffness than the $[\mathrm{Ni/gr}]_s$ sample where no carbyne is present; this is possibly due to the vacuum region present in the sample containing carbyne. In the $[\mathrm{Ni/gr}]_s$ sample there is a gap between the graphene sheets around 3.0 Å thick. When carbyne is present the gap between graphene sheets is around 5.4 or 5.7 Å thick for 1 or 2 chains respectively. The

open space in this region can be considered as a volume fraction of vacuum, which is a sizable presence in the volume of the nanocomposite, but which does not contribute to its strength. This vacuum volume fraction is diminished in the $[\mathrm{Ni/gr/\overline{2c}}]_s$ sample with the presence of a second chain. We also note that when no graphene is present, carbyne decreases the local stiffness of the Ni matrix by 7-9%.

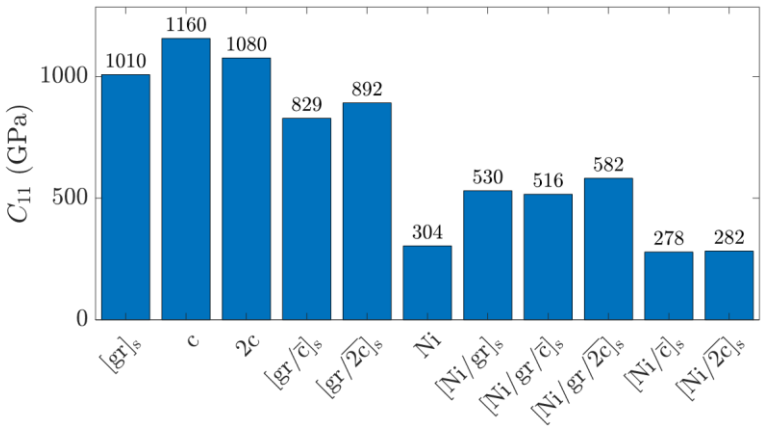

Figure 6.3. Elastic stiffness for graphene, carbyne, Ni and nanocomposites predicted using DFT calculations.

Another way to quantify the local stiffness of samples is by computing their specific stiffness S. Specific stiffness is found by dividing the Young's modulus by its density, or in this case $S = C_{11}/\rho$. Assuming infinitesimal deformations, and by substituting eq. (6.1), this can be converted to

$$S = \frac{1}{m_{total}} \cdot \frac{\partial^2 E_{total}}{\partial \varepsilon^2}, \tag{6.2}$$

where m_{total} is the total mass of all atoms in the sample. Note that specific stiffness is not dependent on volume in our calculations.

The specific stiffness values of the samples in our study are shown in Figure 6.4. The specific stiffness of an ideal carbon nanotube is on the order of $400\ \mathrm{GPa\ cm^3/g}$ [51, 52], which is

near the value we obtain for graphene. We find that the specific stiffness of two graphene sheets is 15% or 7% lower when sandwiching one or two carbyne chains respectively, as shown in Figure 6.4(a). On the other hand, Ni-based nanocomposites with graphene show a 10% or 24% improvement in specific stiffness with one or two carbyne chains respectively, as shown in Figure 6.4(b). While the increase in specific stiffness over pure Ni in the Ni-based nanocomposites with graphene is mostly attributable to the graphene sheets, the inclusion of carbyne chains still provides a noticeable improvement in specific stiffness over graphene-Ni alone. The drop in specific stiffness for carbyne-Ni nanocomposites without graphene present is around 61% or 64% for nanocomposites with one or two chains respectively.

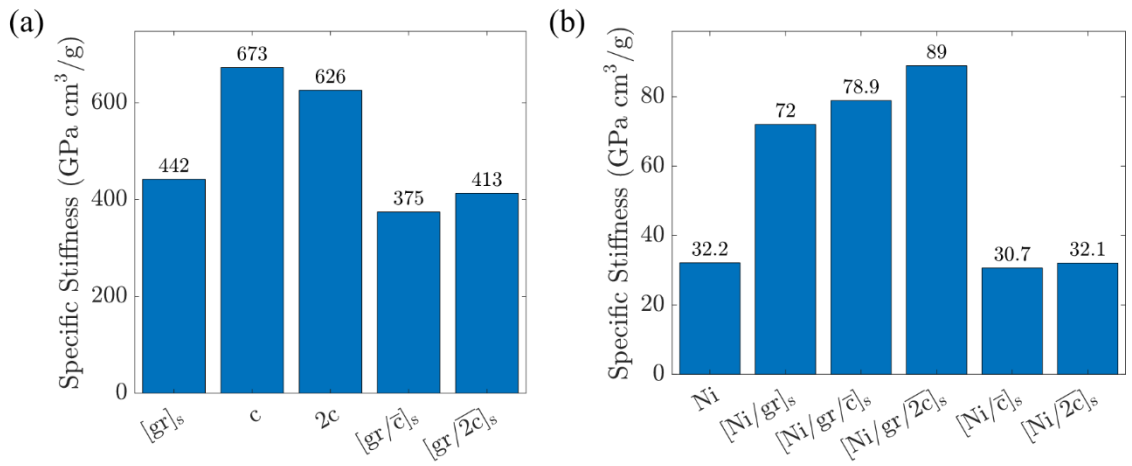

Figure 6.4. Specific stiffness predicted for (a) graphene and carbyne, (b) Ni and Ni-based nanocomposites. Note that the two-chain sample has a lower specific stiffness than the single chain sample, but all nanocomposites with two chains have higher specific stiffness than those with a single chain (though this increase is negligible for $[\mathrm{Ni}/\overline{\mathrm{2c}}]_\mathrm{s}$).

The theoretical value for the specific stiffness of a nanocomposite S_{comp} can be found using the rule of mixtures [53]. In general, this takes the form,

$$S_{\mathrm{comp}} = \sum_i w_i S_i \,, \tag{6.3}$$

where w_i and S_i is the weight fraction and specific stiffness of the i^{th} material respectively. The derivation of eq. (6.3) is included in Appendix B. Our comparison between computed and theoretical specific stiffness is shown in Figure 6.5(a). We observe that the rule of mixtures predicts specific stiffness values higher than those obtained through direct computation, particularly for the $[\text{Ni}/\overline{\text{c}}]_\text{s}$ and $[\text{Ni}/\overline{2\text{c}}]_\text{s}$ samples. However, the relative trends are in good agreement.

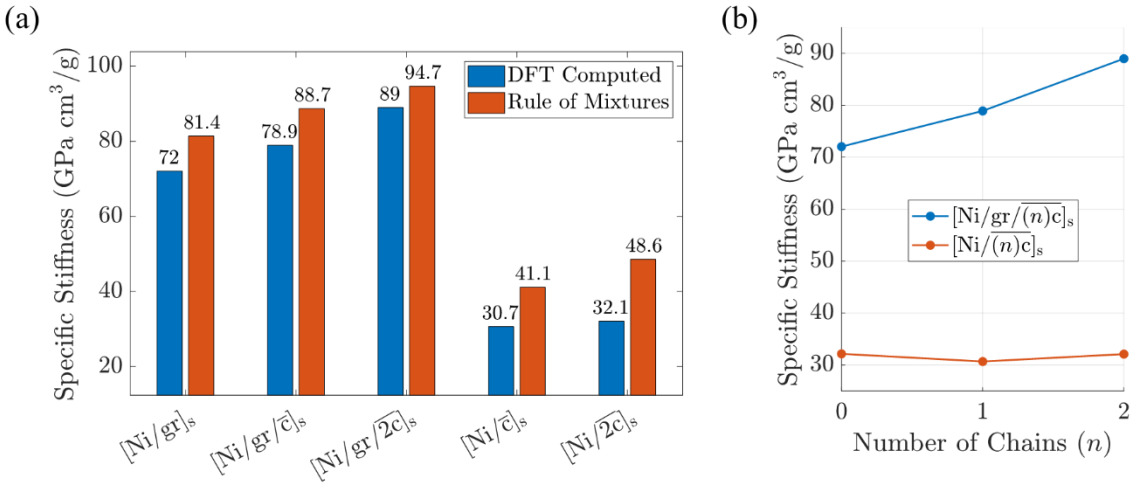

Figure 6.5. (a) Comparison of specific stiffness values for nanocomposites either computed directly with DFT or using the rule of mixtures from eq. (6.3). (b) Specific stiffness vs. number of carbyne chains for Ni-based nanocomposites with or without graphene present. Note that the increase in specific stiffness is linear when graphene is present and is relatively steady otherwise.

We observe that there is a distinct difference in the specific stiffness of carbyne-Ni nanocomposite samples with and without graphene. The change in specific stiffness with 0, 1 or 2 chains are shown in Figure 6.5(b), which shows that carbyne provides a much greater contribution to stiffness when graphene screens it from the Ni surface. It also shows that when graphene is present there is approximately a linear relationship between the number of chains added and the increase in the specific stiffness of the nanocomposite. On the other hand, with samples $[\text{Ni}/\overline{\text{c}}]_\text{s}$ and $[\text{Ni}/\overline{2\text{c}}]_\text{s}$ where no graphene is present there is no improvement in specific stiffness over the pure Ni sample with the addition of carbyne. To understand the reason for this behavior we

compute and visualize the electron density of the single carbyne chain sample, the $[\mathrm{Ni/gr/\overline{c}}]_s$ sample, and the $[\mathrm{Ni/\overline{c}}]_s$ sample, as shown in Figure 6.6. We observe that graphene acts as a dielectric screen for the carbyne chain, such that there is hardly any difference in electron density for the single carbyne chain sample and the $[\mathrm{Ni/gr/\overline{c}}]_s$ sample in the region near the carbyne chain. In contrast, for the $[\mathrm{Ni/\overline{c}}]_s$ sample there is obviously lower electron density between carbon atoms in the chain, with the bonds being lengthened and the chain kinked. This structural change prevents the chain from providing significant contribution to the mechanical performance of $[\mathrm{Ni/\overline{c}}]_s$ and $[\mathrm{Ni/\overline{2c}}]_s$ samples; it would also more correctly be called a carbon chain rather than carbyne because of its change in bond structure.

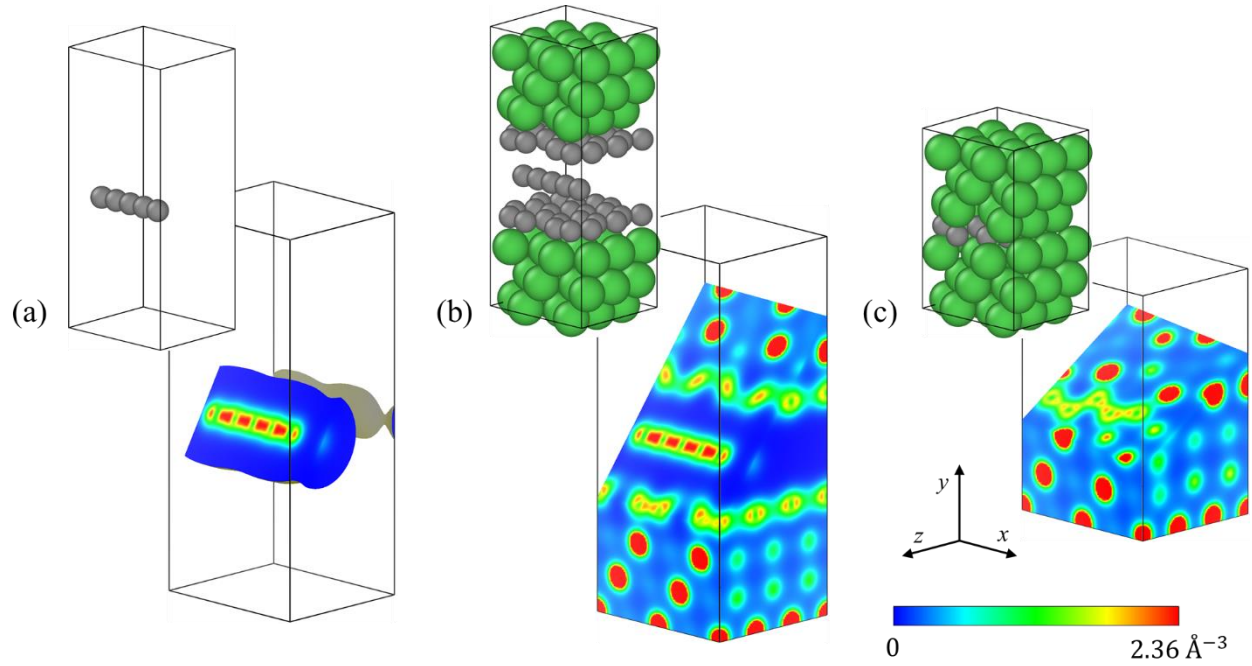

Figure 6.6. Atom positions (upper left corners) and cross-sections of electron density distributions (lower right corners) for (a) single carbyne chain, (b) $[\mathrm{Ni/gr/\overline{c}}]_s$, and (c) $[\mathrm{Ni/\overline{c}}]_s$. Planes for cross-section were chosen to best intersect all atoms in the carbyne chain. Note that the electron density near the carbyne chain is the same for (a) and (b), indicating that graphene effectively screens carbyne from the Ni surface. Note also that the $[\mathrm{Ni/\overline{c}}]_s$ sample has a kinked chain and lower electron density between carbon atoms.

To quantify the charge transferred between the 1D carbyne to the 3D Ni matrix that surrounds it, we use Bader analysis [54-57]. We find that carbyne and graphene have an average of 4.00 valence charge per atom. When carbyne is sandwiched within graphene without Ni present, its valence charge per atom increases to around 4.07, while graphene decreases to around 3.99. This indicates that graphene is donating charge to carbyne, which causes both carbyne and graphene to have lower specific stiffness compared to pure carbyne and graphene, as shown in Figure 6.7(a-b). In its pure form, Ni has a valence charge per atom of 10.00. When either carbyne or graphene is included as a fiber, Ni donates charge to them, as shown in Figure 6.7(c). When graphene is included, this charge donation is accompanied by a significant increase in stiffness compared to pure Ni, while the valence per atom of graphene and carbyne are both increased. When carbyne is included in Ni without graphene present, its valence charge per atom increases substantially to around 4.6. From Figure 6.6(c), we observe that this increased charge in the carbon chain is more spread out rather than focused between the C-C bonds. We note that the average valence charge per atom in Ni is more affected by a single, unprotected, 5-atom carbyne chain than it is by that same chain protected by the 48 carbon atoms present in graphene. This indicates that some Ni carbide has likely formed. We also note that the trend in Figure 6.7(a) shows that an increase in the average valence charge per atom for carbyne leads to a decrease in the specific stiffness of the nanocomposite because of charge distortions in the chain.

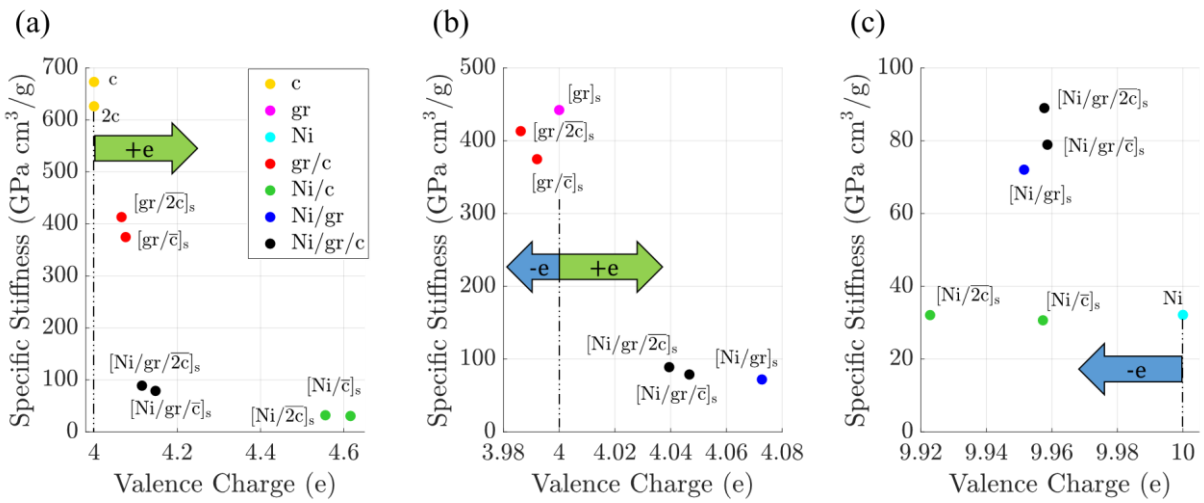

Figure 6.7. Specific stiffness vs. average valence charge per atom for (a) carbyne, (b) graphene, and (c) Ni. The vertical dashed line indicates the valence of the pure sample. Arrows indicate the direction of increasing or decreasing valence charge. This demonstrates the charge being lost or gained when other materials are present. Note that carbyne is always a recipient of donated charge while Ni is always a donor. Graphene is a donor when only carbyne is present, and a recipient otherwise.

6.4 Conclusions

Carbyne is a carbon allotrope possessing excellent mechanical properties and may be an important candidate for use in future nanocomposites as fiber reinforcement. In this first principles study, we find that the local stiffness of a carbyne-Ni nanocomposites under tensile loading is highly dependent on carbyne's charge distribution. When graphene is included as a dielectric screen in carbyne-Ni nanocomposites we find that the charge density between atoms in the carbyne chain remain high and carbyne's valence charge per-atom stays close to its pure form. This allows the carbyne-Ni nanocomposite to have improved local stiffness over pure Ni or graphene-Ni, with the specific stiffness of the carbyne-Ni case increasing linearly with the number of chains. When graphene is not included we find that the charge density between atoms in the chain is reduced and more spread out, and carbon's valence charge per-atom is increased. This causes the nanocomposite to have no improvement in local stiffness over pure Ni, and the carbon chains experience significant kinking.

Our results show that carbyne-metal nanocomposites require dielectric screening for carbyne to effectively improve the mechanical properties of nanocomposites. Nanocomposites with multilayer graphene may derive significant benefit from this as graphene may form carbyne as a secondary structure during yield; the surrounding graphene would provide a built-in screening system, allowing carbyne to further strengthen the nanocomposite. Other materials such as carbon nanotubes could effectively screen chains from metal-matrix charge distortions, though finding ways to ensure that carbyne will contribute to loading will be an ongoing challenge. Utilizing longer carbyne chains may help to promote loading within nanocomposites and allow for better control of chain orientation.

In this research we analyze both elastic and specific stiffness. We find that specific stiffness is an effective way to characterize materials with less than 3 dimensions. When specific stiffness is computed using an energy vs. strain curve, it is not dependent on volume, making it an advantageous measure when analyzing the mechanical properties of modeled 0-D, 1-D and 2-D materials for which volume is an ambiguous property. It is also ideal for analyzing nanocomposite models for which the strength to weight ratio is a commonly desirable measure.

Acknowledgements

We sincerely thank partial support from Center for Advanced Surface Engineering, under the National Science Foundation Grant No. OIA-1457888 and partial support from National Science Foundation Grant No. 1463306 for funding this research. Authors would like to acknowledge the support by Arkansas High Performance Computing Center.

References

[1] A. Hirsch, The era of carbon allotropes, Nature materials 9(11) (2010) 868.

[2] M. Liu, V.I. Artyukhov, H. Lee, F. Xu, B.I. Yakobson, Carbyne from first principles: chain of C atoms, a nanorod or a nanorope, ACS Nano 7(11) (2013) 10075-82.

[3] W.A. Chalifoux, R.R. Tykwinski, Synthesis of polyynes to model the sp-carbon allotrope carbyne, Nat Chem 2(11) (2010) 967-71.

[4] R.R. Tykwinski, W. Chalifoux, S. Eisler, A. Lucotti, M. Tommasini, D. Fazzi, M. Del Zoppo, G. Zerbi, Toward carbyne: Synthesis and stability of really long polyynes, Pure Appl Chem 82(4) (2010) 891-904.

[5] L. Shi, P. Rohringer, K. Suenaga, Y. Niimi, J. Kotakoski, J.C. Meyer, H. Peterlik, M. Wanko, S. Cahangirov, A. Rubio, Confined linear carbon chains as a route to bulk carbyne, Nature materials 15(6) (2016) 634-639.

[6] B. Pan, J. Xiao, J. Li, P. Liu, C. Wang, G. Yang, Carbyne with finite length: The one-dimensional sp carbon, Science advances 1(9) (2015) e1500857.

[7] I.M. Mikhailovskij, E.V. Sadanov, S. Kotrechko, V.A. Ksenofontov, T.I. Mazilova, Measurement of the inherent strength of carbon atomic chains, Phys Rev B 87(4) (2013).

[8] C. Lee, X.D. Wei, J.W. Kysar, J. Hone, Measurement of the elastic properties and intrinsic strength of monolayer graphene, Science 321 (2008) 385-388.

[9] A. Nair, S. Cranford, M. Buehler, Erratum: The minimal nanowire: Mechanical properties of carbyne, EPL (Europhysics Letters) 106(3) (2014) 39901.

[10] S.P. Rawal, Metal-matrix composites for space applications, Jom 53(4) (2001) 14-17.

[11] Z. Salman, A. Nair, S. Tung, One-dimensional carbon chains as electrical sensors for single-stranded DNA, Nano/Micro Engineered and Molecular Systems (NEMS), 2017 IEEE 12th International Conference on, IEEE, 2017, pp. 677-681.

[12] X. Liu, G. Zhang, Y.-W. Zhang, Tunable mechanical and thermal properties of one-dimensional carbyne chain: Phase transition and microscopic dynamics, The Journal of Physical Chemistry C 119(42) (2015) 24156-24164.

[13] M. Kertesz, J. Koller, A. A? man, A binitio Hartree–Fock crystal orbital studies. II. Energy bands of an infinite carbon chain, The Journal of Chemical Physics 68(6) (1978) 2779-2782.

[14] A. Timoshevskii, S. Kotrechko, Y. Matviychuk, Atomic structure and mechanical properties of carbyne, Phys Rev B 91(24) (2015).

[15] Q. Yuan, F. Ding, Formation of carbyne and graphyne on transition metal surfaces, Nanoscale 6(21) (2014) 12727-12731.

[16] A.K. Nair, S.W. Cranford, M.J. Buehler, The minimal nanowire: Mechanical properties of carbyne, Epl 95(1) (2011).

[17] R.H. Baughman, Dangerously seeking linear carbon, Science 312(5776) (2006) 1009-1110.

[18] R.R. Tykwinski, Carbyne: the molecular approach, The Chemical Record 15(6) (2015) 1060-1074.

[19] P. Tarakeshwar, P.R. Buseck, H.W. Kroto, Pseudocarbynes: charge-stabilized carbon chains, The journal of physical chemistry letters 7(9) (2016) 1675-1681.

[20] E. Buntov, A. Zatsepin, M. Guseva, Y.S. Ponosov, 2D-ordered kinked carbyne chains: DFT modeling and Raman characterization, Carbon 117 (2017) 271-278.

[21] T. Pavlova, S. Kovalenko, K. Eltsov, Carbon chains and graphene nucleus synthesized on Ni (111) surface, arXiv preprint arXiv:1712.05313 (2017).

[22] J. Gao, Q. Yuan, H. Hu, J. Zhao, F. Ding, Formation of carbon clusters in the initial stage of chemical vapor deposition graphene growth on Ni (111) surface, The Journal of Physical Chemistry C 115(36) (2011) 17695-17703.

[23] D. Boukhvalov, I. Zhidkov, E. Kurmaev, E. Fazio, S. Cholakh, L. D'Urso, Atomic and electronic structures of stable linear carbon chains on Ag-nanoparticles, Carbon 128 (2018) 296-301.

[24] X. Zhao, Y. Ando, Y. Liu, M. Jinno, T. Suzuki, Carbon nanowire made of a long linear carbon chain inserted inside a multiwalled carbon nanotube, Phys Rev Lett 90(18) (2003) 187401.

[25] C. Zhao, R. Kitaura, H. Hara, S. Irle, H. Shinohara, Growth of linear carbon chains inside thin double-wall carbon nanotubes, The Journal of Physical Chemistry C 115(27) (2011) 13166-13170.

[26] E. Ganz, A.B. Ganz, L.-M. Yang, M. Dornfeld, Carbon nanotube-carbyne composite: A nanoreactor in a quasi-1D liquid state, Computational Materials Science 149 (2018) 409-415.

[27] L. Moura, C. Fantini, A. Righi, C. Zhao, H. Shinohara, M. Pimenta, Dielectric screening in polyynes encapsulated inside double-wall carbon nanotubes, Phys Rev B 83(24) (2011) 245427.

[28] B. Yang, S. Wang, Y. Guo, J. Yuan, Y. Si, S. Zhang, H. Chen, Strength and failure behavior of a graphene sheet containing bi-grain-boundaries, RSC Advances 4(97) (2014) 54677-54683.

[29] S. Wang, B. Yang, J. Yuan, Y. Si, H. Chen, Large-scale molecular simulations on the mechanical response and failure behavior of a defective graphene: cases of 5–8–5 defects, Scientific reports 5 (2015) 14957.

[30] S.E. Muller, R.R. Santhapuram, A.K. Nair, Failure mechanisms in pre-cracked Ni-graphene nanocomposites, Computational Materials Science 152 (2018) 341-350.

[31] M.L. Aubrey, B.M. Wiers, S.C. Andrews, T. Sakurai, S.E. Reyes-Lillo, S.M. Hamed, C.-J. Yu, L.E. Darago, J.A. Mason, J.-O. Baeg, Electron delocalization and charge mobility as a function of reduction in a metal–organic framework, Nature materials (2018) 1.

[32] J. Zhao, Y. Zhang, Y. Fang, Z. Fan, G. Ma, Y. Liu, X. Zhao, Synthesis of polyynes by intense femtosecond laser irradiation of SWCNTs suspended in methanol, Chemical Physics Letters 682 (2017) 96-100.

[33] D. Wendinger, R.R. Tykwinski, Odd [n] Cumulenes (n= 3, 5, 7, 9): synthesis, characterization, and reactivity, Accounts of chemical research 50(6) (2017) 1468-1479.

[34] D. Cheng, G. Barcaro, J.-C. Charlier, M. Hou, A. Fortunelli, Homogeneous nucleation of graphitic nanostructures from carbon chains on Ni (111), The Journal of Physical Chemistry C 115(21) (2011) 10537-10543.

[35] J. Gao, J. Yip, J. Zhao, B.I. Yakobson, F. Ding, Graphene nucleation on transition metal surface: structure transformation and role of the metal step edge, Journal of the American Chemical Society 133(13) (2011) 5009-5015.

[36] P. Giannozzi, S. Baroni, N. Bonini, M. Calandra, R. Car, C. Cavazzoni, D. Ceresoli, G.L. Chiarotti, M. Cococcioni, I. Dabo, QUANTUM ESPRESSO: a modular and open-source software project for quantum simulations of materials, Journal of physics: Condensed matter 21(39) (2009) 395502.

[37] J.P. Perdew, K. Burke, M. Ernzerhof, Generalized gradient approximation made simple, Phys Rev Lett 77(18) (1996) 3865.

[38] P.E. Blöchl, Projector augmented-wave method, Phys Rev B 50(24) (1994) 17953.

[39] S. Grimme, Semiempirical GGA-type density functional constructed with a long-range dispersion correction, Journal of computational chemistry 27(15) (2006) 1787-1799.

[40] A. Stukowski, Visualization and analysis of atomistic simulation data with OVITO-the Open Visualization Tool, Model Simul Mater Sc 18(1) (2010).

[41] K. Momma, F. Izumi, VESTA: a three-dimensional visualization system for electronic and structural analysis, Journal of Applied Crystallography 41(3) (2008) 653-658.

[42] D. Connétable, É. Andrieu, D. Monceau, First-principles nickel database: Energetics of impurities and defects, Computational Materials Science 101 (2015) 77-87.

[43] A. Timoshevskii, S. Kotrechko, Y. Matviychuk, Ab-initio design of 3D carbyne-based material, Computational Materials Science 128 (2017) 223-228.

[44] L. Yue-Lin, Z. Ying, H. Rong-Jie, L. Guang-Hong, Study of the theoretical tensile strength of Fe by a first-principles computational tensile test, Chinese Physics B 18(5) (2009) 1923.

[45] E. Menendez-Proupin, S. Cervantes-Rodríguez, R. Osorio-Pulgar, M. Franco-Cisterna, H. Camacho-Montes, M. Fuentes, Computer simulation of elastic constants of hydroxyapatite and fluorapatite, Journal of the mechanical behavior of biomedical materials 4(7) (2011) 1011-1020.

[46] S.S. Bhat, U.V. Waghmare, U. Ramamurty, First-principles study of structure, vibrational, and elastic properties of stoichiometric and calcium-deficient hydroxyapatite, Crystal Growth & Design 14(6) (2014) 3131-3141.

[47] G.-H. Lu, S. Deng, T. Wang, M. Kohyama, R. Yamamoto, Theoretical tensile strength of an Al grain boundary, Phys Rev B 69(13) (2004) 134106.

[48] H. Sun, S. Mukherjee, M. Daly, A. Krishnan, M.H. Karigerasi, C.V. Singh, New insights into the structure-nonlinear mechanical property relations for graphene allotropes, Carbon 110 (2016) 443-457.

[49] G. Chechin, D. Sizintsev, O. Usoltsev, Nonlinear atomic vibrations and structural phase transitions in strained carbon chains, Computational Materials Science 138 (2017) 353-367.

[50] S. Cranford, D. Sen, M.J. Buehler, Meso-origami: folding multilayer graphene sheets, Applied physics letters 95(12) (2009) 123121.

[51] F.A. Hill, T.F. Havel, A.J. Hart, C. Livermore, Characterizing the failure processes that limit the storage of energy in carbon nanotube springs under tension, Journal of Micromechanics and Microengineering 20(10) (2010) 104012.

[52] K. Koziol, J. Vilatela, A. Moisala, M. Motta, P. Cunniff, M. Sennett, A. Windle, High-performance carbon nanotube fiber, Science 318(5858) (2007) 1892-1895.

[53] A.K. Kaw, Mechanics of composite materials, CRC press2005.

[54] G. Henkelman, A. Arnaldsson, H. Jónsson, A fast and robust algorithm for Bader decomposition of charge density, Computational Materials Science 36(3) (2006) 354-360.

[55] E. Sanville, S.D. Kenny, R. Smith, G. Henkelman, Improved grid-based algorithm for Bader charge allocation, Journal of computational chemistry 28(5) (2007) 899-908.

[56] W. Tang, E. Sanville, G. Henkelman, A grid-based Bader analysis algorithm without lattice bias, Journal of Physics: Condensed Matter 21(8) (2009) 084204.

[57] M. Yu, D.R. Trinkle, Accurate and efficient algorithm for Bader charge integration, The Journal of chemical physics 134(6) (2011) 064111.

Chapter 7

Paper 4: Deformation mechanisms of Al/amorphous-Si core-shell nanorods

Abstract

In this study, we model the indentation/retraction of an aluminum/amorphous-Si (Al/a-Si) core-shell nanorod. We investigate changes in the deformation behavior of the core-shell structure with changes in the size of the core and shell. Since indentation has nonlinear material behavior around the point of contact, and the linear elastic region can span long range, we use a multiscale model as implemented in the coupled atomistic and discrete dislocation (CADD) method. We introduce a two-material/phase formulation of the CADD method to model the FCC Al and a-Si phases. Under indentation and retraction loading, samples with shell show an average 9% greater recovery in core height than samples with no shell. We find that there are three routes for deformation in the core-shell structure: (1) compression of the Al core, (2) deflection of the surrounding Al substrate, (3) deformation of the a-Si shell. When present, the a-Si shell delocalizes forces generated by the indenter, allowing for all three forms of deformation to be active. This allows the Al core, the a-Si shell, and the surrounding Al substrate to each contribute to the indentation load and increases the force necessary to produce yield in the core. Without the shell, compression of the core is the dominant form of deformation, with yield occurring at lower indentation force than samples with shell. We also find that the dominance of deformation in the core or substrate is dependent on the size of core used. Samples with large cores and thin shells experience deformation mostly in the core. On the other hand, shelled samples with small cores and thick shells have well-protected cores and experience substantial deformation in the substrate. This work

will help with the design of low friction nanotextured surfaces composed of core-shell nanorods tailored for specific deformation characteristics.

7.1 Introduction

The tribological properties of nanotextured contact surfaces have many advantages over smooth contact surfaces including a reduction in friction and adhesion [1-5]. However, because of their high surface-to-volume ratio, nanotextured surfaces have a strong tendency toward plastic deformation [6, 7]. Designing nanotexture surfaces that are resistant to deformation is important for many micro and nanoscale systems. Tidwell et al. designed aluminum/amorphous-silicon (Al/a-Si) core-shell nanostructures which are resistant to deformation under indentation [8]. Fleming et al. showed that these nanostructure also experience a surprising level of recovery after indentation and retraction [9, 10]. They found this effect most pronounced in nanostructures with smallest core volume and a hemispherical structure, as shown in Figure 7.1(a). But this effect was also observed in core-shell nanorods, as shown in Figure 7.1(b-d). Several possible mechanisms were theorized to explain this behavior, including dislocation absorption by the Al/a-Si interface and annihilation through reactions with other dislocations, both of which they observed using molecular dynamics (MD) models of their samples. Other factors that may influence deformation and recovery in core-shell nanostructures/nanorods include core and shell size. It would be useful to consider the way these parameters influence deformation and recovery in the core, shell and substrate separately, though this is challenging to do experimentally. Nanostructures/nanorods may also be investigated at higher length scales than those used by Fleming et al. to determine how these structures behave at lengths beyond the reach of pure MD.

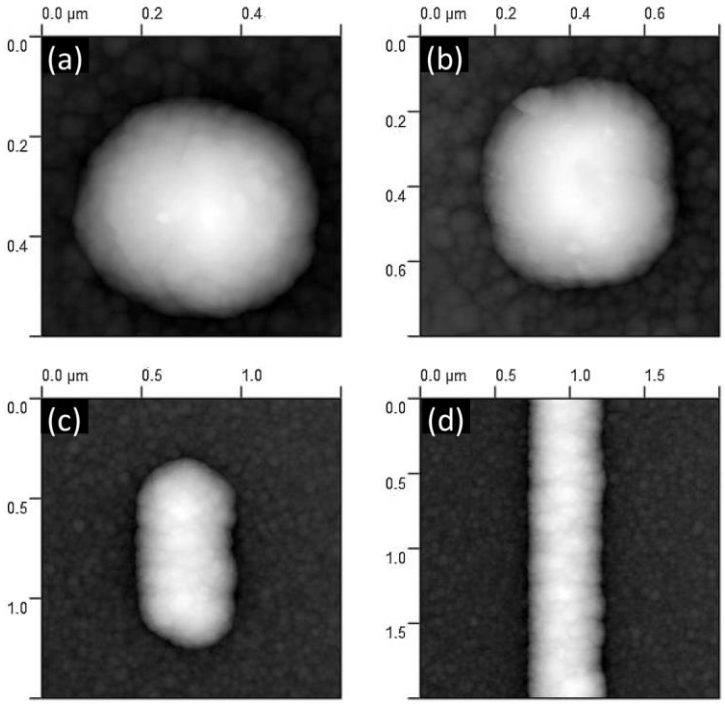

Figure 7.1 Atomic force microscopy images of a hemispherical core-shell nanostructure (a), and core-shell nanorods with core lengths of 100 nm (b), 500 nm (c), and 10 µm (d). Reprinted from Fleming et al., with permission from Elsevier [9].

Computationally modeling metals and metal-based nanocomposites beyond the atomistic scale presents a challenge. Continuum models for macroscale behavior may fail to capture unique behaviors that nanoscale metals are known to exhibit. These behaviors includes dislocation starving [11, 12], multilayer laminates [13], and unique deformation mechanisms [14], all of which can have significant impact on macroscale mechanical properties. On the other hand, atomistic models have a limited length scale that may fail to predict macroscale behavior. Multiscale methods can bridge the gap between length scales and explore how nonlinear effects translate into long range behavior. One multiscale method that is ideal for many metallic systems is the coupled atomistic and discrete dislocation (CADD) method which connects an atomistic system to a discrete dislocation framework [15]. This method was designed to allow dislocations generated in the atomistic region to be transmitted to the continuum, and has been shown to be among the most accurate and efficient methods of its kind [16].

In this work we use the CADD multiscale method to further explore the deformation of Al/a-Si core-shell nanorods under indentation and retraction. We vary the Al-core radius and a-Si shell thickness and determine the effect that core-shell structure has on indentation force, deformation of core/shell/substrate at first yield, and recovery. In our implementation of CADD, we select an atomistic region such that free surface effects will not influence bulk atom properties. Previous studies using CADD were designed to model one material/phase; here we modify CADD to simultaneously model both FCC Al and Si in an amorphous phase. The inclusion of a second amorphous material presents challenges to the CADD algorithm due to the required crystallinity of pad atoms, the formulation of the continuum's free energy functional, and high forces at the Al/a-Si interface. We show our process for modifying the CADD algorithm to address these issues, which improves its adaptability and allows it to model our materials of interest.

7.2 Methods

7.2.1 Layup of Al/a-Si core-shell nanorods and CADD implementation

The material phases we implement are FCC Al (core) and a-Si (shell) in a nanorod structure, as shown schematically in Figure 7.2. The core is composed of a semicylindrical Al asperity on top of an Al substrate, with both asperity and substrate being a single Al crystal. The shell consists of a-Si deposited on both the Al asperity and the upper surface of the Al substrate. Our model is structurally similar to the experimental layup shown in Figure 7.1(d) [9], but with Al instead of Si being used as the substrate. This allows us to explore substrate effects, which were not considered in previous studies by Fleming et al. who used a rigid substrate in their MD simulations [9, 10]. The *x*, *y* and *z* axes in our simulation refer to the lattice vectors $[11\bar{2}]$, $[111]$ and $[1\bar{1}0]$ respectively. Simulations are periodic in the *z* direction, which reflects our nanorod

geometry. This also allows for single-crystal Al to be modeled with two Al layers in the *z* direction, with a thickness of 0.285 nm in that direction. Indentation and retraction is performed on our samples using a cylindrical repulsive indenter with a diameter of 200 nm.

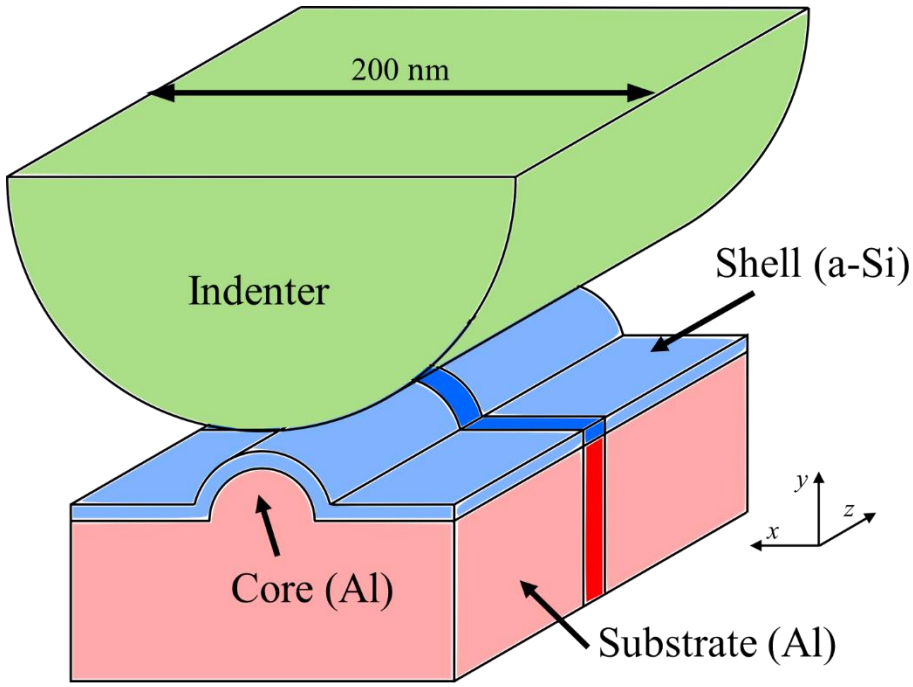

Figure 7.2. Schematic of Al/a-Si core-shell nanorod being tested with a repulsive indenter. The bolder colored regions in the core-shell structure represent the model being developed while the lighter colored region shows the larger system we are modeling due to our periodic boundaries.

In this work we use the CADD method as implemented previously [17-19], consisting of an atomistic region coupled to a continuum region. Atomistic-continuum multiscale methods are defined by the interaction between their atomistic and continuum regions. In the CADD method, the atomistic and continuum regions interact by separately controlling the movement of atoms/nodes at their interface, which serve as Dirichlet boundary conditions for the other region. The atomistic region controls the movement of "interface" atoms, which are fixed from the continuum's perspective. The continuum region in turn controls the movement of "pad" atoms, which are frozen in the atomistic region.

The continuum region, shown in Figure 7.3(a), is a finite element mesh governed by a discrete dislocation framework [20]. The continuum region acts as that part of the substrate in the linear elastic regime that is far-distant from the nonlinear material behavior produced by indentation. Our continuum region is 2 μm wide by 1 μm tall, dimensions that are on the order of those used by Fleming et al. [9, 10] and Steck et al. [21] for their experimental substrate about their indentation impression. Such dimensions are generally beyond the reach of atomistic models alone. The mesh of the continuum region has increasing fineness close to the atomistic region, as shown in Figure 7.3(b). Our atomistic region, shown in Figure 7.3(c), is 150 nm wide and has a substrate height that varies with shell thickness, but the height of the Al substrate is always 20 nm. The dimensions of our atomistic region are chosen to ensure that deformations produced through indentation remain minimal near pad atoms. The pad region in our model, shown in Figure 7.3(d), has a thickness of 1.5 nm, three times greater than the 0.5 nm interaction cutoff radius used in our MD model. This prevents interior atoms from detecting the free surface at the edges of the atomistic region. With these dimensions, we find that the maximum deflection in our pad for samples with the greatest substrate deflection is less than 0.5 nm in the *y* direction, which is less than 2.5% the size of the Al part of the substrate. Through parametric studies we find that nonlinear effects from the atomistic region have minimal effect on the continuum region with the chosen dimensions. The samples in our study vary based on the parameters core radius (R) and shell thickness (t_0). We vary R between 6.25 nm, 12.5 nm, 25 nm, and 50 nm; we vary t_0 between 0 (no shell), 6.25 nm, and 12.5 nm.

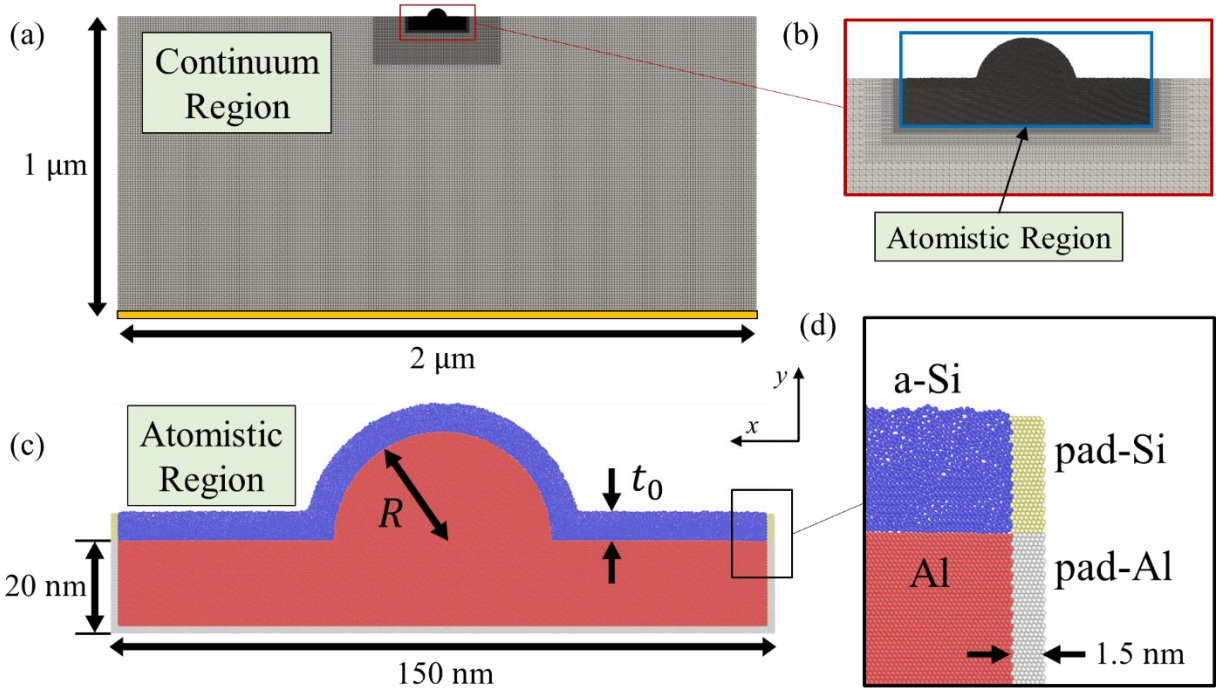

Figure 7.3. (a) Continuum region consisting of a finite element mesh with a discrete dislocation framework. The fixed boundary at the bottom is shown as an orange bar. (b) Zoomed-in view of continuum region at and near the atomistic region, which is boxed in blue. (c) Atomistic region with Al atoms colored red, a-Si atoms colored blue, pad-Al atoms colored white and pad-Si atoms colored yellow. Note that core radius R and shell thickness t_0 vary with each sample. (d) Zoomed-in view of atomistic region, showing the different atom types being used. Specified dimensions are consistent for all samples. Continuum visuals are generated using ParaView [22] while atomistic visuals are generated using OVITO [23].

During simulations there is systematic transfer of information between the continuum region and the atomistic region, detailed in section 2.3. Bulk atoms that are adjacent to pad atoms in the atomistic region are interface atoms, which serve as a fixed boundary condition for the continuum region. The continuum region also has fixed boundary conditions for nodes at its base, as shown in Figure 7.3(a). The continuum region provides boundary conditions for the atomistic region through the movement of pad nodes, which correspond to pad atoms in the atomistic region. To ensure that the pad nodes in the continuum remain well-ordered, we keep all pad atoms in an FCC-Al structure, including pad-Si atoms. Because the forces on pad atoms in the atomistic region is always zero, the instability of pad-Si atoms in the FCC-Al structure only affects a-Si atoms

neighboring the pad region. Any instability affecting a-Si atoms at the a-Si/pad-Si interface is generally contained at that interface due to the immobility of defects in the amorphous structure.

A key feature of CADD is its method for detecting and passing discrete dislocations from the atomistic region to the continuum region [15, 17, 18]. This is accomplished using a detection band near the pad region that identifies dislocations that pass through it. A detected dislocation is annihilated within the atomistic region by shifting pad atoms to accommodate the slip produced by the dislocation. A discrete dislocation is then generated in the continuum region, with behavior dependent on discrete dislocation dynamics.

7.2.2 Theoretical justification for two-material CADD formulation in continuum region

To theoretically justify our use of a second material in the continuum region for CADD, we must alter its formulation at the element level. We first consider the free energy functional of CADD's continuum region as outlined by Shilkrot et al. [17]:

$$E^c = \frac{1}{2}\int_{\Omega_C} (\widehat{\boldsymbol{\sigma}} + \widetilde{\boldsymbol{\sigma}}) : (\widehat{\boldsymbol{\varepsilon}} + \widetilde{\boldsymbol{\varepsilon}}) dV - \int_{\partial\Omega_T} \boldsymbol{T}_0 (\widetilde{\boldsymbol{u}} + \widehat{\boldsymbol{u}}) dA \ . \tag{7.1}$$

The energy is a superposition of a linear elastic body (^) and discrete dislocations in a homogeneous elastic material (~), subject to traction $\boldsymbol{T}_0$. One of the materials in our model is amorphous, meaning that we need only consider discrete dislocations in the non-amorphous material. This confines the required changes in CADD's formulation to the linear elastic body and allows the discrete dislocation field terms (containing $\widetilde{\boldsymbol{\sigma}}$, $\widetilde{\boldsymbol{\varepsilon}}$) to require no modification. Changing CADD's formulation to accommodate discrete dislocations in more than one material is a challenge for future work.

The strain energy of the linear elastic body, which we will denote W, is part of the free energy functional; it has the form [17]

$$W = \frac{1}{2}\int_{\Omega_C} \hat{\boldsymbol{\sigma}} : \hat{\boldsymbol{\varepsilon}}\, dV = \frac{1}{2}(\hat{\boldsymbol{u}}_C^T \boldsymbol{C}_{CC} \hat{\boldsymbol{u}}_C + \hat{\boldsymbol{u}}_I^T \boldsymbol{C}_{II} \hat{\boldsymbol{u}}_I) + \hat{\boldsymbol{u}}_C^T \boldsymbol{C}_{CI} \hat{\boldsymbol{u}}_I \ , \tag{7.2}$$

where $\boldsymbol{C}_{CC}$, $\boldsymbol{C}_{II}$ and $\boldsymbol{C}_{CI}$ are FEM stiffness matrices coupling continuum nodal displacements ($\hat{\boldsymbol{u}}_C$) and interface nodal displacements ($\hat{\boldsymbol{u}}_I$). The subscripts CC, II and CI refer to continuum-continuum, interface-interface and continuum-interface nodal coupling respectively. If all nodal displacements in the linear elastic body are contained in a single concatenated vector $\hat{\boldsymbol{u}} = \hat{\boldsymbol{u}}_C \| \hat{\boldsymbol{u}}_I$, then the strain energy can be written as

$$W = \frac{1}{2}\hat{\boldsymbol{u}}^T \begin{bmatrix} \boldsymbol{C}_{CC} & 2\boldsymbol{C}_{CI} \\ \boldsymbol{0} & \boldsymbol{C}_{II} \end{bmatrix} \hat{\boldsymbol{u}} = \frac{1}{2}\hat{\boldsymbol{u}}^T \boldsymbol{C}\, \hat{\boldsymbol{u}} \ , \tag{7.3}$$

where $\boldsymbol{C}$ is the global stiffness matrix combining all element stiffness matrices. We now consider the strain energy of the i^{th} element of a linear elastic body [24], found by

$$W_i = \frac{1}{2}\hat{\boldsymbol{u}}_i^T \boldsymbol{K}_i^{\mu_i} \hat{\boldsymbol{u}}_i \ , \tag{7.4}$$

where $\hat{\boldsymbol{u}}_i$ is a vector that contains the nodal displacements for each node in the element and $\boldsymbol{K}_i^{\mu_i}$ is the element's stiffness matrix, with the element being composed of material μ_i. The stiffness matrix of element i is found by

$$\boldsymbol{K}_i^{\mu_i} = a_i \boldsymbol{B}_i^T \boldsymbol{D}^{\mu_i} \boldsymbol{B}_i \ , \tag{7.5}$$

where a_i is the scalar area of the element, $\boldsymbol{D}^{\mu_i}$ is a matrix determined by the elastic properties of material μ_i, and $\boldsymbol{B}_i$ is a matrix of spatial derivatives of shape functions such that the element strain is $\hat{\boldsymbol{\varepsilon}}_i = \boldsymbol{B}_i \hat{\boldsymbol{u}}_i$. The total strain energy of all elements can be found by

$$W = \sum_i W_i = \frac{1}{2}\sum_i \hat{\boldsymbol{u}}_i^T \boldsymbol{K}_i^{\mu_i} \hat{\boldsymbol{u}}_i \ . \tag{7.6}$$

To incorporate two materials into our CADD model we will assume there are a total of n elements, and that the first m elements are Al while the latter $n-m$ elements are Si. In this case, the total strain energy can be written as

$$W = \frac{1}{2}\left[\sum_{i=1}^{n-m} \hat{\boldsymbol{u}}_i^T \boldsymbol{K}_i^{\mathrm{Al}} \hat{\boldsymbol{u}}_i + \sum_{i=n-m+1}^{n} \hat{\boldsymbol{u}}_i^T \boldsymbol{K}_i^{\mathrm{Si}} \hat{\boldsymbol{u}}_i\right] . \tag{7.7}$$

This can be further expanded by substituting in eq. (7.5)

$$W = \frac{1}{2}\left[\sum_{i=1}^{n-m} a_i \hat{\boldsymbol{u}}_i^T \boldsymbol{B}_i^T \boldsymbol{D}^{\mathrm{Al}} \boldsymbol{B}_i \hat{\boldsymbol{u}}_i + \sum_{i=n-m+1}^{n} a_i \hat{\boldsymbol{u}}_i^T \boldsymbol{B}_i^T \boldsymbol{D}^{\mathrm{Si}} \boldsymbol{B}_i \hat{\boldsymbol{u}}_i\right] . \tag{7.8}$$

We note that each element stiffness matrix may be different, but all Al elements have the same $\boldsymbol{D}^{\mathrm{Al}}$, and all Si elements have the same $\boldsymbol{D}^{\mathrm{Si}}$. We can contain all nodal displacements into a single vector $\hat{\boldsymbol{u}}$ by constructing a global stiffness matrix $\boldsymbol{C}$ such that $W = \frac{1}{2}\hat{\boldsymbol{u}}^T \boldsymbol{C}\, \hat{\boldsymbol{u}}$. The global stiffness matrix stores all the material properties for both Al and Si elements, and we have the same form as that developed for CADD in eq. (7.3). Thus our two materials can be incorporated in CADD's continuum region. Elastic constants for the element stiffness matrices used for Al and a-Si in the continuum are obtained by MD simulations using the same potential used for atoms in the atomistic region, as described in section 2.3. This gives us continuity in our elastic properties going from the atomistic region to the continuum region.

7.2.3 Simulation specifics for two-material CADD formulation

The atomistic region of CADD is simulated by molecular dynamics using the Large-scale Atomic/Molecular Massively Parallel Simulator (LAMMPS) [25], which has previously been

implemented with CADD by Pavia and Curtin [26]. Interactions in the atomistic region are governed by the modified embedded-atom method (MEAM) [27], with potentials developed by Jelinek et al. for modeling a variety of alloys including Al and Si [28]. Energy minimization in our simulation is performed using the conjugate gradient method. We generate the a-Si shell in our model by first heating and relaxing the non-pad-Si to 1500 K for 0.5 ps with an NVT ensemble. The underlying Al atoms and pad-Si atoms in the atomistic region are held fixed during this process, ensuring that atom vibrations from heated non-pad-Si will not affect the atomistic-continuum interface. This is followed immediately by energy minimization and relaxation of non-pad-Si at 1 K for 2.5 ps while still holding all other atoms fixed. At this point an a-Si shell is generated. To minimize forces at the Al/a-Si interface we perform energy minimization and relax all non-pad Al and a-Si atoms at 1 K for 5 ps. The process of generating a-Si takes place entirely in the atomistic region with no activity in the continuum region.

The equilibrium elastic moduli used in the continuum region are found using molecular statics, run separately for Al and a-Si blocks, with loading in different directions. We use the same MEAM potential as that used in the atomistic region. For the Al part of the continuum model, the equilibrium elastic moduli we use are $C_{11} = C_{22} = C_{33} =$ 110.5 GPa, $C_{12} = C_{13} = C_{23} =$ 60.9 GPa, and $C_{44} = C_{55} = C_{66} =$ 28.4 GPa, less than 3% different from values obtained experimentally and in good agreement with other MD potentials [29]. For the a-Si part of the continuum, the equilibrium elastic moduli we use are $C_{11} = C_{22} = C_{33} =$ 124.7 GPa, $C_{12} = C_{13} = C_{23} =$ 63.0 GPa, and $C_{44} = C_{55} = C_{66} =$ 30.8 GPa, around 10% less than values obtained for a-Si using a reactive empirical bond-order potential [30].

Indentation and retraction is performed on each sample, with the indenter interacting directly with atoms in the atomistic region. The continuum region is affected by the indenter only

indirectly based on the forces experienced by atoms in the atomistic region and dislocations detected near the atomistic-continuum interface. We use a repulsive cylindrical indenter with a diameter of 200 nm, as shown schematically in Figure 7.2, with a force constant of 1602 nN/nm^2. Indentation is performed quasi-statically by shifting the indenter 0.1 nm per cycle. At each indentation cycle the atomistic region approaches an equilibrium state for all non-pad atoms by performing the following process one or more times: (1) energy minimization, (2) relaxation at 1 K for 1 ps with an NVT ensemble, (3) energy minimization. The NVT ensemble helps minimize the a-Si region that contains a few atoms with high forces.

CADD is a force-based method, meaning that equilibration of the system occurs as forces in the system approach zero. Our criteria for an equilibrated state is that the maximum force possessed by Al atoms in the core and substrate of the atomistic region is less than 0.008 eV/Å. We observe that while the a-Si region approaches equilibrium, its inherently disordered structure means that a few a-Si atoms scattered throughout the shell will retain relatively high forces, however, through parametric studies we find that these atoms won't affect the dislocation nucleation force or deformation mechanisms. When an equilibrated state is reached in the atomistic region, the continuum region equilibrates using the conjugate gradient method while applying all its boundary conditions, including those imposed by interface atoms. During this step the continuum moves continuum dislocations and pad nodes corresponding to pad atoms in the atomistic region. We simulate indentation on each sample until a dislocation is present in the Al core or substrate. After the point of dislocation nucleation, we begin quasi-static retraction of the indenter at the same rate of 0.1 nm per cycle. This is continued until all forces on the indenter reach zero.

7.3 Results and discussion

7.3.1 Parameters used in core shell analysis

The indentation depths at which the first dislocation is nucleated range from 1.2 -7 nm. The average indentation depth at which a dislocation nucleates is 2.6, 4.2 and 5.7 nm for samples with shell thicknesses of 0, 6.25 and 12.5 nm respectively. During indentation and retraction, we keep track of force on the indenter in the *y* direction (F_y), as well as several spatial parameters, shown in Figure 7.4, that are used in later analysis including: the change in core height (Δh), the deformation of the substrate relative to the initial flat substrate (Δs), and the approximate change in shell thickness in that part of the shell directly above the asperity and beneath the indenter (Δt). These spatial parameters allow us to better understand the deformation of the core and the extent to which the shell protects the core during indentation than other spatial parameters such as indentation depth.

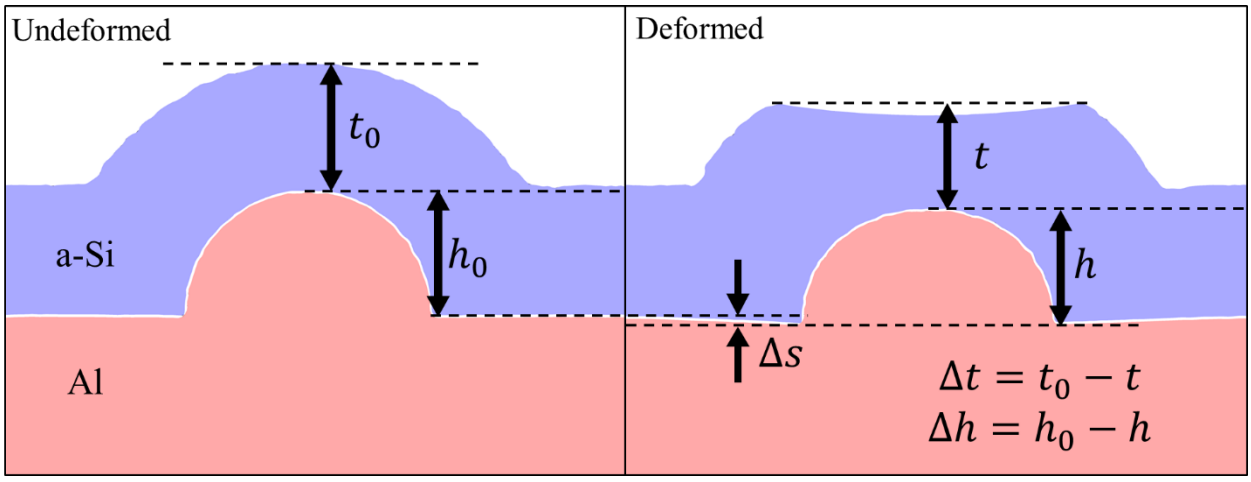

Figure 7.4. Surface view of undeformed and deformed samples showing important parameters used in the analysis of the core-shell structure. These parameters include change in core height (Δh), substrate deformation (Δs), and approximate change in shell thickness beneath indenter (Δt).

7.3.2 Analysis of indentation-retraction curves

The force on the repulsive indenter during indentation and retraction is plotted vs. core height for all samples in Figure 7.5. For the samples with no shell, we do a comparison with predictions from the Hertzian model for contact between two cylinders with parallel axes. Our approximation for the contact force is given by [31]

$$F \approx \frac{\pi}{4} E^* L d \,. \tag{7.9}$$

where E^* is the composite modulus for the two cylinders, L is the length of the cylinders in contact, and d is the indentation depth. The composite modulus is found by

$$E^* = \left[\frac{1 - \nu_{\mathrm{Al}}^2}{E_{\mathrm{Al}}} + \frac{1 - \nu_{ind}^2}{E_{ind}} \right]^{-1} , \tag{7.10}$$

where E_{Al} = 67.3 GPa and ν_{Al} = 0.355, as derived using isotropic relations [32] from the elastic moduli for Al in section 2.3. The modulus for the repulsive indenter is infinite, so the composite modulus becomes $E^* = E_{\mathrm{Al}}\left(1 - \nu_{\mathrm{Al}}^2\right)^{-1}$ = 77.0 GPa. The length of the cylinders in contact is the thickness of our simulation cell in the *z* direction, 0.285 nm. In our Hertz approximation we assume that the substrate is rigid, so indentation depth is equal to the change in core height, allowing us to replace d with Δh in eq. (7.9). The predicted contact forces using the Hertzian model from eq. (7.9) is shown in Figure 7.5(a). The force vs. core height curves in samples with no shell show good agreement with the Hertzian model.

The samples with no shell have an immediate recovery in core height during retraction, with slopes in the retraction curve almost parallel to those in the indentation curve, as shown in Figure 7.5(a). The samples with a shell thickness of 6.25 nm show a delayed recovery during retraction for samples with large core radii, as shown in Figure 7.5(b). Recovery during retraction

is even more delayed for samples with a shell thickness of 12.5 nm and core radii larger than 6.25 nm, as shown in Figure 7.5(c). The delayed recovery in samples with a-Si shells occurs because of the lack of elasticity in the a-Si shell. Deformations made to the a-Si shell during indentation remain mostly permanent. The deformed shell then pushes back against the recovering core as it rebounds during retraction. So, the presence of a shell delays recovery, with greater delays caused by shells of greater thickness. Ultimately the core makes a significant recovery in all samples. Samples with no shell have an average 80% recovery in core height, while samples with shells of 6.25 nm and 12.5 nm both have an average 87% recovery. So, while adding the shell delayed recovery in the core, the degree of recovery was greater than in samples without the shell.

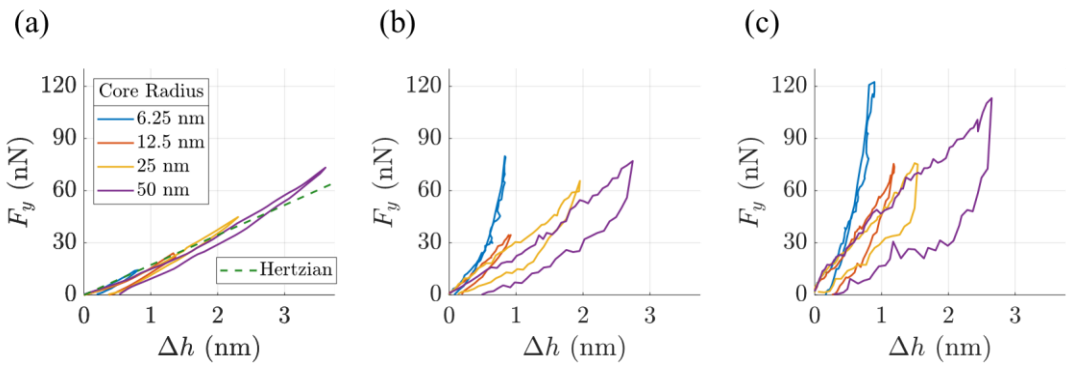

Figure 7.5. Force on indenter vs. change in core height for samples with (a) no shell, (b) 6.25 nm shell, and (c) 12.5 nm shell. Indentation occurs until first yield in core or substrate, after which the indenter is retracted. The predicted force using a Hertzian contact model is included in (a).

In analyzing Figure 7.5, we find that indentation-retraction curves have elastic hysteresis loops whose areas generally increase with increasing shell thickness. This is most distinct in comparing samples with a 50 nm core radius. The hysteresis loop area is largest with the 12.5 nm shell and smallest when no shell is present. This indicates that samples with larger a-Si shells have greater energy dissipation [33-35], which takes place mostly through plastic deformation of the shell. We also find that the slopes in the indentation curves of the samples with no shell show a slight but distinct decrease with increasing core radius, indicating that smaller core radii have

greater stiffness. This trend is also present in samples with a shell present, though in the samples with 12.5 nm shell thickness this trend is only obvious with core radii of 12.5 nm and 25 nm.

In comparing the peak indenter force at first dislocation for the samples with a-Si shells, we find the samples with a core radius of 6.25 nm to be major outliers. In these samples the core has a relatively low deformation while the force on the indenter is very high. The reason for these outliers is discussed in section 3.4.

7.3.3 Analysis of dislocations at yield

Yield in our samples is accompanied by dislocations nucleating within the Al core. All samples have initial dislocations nucleating either from the core surface when no shell is present, or the Al/a-Si interface when a shell is present. For the samples with no shell, this would seem to contradict the Hertzian model which predicts that yield will occur at the point of maximum shear stress some distance beneath the point of contact rather than at the surface. However, it is important to note that the Hertzian model is a continuum approach, which has limitations when considering atomic level features [36]. At the surface of our Al asperities with no shell, atomic layers form steps at the asperity surface which can act as stress concentrators [36-38]. When dislocations emit at these atom steps it can improve the coordination number of atoms at the step, lowering the energy cost of dislocation nucleation at these points [37]. Additionally, dislocations will only nucleate from the point of maximum shear stress if the shear stress is applied to one of the close-packed planes [39]. If the stress concentrations at the asperity surface produce local shear stress on a close-packed plane higher than any interior shear stress on a close-packed plane, then dislocations will nucleate from the surface. In our model, indentation is applied normal to the close-packed (111) plane. At this orientation the $(11\bar{1})$ plane is the most accessible for slip, and the maximum shear stress at the interior of the material does not reach the critical value on that

plane to initiate dislocation nucleation before it occurs at the surface. This is also seen in the indentation simulations of Nair et al. where dislocations in single crystals always initiated at the surface directly beneath the indenter [40].

In most of our samples possessing an a-Si shell, Shockley partial dislocations of the form $\langle 112 \rangle \{111\}$ nucleate from near the top of the core at yield. The only exception is the t_0 = 12.5 nm and R = 6.25 nm case, discussed later. For samples with no shell and core radii of 6.25, 12.5 and 50 nm we instead find Lomer-Cottrell dislocations of the form $\langle 110 \rangle \{001\}$ nucleating from near the top of the core. Lomer-Cottrell dislocations, also called Lomer-Cottrell junctions, are formed by the combination of two Shockley partials, [41]

$$\frac{a}{6}[112] + \frac{a}{6}[11\bar{2}] \rightarrow \frac{a}{3}[110] \ , \tag{7.11}$$

as shown in Figure 7.6 for one of our sample with no shell and where R = 50 nm.

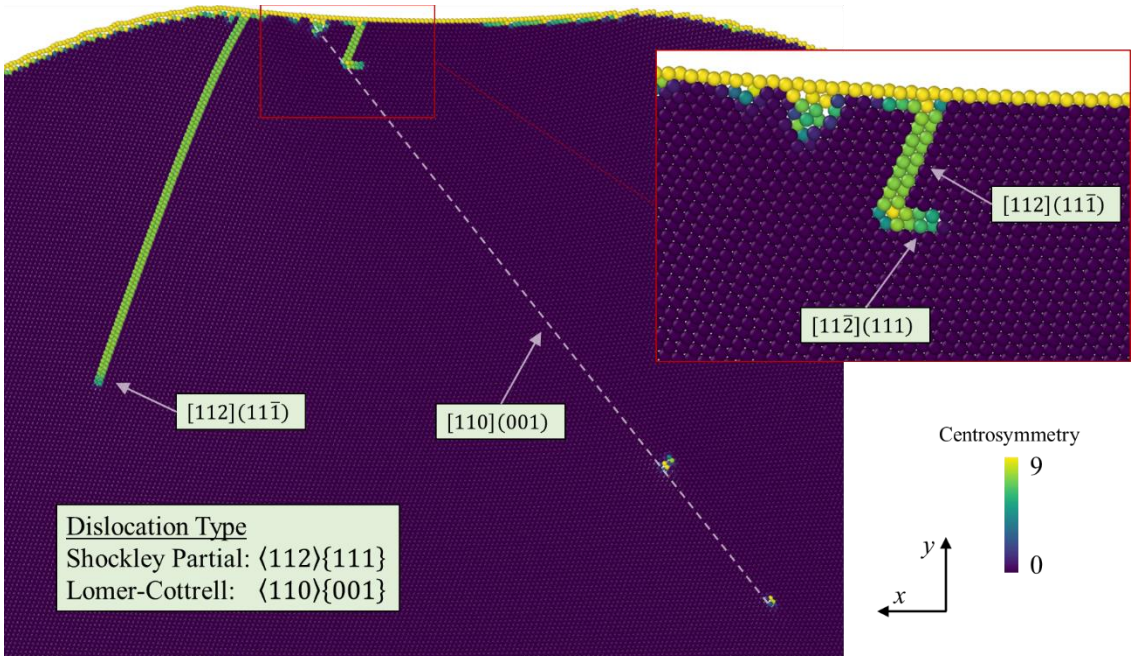

Figure 7.6. Dislocations present at yield in sample where t_0 = 0 and R = 50 nm. Atom color coding is based on centrosymmetry [42]. We find both Shockley partial dislocations and Lomer-Cottrell dislocations in the material, with the Lomer-Cottrell dislocation shown as a dashed line from the

free surface to its dislocation core. The inset shows a zoomed in view of the Shockley partials that combine to generate the Lomer-Cottrell dislocation.

Among the samples with no shell, the R = 25 nm sample is the only one to nucleate only Shockley partials at yield, with no Lomer-Cottrell dislocations. The presence of this exception shows that the formation of Lomer-Cottrell dislocations is by no means guaranteed when no shell is present, however, based on their presence in our other t_0 = 0 samples it seems that the likelihood of their occurring does increase. This may be due to free surfaces providing greater opportunity for multiple glide planes, which can combine to form Lomer-Cottrell dislocations. When an a-Si shell is present, it confines the core, and more energy is required to form dislocations, with much less chance of multiple dislocations forming a Lomer-Cottrell dislocation. We note that Lomer-Cottrell dislocations were also identified by Fleming et al. in their MD simulations of Al/a-Si core-shell nanostructures [10]. The Lomer-Cottrell dislocation cores we identify are similar to those seen by Weinberger et al. who also found that such dislocations are more mobile than previously thought [43].

Of all the samples with an a-Si shell, the only sample to possess a Lomer-Cottrell dislocation is the t_0 = 12.5 nm and R = 6.25 nm case. This sample is also unique as its first dislocation nucleates from the base of the core rather than near its top. This is because the a-Si shell flattens substantially during indentation, to such a degree that the core and its surrounding Al substrate deflect together, with the core remaining relatively undeformed. Stress concentrates at the sharp point where the base of the core, which is approximately in the $(11\bar{1})$ plane, meets the (111) plane of the substrate. Yield then occurs in a manner similar to what is shown in the inset of Figure 7.6, but with the combination of confined Al surfaces rather than Shockley partial dislocations.

7.3.4 Analysis of core-shell structure at yield

To better understand the effect that core-shell structure has on yield behavior, we plot the indenter force at yield vs. change in core height at yield for each of the samples, as shown in Figure 7.7(a). We use an asterisk (*) to indicate properties that occur at the point of yield. We find that increasing the core radius allows the core to deform more before first yield. We also find that increasing the shell thickness allows the core-shell structure to experience greater force before yield.

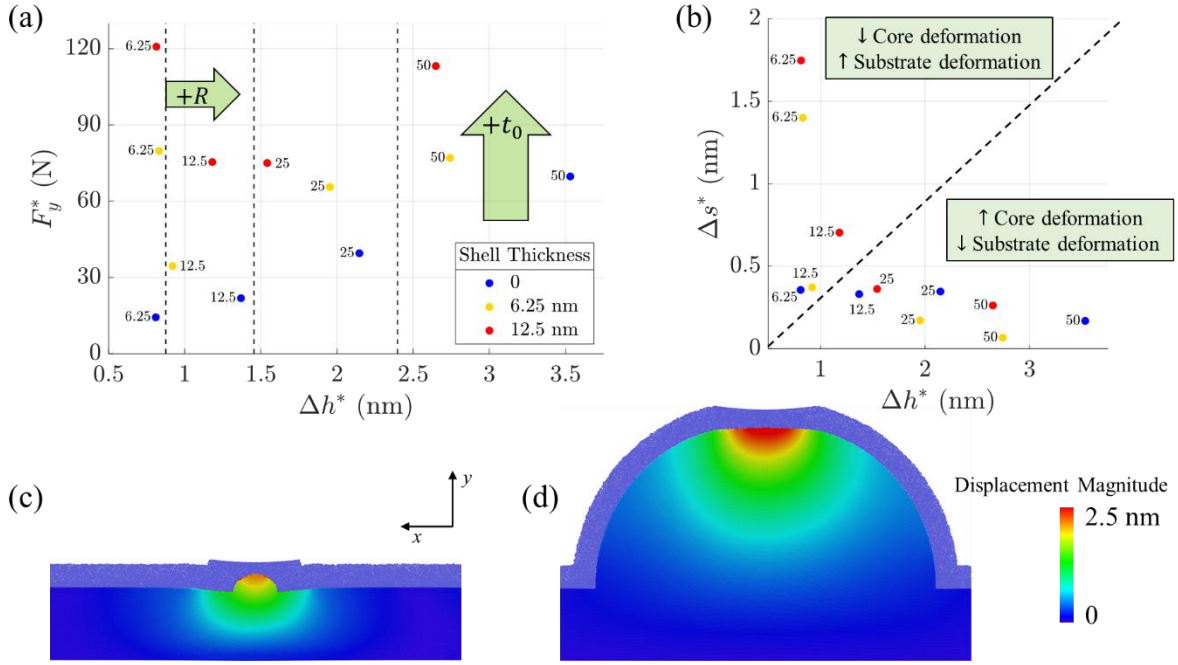

Figure 7.7. (a) Force on indenter at yield vs. change in core height at yield for all samples. In-plot text indicates core radius, with dashed vertical lines separating samples with differing core radii. Arrows indicate the direction of increasing core radius and increasing shell thickness. Note that as core radius increases the core can experience more deformation before yield. Also note that with increased shell thickness the force required to produce yield also increases. (b) Substrate deformation at yield vs. change in core height at yield for all samples. The dashed line separates samples that have different core deformation behavior. Samples in the upper left corner have greater deformation in the substrate than in the core, while samples in the lower right corner have more deformation in the core and very little in the substrate. (c) Core/substrate displacement field for sample with $t_0 = R$ = 6.25 nm, exhibiting high substrate deformation and relatively low core deformation. (d) Core/substrate displacement field for sample with t_0 = 6.25 nm and R = 50 nm, exhibiting low substrate deformation and high core deformation. Note that only Al atoms are colored based on displacement for (c) and (d).

As the indenter encounters the core-shell structure, the atoms in the core-shell structure are deformed in response. There are three ways in which these deformations can occur in the structures studied here. The first is by compressing the core, which will change the height of the core. The second is by pressing the core asperity into the substrate, deforming the substrate. The third is by displacing and deforming the shell. The balance of these different deformation behaviors depends on the core-shell structure. We plot substrate deformation at yield vs. the change in core height at yield for the different samples, as shown in Figure 7.7(b). We find that there are two general groupings in core-shell structures and their deformation. For samples with small core radius and large shell thickness, deformation is dominant in the substrate while the core experiences relatively little deformation, as demonstrated in the core/substrate displacement field in Figure 7.7(c). For samples with larger core radius, deformation is mostly in the core and there is very little deformation of the substrate, as shown in Figure 7.7(d). These deformation mechanisms explain the exceptionally high forces in the Al/a-Si core-shell structures with 6.25 nm core radius, as well as the relatively high force at dislocation of the sample with 12.5 nm shell thickness and 12.5 nm core radius. In these samples much of the deformation of the core-shell structure occurs in the substrate, delaying yield in the core until the indenter exerts the higher forces we observe.

7.3.5 Analysis of different deformation behaviors depending on core radius and shell thickness

We isolate the three sources of deformation in our core-shell structure and compare them for different core radii and shell thicknesses, as shown in in Figure 7.8. We observe that the change in core height at yield increases linearly with increasing core radius for samples of a given shell thickness, as shown in Figure 7.8(a). Samples with small core radius experience little core

deformation before yield, regardless of shell thickness, however, samples with larger core radius have decreased core deformation before yield when the shell is present.

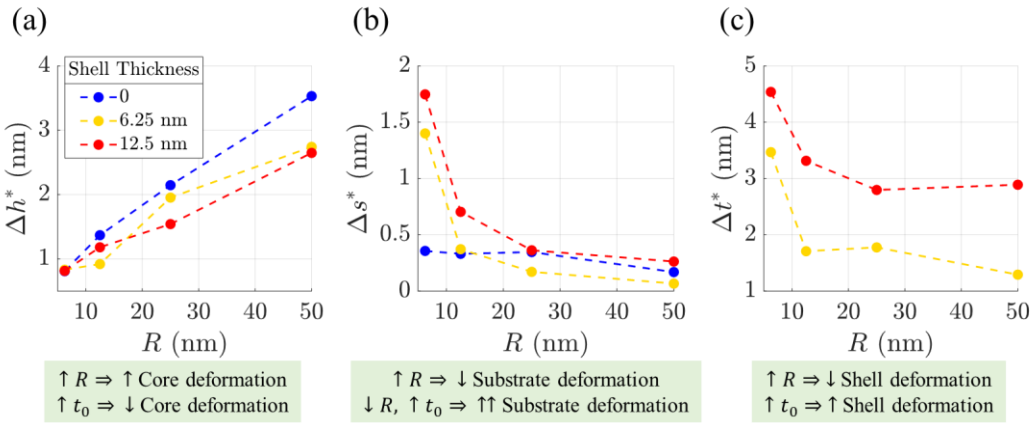

Figure 7.8. Plots showing deformation of core-shell structure in samples at the point of yield depending on core radius and shell thickness. Deformation is measured by (a) change in core height, (b) substrate deformation, and (c) change in shell thickness beneath indenter. Key results based on core radius and shell thickness are shown below each plot.

Substrate deformation at yield for different core-shell structures is shown in Figure 7.8(b). Samples with a core radius of 6.25 nm have a dramatic increase in substrate deformation when a shell is present. For all samples, particularly those with shells, increasing the core radius leads to decreased substrate deformation at yield.

The approximate change in shell thickness at yield for samples with shells is shown in Figure 7.8(c). We find that a larger shell thickness results in greater shell deformation before yield occurs in the core. This is unsurprising considering the greater dissipation energy we identified in samples with greater shell thickness, as discussed in section 3.2. We also observe that samples with lower core radius have high shell deformation. This further explains the high indenter forces in samples with small core radius as the indenter greatly deformed both the substrate and shell, delaying damage in the core.

7.3.6 Discussion of core-shell results

We find that the presence of an a-Si shell tends to delocalize forces from the indenter. In this way the amorphous shell and the surrounding Al substrate can contribute to loading and support the core, especially when the core is small. Larger cores eventually experience more localized compression and deformation in the core, producing yield before the surrounding substrate is deflected. We also note that for large cores the shell does protect the core from deformation, but it also delays the core from recovering from any deformation that does occur. Our results agree with the experimental and computational work of Sharma et al. who found that a thin layer of native oxide contributes to the strength of Ni nanoparticles under compression by cushioning their contact with the substrate and indenter [44]. The thickness of the oxide layer Sharma et al. identified is around 4 nm, which is smaller than the a-Si shell used in our model. This would seem to contradict the computational work of Sen et al. who predicted that native oxide decreases the strength of Al nanowires under tension when a native oxide layer is present [45]. They found that the interface between Al and Al oxide was more disordered than a pure Al surface, providing locations for easier dislocation nucleation and decreased strength. However, unlike our work or the work of Sharma et al., Sen et al. applied strain uniformly to the nanowires they simulated, with the oxide layer unable to provide any kind of buffer to prevent strain to interior Al. In our work, strains transmitted to the Al core are greatly diminished when the a-Si shell is present. Whatever disorder is produced at the Al/a-Si interface is insignificant compared to the effect of forces and strains being dispersed by the a-Si shell.

Our results have several implications for core-shell and asperity designs that will be subject to indentation. If the objective is to prevent the substrate from being damaged during indentation, then a large core should be used with a thin shell. On the other hand, if protection of the core is a

priority, then the core should be made smaller with a thicker shell. The methods utilized in this paper can be used for core-shell nanorods composed of different materials to identify their deformation characteristics as a function of structure. This would be a great aid in tailoring core-shell designs for different applications.

7.4 Conclusions

We have developed a method to implement a two material/phase in the CADD method to study core-shell nanorods. The spatial parameters we use in this study are change in core height, deformation of substrate, and approximate change in shell thickness beneath the indenter. While these parameters are challenging to obtain in experimental work, they allow for a deep understanding of deformation in the core-shell structure. The deformation behavior of Al/a-Si core-shell nanorods is dependent on the sizes of the core and shell. When no shell is included, the force on the indenter and the deformation of the core at yield increase linearly with the core radius. When a shell is present it protects the core during indentation by deforming and delocalizing forces produced by the indenter. In this way the core becomes less deformed and the core-shell structure can experience greater force from indentation before yield. For especially small core-shell structures we find that delocalized forces allow the substrate surrounding the core to deform and contribute to loading, further enhancing the stiffness of the nanorod and requiring even greater force before yield in the core. This work can help in designing core-shell structures which can be tailored for desired deformation characteristics. These core-shells will be useful in any application where the integrity of the nanostructure is important including micro/nano-electromechanical systems, nanolithography and nanotribology.

Acknowledgements

We sincerely thank support from National Science Foundation Grant No. 1463306 for funding this research. Authors would like to acknowledge the support by Arkansas High Performance Computing Center.

References

[1] M. Kang, Y.M. Park, B.H. Kim, Y.H. Seo, Micro-and nanoscale surface texturing effects on surface friction, Applied Surface Science 345 (2015) 344-348.

[2] M. Shafiei, A.T. Alpas, Nanocrystalline nickel films with lotus leaf texture for superhydrophobic and low friction surfaces, Applied Surface Science 256(3) (2009) 710-719.

[3] M. Zou, L. Cai, H. Wang, D. Yang, T. Wyrobek, Adhesion and friction studies of a selectively micro/nano-textured surface produced by UV assisted crystallization of amorphous silicon, Tribology Letters 20(1) (2005) 43-52.

[4] R.P. Nair, M. Zou, Surface-nano-texturing by aluminum-induced crystallization of amorphous silicon, Surface and Coatings Technology 203(5-7) (2008) 675-679.

[5] M. Zou, L. Cai, H. Wang, Adhesion and friction studies of a nano-textured surface produced by spin coating of colloidal silica nanoparticle solution, Tribology Letters 21(1) (2006) 25.

[6] Z. Guo, Y. Meng, C. Su, H. Wu, An on-chip micro-friction tester for tribology research of silicon based MEMS devices, Microsystem Technologies 14(1) (2008) 109-118.

[7] L. Chen, J. Zhang, Design and properties of self-assembled ordered films for nanolubrication, Surfactants in tribology 4 (2015) 97-150.

[8] W. Tidwell, D. Scott, H. Wang, R. Fleming, M. Zou, Nanoindentation study of deformation-resistant Al/a-Si core–shell nanostructures, Acta Materialia 59(15) (2011) 6110-6116.

[9] R.A. Fleming, J.A. Goss, M. Zou, Material dimensionality effects on the nanoindentation behavior of Al/a-Si core-shell nanostructures, Applied Surface Science 412 (2017) 96-104.

[10] R.A. Fleming, M. Zou, The effects of confined core volume on the mechanical behavior of Al/a-Si core-shell nanostructures, Acta Materialia 128 (2017) 149-159.

[11] K.J. Hemker, W.D. Nix, Nanoscale deformation: seeing is believing, Nature materials 7(2) (2008) 97-98.

[12] W.D. Nix, J.R. Greer, G. Feng, E.T. Lilleodden, Deformation at the nanometer and micrometer length scales: Effects of strain gradients and dislocation starvation, Thin Solid Films 515(6) (2007) 3152-3157.

[13] D. Mordehai, M. Kazakevich, D.J. Srolovitz, E. Rabkin, Nanoindentation size effect in single-crystal nanoparticles and thin films: A comparative experimental and simulation study, Acta Materialia 59(6) (2011) 2309-2321.

[14] A. Misra, R. Hoagland, Plastic flow stability of metallic nanolaminate composites, Journal of materials science 42(5) (2007) 1765-1771.

[15] L. Shilkrot, R. Miller, W. Curtin, Coupled atomistic and discrete dislocation plasticity, Phys Rev Lett 89(2) (2002) 025501.

[16] R.E. Miller, E.B. Tadmor, A unified framework and performance benchmark of fourteen multiscale atomistic/continuum coupling methods, Model Simul Mater Sc 17(5) (2009) 053001.

[17] L. Shilkrot, R.E. Miller, W.A. Curtin, Multiscale plasticity modeling: coupled atomistics and discrete dislocation mechanics, Journal of the Mechanics and Physics of Solids 52(4) (2004) 755-787.

[18] R.E. Miller, L. Shilkrot, W.A. Curtin, A coupled atomistics and discrete dislocation plasticity simulation of nanoindentation into single crystal thin films, Acta Materialia 52(2) (2004) 271-284.

[19] A. Nair, D. Warner, R. Hennig, Coupled quantum–continuum analysis of crack tip processes in aluminum, Journal of the Mechanics and Physics of Solids 59(12) (2011) 2476-2487.

[20] M. Fivel, Discrete dislocation dynamics: principles and recent applications, in: O. Cazacu (Ed.), Multiscale Modeling of Heterogenous Materials: From Microstructure to Macro-scale Properties, John Wiley & Sons2008, pp. 17-36.

[21] J.G. Steck, R.A. Fleming, J.A. Goss, M. Zou, Deformation and fatigue resistance of Al/a-Si core-shell nanostructures subjected to cyclic nanoindentation, Applied Surface Science 433 (2018) 617-626.

[22] J. Ahrens, B. Geveci, C. Law, Paraview: An end-user tool for large data visualization, in: C.D. Hansen, C.R. Johnson (Eds.), The Visualization Handbook, Elsevier2005, pp. 717-731.

[23] A. Stukowski, Visualization and analysis of atomistic simulation data with OVITO-the Open Visualization Tool, Model Simul Mater Sc 18(1) (2010).

[24] A.F. Bower, Applied mechanics of solids, CRC press2009.

[25] S. Plimpton, Fast Parallel Algorithms for Short-Range Molecular-Dynamics, J Comput Phys 117(1) (1995) 1-19.

[26] F. Pavia, W. Curtin, Parallel algorithm for multiscale atomistic/continuum simulations using LAMMPS, Model Simul Mater Sc 23(5) (2015) 055002.

[27] M. Baskes, Modified embedded-atom potentials for cubic materials and impurities, Phys Rev B 46(5) (1992) 2727.

[28] B. Jelinek, S. Groh, M.F. Horstemeyer, J. Houze, S.-G. Kim, G.J. Wagner, A. Moitra, M.I. Baskes, Modified embedded atom method potential for Al, Si, Mg, Cu, and Fe alloys, Phys Rev B 85(24) (2012) 245102.

[29] S.M. Rassoulinejad-Mousavi, Y. Mao, Y. Zhang, Evaluation of copper, aluminum, and nickel interatomic potentials on predicting the elastic properties, Journal of Applied Physics 119(24) (2016) 244304.

[30] J.D. Schall, G. Gao, J.A. Harrison, Elastic constants of silicon materials calculated as a function of temperature using a parametrization of the second-generation reactive empirical bond-order potential, Phys Rev B 77(11) (2008) 115209.

[31] V.L. Popov, Contact mechanics and friction, Springer2010.

[32] A.K. Kaw, Mechanics of composite materials, CRC press2005.

[33] O. Klymenko, J. Wiltowska-Zuber, M. Lekka, W. Kwiatek, Energy dissipation in the AFM elasticity measurements, Acta Physica Polonica-Series A General Physics 115(2) (2009) 548.

[34] G.L. Cross, A. Schirmeisen, P. Grütter, U.T. Dürig, Plasticity, healing and shakedown in sharp-asperity nanoindentation, Nature materials 5(5) (2006) 370.

[35] H.M. Lankarani, P.E. Nikravesh, Continuous contact force models for impact analysis in multibody systems, Nonlinear Dynamics 5(2) (1994) 193-207.

[36] J. Kiely, R. Hwang, J. Houston, Effect of surface steps on the plastic threshold in nanoindentation, Phys Rev Lett 81(20) (1998) 4424.

[37] O.R. De la Fuente, M. Gonzalez-Barrio, V. Navarro, B. Pabon, I. Palacio, A. Mascaraque, Surface defects and their influence on surface properties, Journal of Physics: Condensed Matter 25(48) (2013) 484008.

[38] C. Schuh, J. Mason, A. Lund, Quantitative insight into dislocation nucleation from high-temperature nanoindentation experiments, Nature Materials 4(8) (2005) 617.

[39] T. Michalske, J. Houston, Dislocation nucleation at nano-scale mechanical contacts, Acta Materialia 46(2) (1998) 391-396.

[40] A.K. Nair, E. Parker, P. Gaudreau, D. Farkas, R.D. Kriz, Size effects in indentation response of thin films at the nanoscale: A molecular dynamics study, International Journal of Plasticity 24(11) (2008) 2016-2031.

[41] H. Karnthaler, The study of glide on {001} planes in fcc metals deformed at room temperature, Philosophical Magazine A 38(2) (1978) 141-156.

[42] C.L. Kelchner, S. Plimpton, J. Hamilton, Dislocation nucleation and defect structure during surface indentation, Phys Rev B 58(17) (1998) 11085.

[43] C.R. Weinberger, W. Cai, The stability of Lomer–Cottrell jogs in nanopillars, Scripta Materialia 64(6) (2011) 529-532.

[44] A. Sharma, J. Hickman, N. Gazit, E. Rabkin, Y. Mishin, Nickel nanoparticles set a new record of strength, Nature communications 9(1) (2018) 4102.

[45] F.G. Sen, A.T. Alpas, A.C. Van Duin, Y. Qi, Oxidation-assisted ductility of aluminium nanowires, Nature communications 5 (2014) 3959.

Chapter 8

Conclusions

This dissertation predicts the mechanical properties of nanocomposites with 1-D, 2-D and 3-D reinforcing nanomaterials. The nanomaterials modeled in this process are 2-D graphene sheets (chapters 4-6), 1-D carbyne chains (chapter 6), and 3-D Al/a-Si core-shells nanorods (chapter 7). A Ni matrix is used as the bulk material for nanocomposites reinforced with 1-D and 2-D nanomaterials (chapters 4-6). The computational methods used in this work to predict mechanical properties include molecular dynamics (chapters 4, 5 and 7), density functional theory (chapter 6), and the coupled atomistic and discrete dislocation (CADD) multiscale method (chapter 7).

8.1 Summary of predicted mechanical properties

The key properties predicted in the different chapters include: stress intensity factor at yield, strain at yield (chapter 4); stress at yield, shear stress, graphene sheet height variance, stress in Ni contiguous with graphene sheet (chapter 5); elastic stiffness, specific stiffness, average valence charge per atom (chapter 6); indenter force at yield, core deformation, substrate deformation, and shell deformation (chapter 7). This work provides unique contributions in understanding each of the nanocomposites that are studied. These contributions are summarized below in brief:

1. When a crack is present in the Ni matrix of a Ni-graphene nanocomposite, the stress intensity factor and strain necessary to instigate yield in the Ni matrix increases as the distance between the crack and graphene sheet increases. This is due to graphene confining the stress intensity produced by the crack tip. (Chapter 4)

2. Ni-graphene nanocomposites with multilayer-graphene yields by delamination at much lower stress and strain than nanocomposites with monolayer graphene. (Chapter 4)
3. The failure modes for Ni-graphene nanocomposites with a crack in the Ni matrix depends on the loading direction relative to the embedded sheet and the orientation of the crack. For example, when load direction, crack orientation and the graphene sheet are all parallel to each other, yield occurs at very high stress compared to pure Ni, and the failure is catastrophic. If only the loading direction is changed, yield occurs by delamination at much lower stress than pure Ni. Other loading directions and crack orientations produce different non-catastrophic yield by dislocation. (Chapter 5)
4. Polycrystalline graphene is a better reinforcement in Ni-graphene nanocomposites than pristine graphene. This is because of its improved interfacial shear stress with contiguous Ni layers, which improves load transfer in the Ni matrix. This is also related to wrinkling in graphene sheets, which this work predicts to occur more in pristine graphene than in polycrystalline graphene. (Chapter 5)
5. The local stiffness of a carbyne-Ni nanocomposite under tension is dependent on carbyne's charge distribution. Carbyne improves the local stiffness only if it is dielectrically screened within the Ni-matrix, otherwise its structure breaks down and possibly forms Ni carbide. (Chapter 6)
6. Graphene serves as an effective dielectric screen for carbyne, allowing for improvement in the local stiffness of the nanocomposite proportional to the number of chains present. (Chapter 6)
7. The deformation behavior of Al/a-Si core-shell nanorods under indentation is dependent on the core radius and shell thickness. When no shell is present, indenter force and core

deformation increase linearly with core radius. A shell protects the core by deforming and delocalizing forces produced by the indenter. This allows the core-shell structure to experience greater force before the core itself begins to yield. (Chapter 7)

8. Three forms of deformation are possible for Al/a-Si core-shell nanorods under indentation: core deformation, shell deformation and substrate deformation. Core-shell structures with especially small cores experience high substrate deformation and low core deformation at yield. The opposite is true when cores are large. (Chapter 7)

8.2 Summary of unique methodological contributions

In addition to the predicted mechanical properties/behavior, this work makes a few unique methodological contributions that are worthy of note:

1. A method is developed for generating a "patchwork quilt" polycrystalline graphene sheet (outlined in section 3.1.4, used in chapter 5).
2. Specific stiffness is identified as an ideal parameter for low-dimensional materials due to its independence from assumptions about volume when using the energy vs. strain relation (chapter 6). A Rule of Mixtures for specific stiffness is also derived (Appendix B).
3. CADD is modified to utilize two materials, with theoretical justification provided for this modification in the continuum region (chapter 7).
4. Core-shell spatial parameters are separately collated to allow detailed analysis of core-shell structures during indentation (chapter 7).

8.3 Future work

8.3.1 Ni-graphene nanocomposites

Delamination can be avoided if care is taken to only use monolayered graphene sheets in Ni-graphene nanocomposites. However, the cost of producing pristine monolayered graphene is quite high. Fortunately, this research suggests that easier-to-produce polycrystalline graphene sheets may be superior to pristine in nanocomposite applications. Experimental and computational work should be done to determine whether multilayered polycrystalline sheets are as prone to delamination as pristine sheets. It is possible that interactions at graphene grain boundaries may improve adhesion between polycrystalline graphene sheet layers, which would help to prevent delamination.

8.3.2 Carbyne-Ni nanocomposites

In this research pristine graphene is successfully used to dielectrically screen carbyne from a Ni matrix. To what extent are defective graphene sheets also able to dielectrically screen carbyne? Computational work should be done to determine the effect that vacancies or interstitials in a graphene sheet will have on enclosed carbyne. Also, the work presented here does not include hydrogen end caps. Future work could determine the effect that hydrogen has on dielectric screening, whether that screening is done by graphene, carbon nanotubes, or with some other material. One of the limiting factors in this work is the number of Ni atoms necessary for tensile loading in DFT. A study focused on investigating the effects of dielectric screening alone rather than the local stiffness of an entire nanocomposite could use a much smaller number of Ni atoms (or a different material that carbyne is to be screened from), which would grant more flexibility in

graphene sheet size (or a different screening material) and carbyne chain length than is possible in this study.

8.3.3 Al/a-Si core-shell nanorods

The version of CADD utilized in this research is the original 2-D version of CADD, which necessitates the study of semicylindrical nanorods rather than hemispherical nanostructures. Different core-shell structures should be tested to determine whether the deformation mechanisms identified in this work hold for different geometries. Different materials can also be tested in the core and/or shell. These tests could be performed in either pure MD or using a multiscale model.

Appendix A

Supplementary material for Paper 2: Failure mechanisms in pre-cracked Ni-graphene nanocomposites

Supplementary figures are included to allow readers to analyze the predicted stress values in Figures 5.4 and 5.8 in chapter 5. Table A1 is included from chapter 5 as a reference for the loading conditions of cases 1-4. The values used in Figure 5.4 are explained by Figures A1, A2, A3 and A4, which show the stress vs. strain curves for cases 1, 2, 3 and 4 respectively. The "(a)" portion of Figures A1-A4 is for Ni-graphene samples with only one graphene sheet present. The "(b)" portion of Figures A1-A4 is for Ni-graphene samples with two graphene sheets present. The values shown in Figure 5.8 are explained by Figure A5, which shows the stress vs. strain curves for the large Ni-graphene samples discussed in sections 5.2.3 and 5.3.2 of chapter 5. Note that multiple simulations were run for each sample to account for variations due to different starting velocities, with each simulation having a different number seed; the stress vs. strain curves are shown for only one of the simulations for each sample.

Table A1. Key to different Ni-graphene loading directions and crack orientations used in the simulations. Included for convenience in analyzing stress vs. strain figures.

	Case 1	Case 2	Case 3	Case 4
Loading direction relative to graphene sheet	∥	∥	⊥	⊥
Crack orientation relative to graphene sheet	∥	⊥	∥	⊥
Visualization	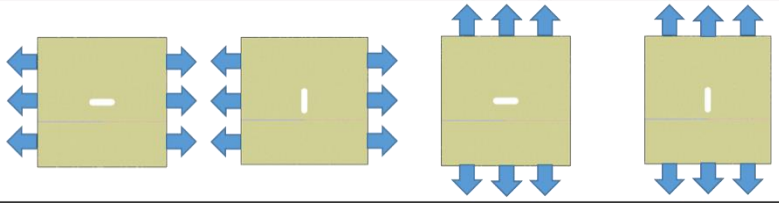			

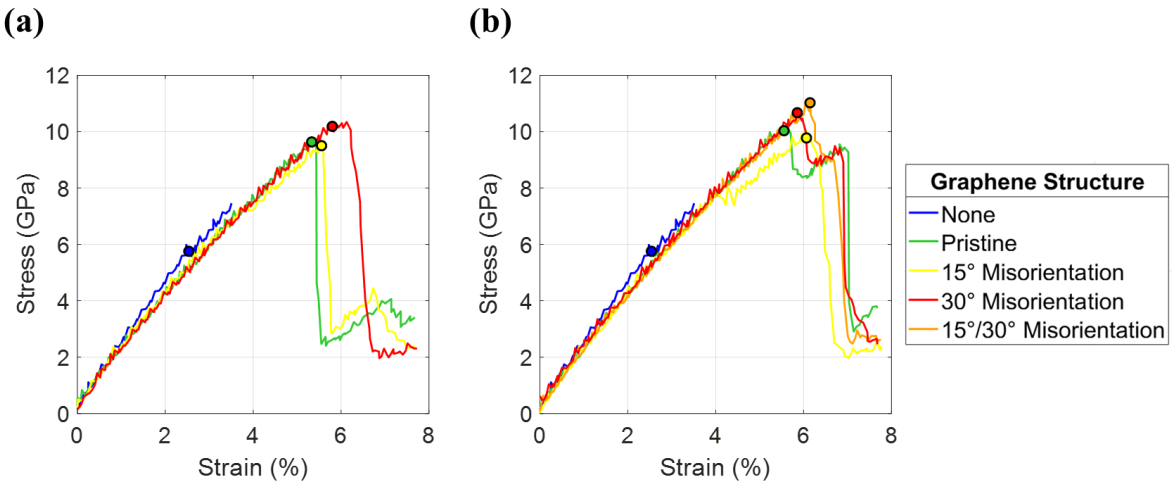

Figure A1. Stress vs. strain for case 1 samples with (a) one graphene sheet, or (b) two graphene sheets present. Colored dots indicate stress and strain at first yield.

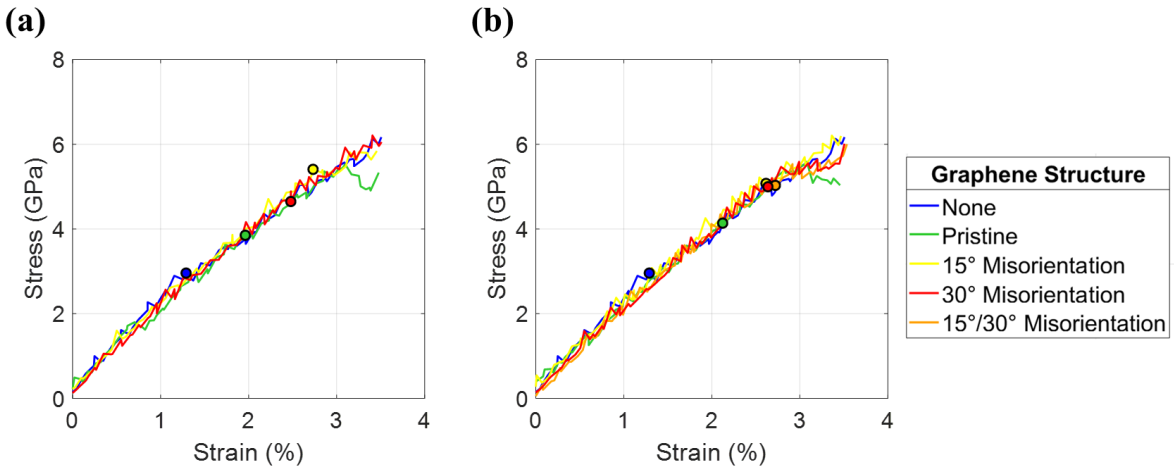

Figure A2. Stress vs. strain for case 2 samples with (a) one graphene sheet, or (b) two graphene sheets present. Colored dots indicate stress and strain at first yield.

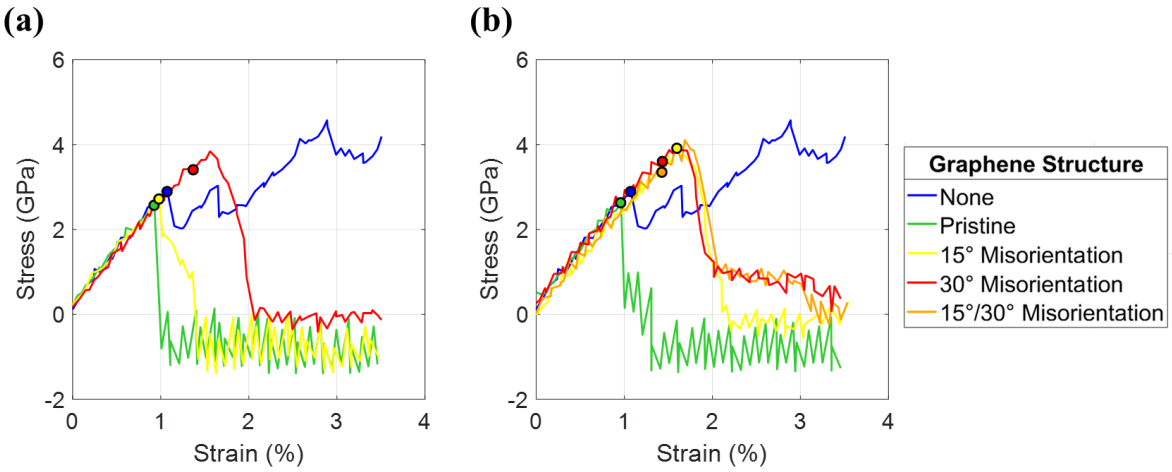

Figure A3. Stress vs. strain for case 3 samples with (a) one graphene sheet, or (b) two graphene sheets present. Colored dots indicate stress and strain at first yield.

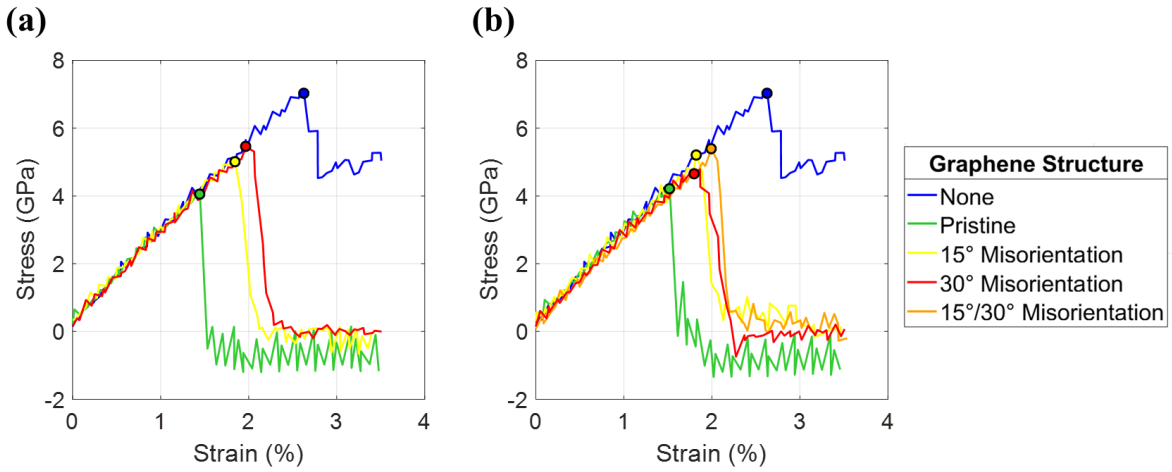

Figure A4. Stress vs. strain for case 4 samples with (a) one graphene sheet, or (b) two graphene sheets present. Colored dots indicate stress and strain at first yield.

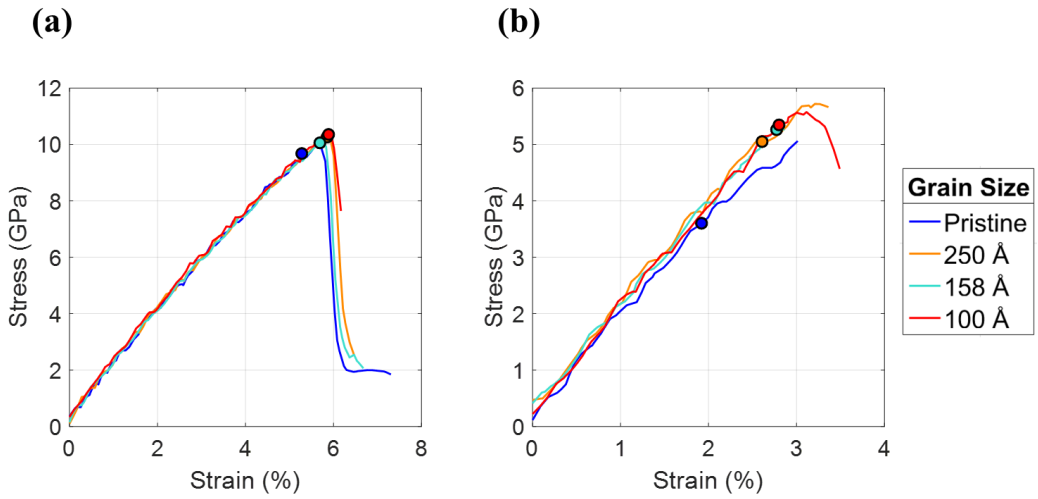

Figure A5. Stress vs. strain for large Ni-graphene samples with (a) case 1 loading and crack orientation, (b) case 2 loading and crack orientation. Colored dots indicate stress and strain at first yield.

Appendix B

Supplementary material for Paper 3: Carbyne as a fiber in metal-matrix nanocomposites: A first principle study

Derivation of general rule of mixtures for specific stiffness

The rule of mixtures used to estimate the longitudinal Young's modulus (E) for a composite as a weighted mean of the matrix and fiber modulus is given by [1]

$$E_c = v_m E_m + v_f E_f \,, \tag{B1}$$

where v_j is the volume fraction of material j, defined as

$$v_j = \frac{V_j}{V_c}, \tag{B2}$$

where V_j is the volume of material j. Consider a composite material composed of a matrix with three different types of fibers, all aligned parallel in the longitudinal direction, as shown in Figure B1. If we only try to estimate the Young's modulus for the matrix and the first fiber, we get

$$E_{c1} = \frac{V_m}{V_{c1}} E_m + \frac{V_1}{V_{c1}} E_1 \,. \tag{B3}$$

Composite $c1$ can now be the considered the matrix in which fibers 2 and 3 are present. If we now consider only fiber 2 in the composite matrix $c1$, the estimated Young's modulus is

$$E_{c12} = \frac{V_{c1}}{V_{c12}} E_{c1} + \frac{V_2}{V_{c12}} E_2 \,, \tag{B4}$$

If we substitute eq. (B3) into (B4), we get

$$E_{c12} = \frac{V_m}{V_{c12}} E_m + \frac{V_1}{V_{c12}} E_1 + \frac{V_2}{V_{c12}} E_2 \,. \tag{B5}$$

By this same pattern combining $c12$ and fiber 3 yields

$$E_{c123} = \frac{V_m}{V_{c123}} E_m + \frac{V_1}{V_{c123}} E_1 + \frac{V_2}{V_{c123}} E_2 + \frac{V_3}{V_{c123}} E_3 \,, \tag{B6}$$

which, using eq. (B2), becomes

$$E_{c123} = v_m E_m + v_1 E_1 + v_2 E_2 + v_3 E_3 \,. \tag{B7}$$

More generally, for a composite with N materials including a matrix and N-1 fibers aligned in parallel, the longitudinal Young's modulus may be estimated as

$$E_c = \sum_{i=1}^{N} v_i E_i \,. \tag{B8}$$

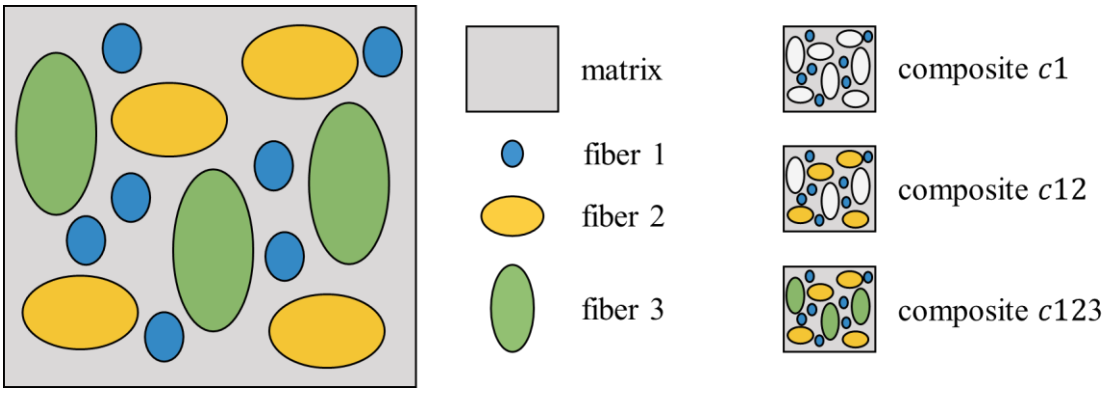

Figure B1. Visual of composite material composed of a matrix and three fibers. Note that the white shapes in composites $c1$ and $c12$ represent the absence of fibers 2 and 3 and fiber 3 respectively.

The specific stiffness of a material is defined as

$$S = \frac{E}{\rho} \,, \tag{B9}$$

where E is the Young's modulus and ρ is the density of the material. If we divide the Young's modulus in eq. (B8) by the composite's density, we get

$$S_c = \frac{1}{\rho_c} \sum_{i=1}^{N} v_i E_i \, . \tag{B10}$$

This can be rearranged to become

$$S_c = \sum_{i=1}^{N} \left(\frac{V_c}{m_c}\right) \frac{V_i}{V_c} \, E_i = \sum_{i=1}^{N} \frac{V_i}{m_c} \, E_i \, , \tag{B11}$$

where V is volume and m is mass. Based on eq. (B9), we know that $E_i = \frac{m_i}{V_i} S_i$, which can be substituted into eq. (B11) to get

$$S_c = \sum_{i=1}^{N} \frac{m_i}{m_c} \, S_i = \sum_{i=1}^{N} w_i \, S_i \, , \tag{B12}$$

where w_i is the weight fraction of material i. Thus, the estimated specific stiffness of the composite is not dependent on volume, given the specific stiffness values of the constituent materials. Note that all the assumptions used to obtain eq. (B8) still apply to eq. (B12).

References

[1] A.K. Kaw, Mechanics of composite materials, CRC press2005.